Report Submitted to	Patcharin Burke, Ph.D. Advanced Energy Systems Division U.S. DOE, National Energy Technology Laboratory 626 Cochrans Mill Road, P.O. Box 10940, Pittsburgh, PA 15236 Phone: 412-386-7378 Email: Patcharin.Burke@NETL.DOE.GOV
Project Number	DE-FE-0026097
Project Title	Developing Accelerated Test Protocols and Tuning Microstructures of the Common Materials to Improve Robustness, Reliability, and Endurance of SOFC Cells
PI Contact Information	Professor Mike Matthews 301 Main Street Columbia, SC 29208 E-mail: mamatthe@mailbox.sc.edu
Submitted by	Professor Xiao-Dong Zhou 301 Main Street Columbia, SC 29208 E-mail: zhox@cec.sc.edu zhou@louisiana.edu
Submission Date	November 27, 2021
DUNS	11-131-0249
Recipient Organization	Sponsored Programs Office University of South Carolina
Project Period	10/01/2015 – 07/31/2021
Reporting Period End Date	10/30/2021
Report Frequency	Final Report
Signature	XiaoDong Zhou

DISCLAIMER* -- The Disclaimer must follow the title page, and must contain the following paragraph:

> "This report was prepared as an account of work sponsored by an agency of the United States Government. Neither the United States Government nor any agency thereof, nor any of their employees, makes any warranty, express or implied, or assumes any legal liability or responsibility for the accuracy, completeness, or usefulness of any information, apparatus, product, or process disclosed, or represents that its use would not infringe privately owned rights. Reference herein to any specific commercial product, process, or service by trade name, trademark, manufacturer, or otherwise does not necessarily constitute or imply its endorsement, recommendation, or favoring by the United States Government or any agency thereof. The views and opinions of authors expressed herein do not necessarily state or reflect those of the United States Government or any agency thereof."

Abstract

Developing Accelerated Test Protocols and Tuning Microstructures of the Common Materials to Improve Robustness, Reliability, and Endurance of SOFC Cells

This work is built on the prior work where the phase transformation in praseodymium nickelates, e.g. Pr_2NiO_4 (PNO) and $(Pr_{1-x}Nd_x)_2NiO_4$ (PNNO), can be electrochemically driven, and is substantially faster when compared to thermal annealing studies.

The first task aims at an attempt to further accelerate the phase transformation in the oxygen electrode by alternating the current input in the cells, which lead to the development of accelerated test protocols (ATPs). ATPs showed up to 60× faster phase transformation and up to 10x faster performance degradation in $(Pr_{0.50}Nd_{0.50})_2NiO_4$ electrodes, when compared to long-term operation under constant current density. Furthermore, the phase stable Nd_2NiO_4 and $(La_{0.6}Sr_{0.4})(Co_{0.8}Fe_{0.2})O_3$ (LSCF6482) electrodes were tested in full cells under ATPs, and showed up to 10× faster performance degradation within 1,100 hours in a comparison with long-term thermal annealing studies and electrochemical operation under constant current density.

The second task aims at the quantification of the contributions of cell components to the total impedance of a solid oxide fuel cell (SOFC) using electrochemical impedance spectroscopy (EIS) and distribution of relaxation times (DRT). Specifically, the role of gas composition at both anode and cathode was systematically studied, aiming at deconvoluting, identifying and quantifying the contributions of different electrode processes. This was achieved by first tuning the partial pressure of H_2 at the anode and subsequently varying the partial pressure of O_2 at the cathode. The results suggest that, while DRT offers a viable way of deconvoluting different times distributions, additional attention is needed before assigning a peak to a specific electrode process due to the significant overlap of the contributions from the cathode and the anode.

Density function theory studies show that both Pr-vacancies and O-defects play a key role on the activity and stability for nickelates towards oxygen reduction reaction. The resident O-interstitials and oxygen ions in the PrO layer form peroxide (O_2^{2-}) nearby Pr vacancies. The O_2^{2-} limits oxygen-ion transport due to the required additional energy to break its O-O bond. The formation and segregation energies were then calculated for different Ln ions (La, Pr, Nd, Pm, Sm, Gd, Tb, Dy, and Ho) in PNO and $CeO_2(111)$ surfaces. In addition to Nd, Pm and La are suggested as potential dopants in PNO to enhance it stability without decomposition due to their more negative formation energies, lower diffusion energies, and positive separation energies.

Contents

A. Executive Summary

A long-lasting challenge in SOFC R&D is to develop accelerate test protocols because an operation of SOFCs under its normal conditions for tens of thousands of hours is often impractical and costly. Hence, reliable and accelerated test methods are needed to facilitate rapid learning on key durability and reliability issues. Cares, however, must be taken to develop accelerated test protocols to ensure that (1) there are no new failure mechanisms introduced, which would be unrealistic in a real SOFC environment and (2) detailed and reliable examinations are performed on single cells or stacks under the steady-state operation to provide reproducible baselines.

This project invokes a systematic and intensive effort focused on understanding the relationships between accelerated materials structure and resident chemistry on the electrochemical properties and durability. This dichotomy to obtain durable and active cathodes can only be realized in materials where structure can be manipulated not only at the unit cell level in crystalline materials but also the electrode-electrolyte interfaces. The experimental constituent of the proposal aims at (1) developing accelerating test protocols by adopting cycling potentials between open circuit voltage (OCV) and an operating potential and (2) identifying and quantifying the contributions of cell components to the total impedance of a solid oxide fuel cell.

The accelerated test protocols (ATPs) showed its applicability in nickelate cathodes: up to 60x faster phase transformation and up to 10x faster performance degradation in $(Pr_{0.50}Nd_{0.50})_2NiO_4$ electrodes, when compared to long-term operation under constant current density. Furthermore, the phase stable Nd_2NiO_4 and $(La_{0.6}Sr_{0.4})(Co_{0.8}Fe_{0.2})O_3$ (LSCF6482) electrodes were tested in full cells under ATPs, and showed up to 10x faster performance degradation within 1,100 hours in a comparison with long-term thermal annealing studies and electrochemical operation under constant current density.

In terms of using the distribution of relaxation time (DRT) analysis to quantify the contributions of cell components to the total impedance, while DRT offers a viable way of deconvoluting different times distributions, additional attention is needed before assigning a peak to a specific electrode process due to the significant overlap of the contributions from the cathode and the anode. Density function theory studies show that both Pr-vacancies and O-defects play a key role on the activity and stability for nickelates towards oxygen reduction reaction. The resident O-interstitials and oxygen ions in the PrO layer form peroxide (O_2^{2-}) nearby Pr vacancies. The O_2^{2-} limits oxygen-ion transport due to the required additional energy to break its O-O bond. In addition to Nd, Pm and La are suggested as potential dopants in PNO to enhance it stability without decomposition due to their more negative formation energies, lower diffusion energies, and positive separation energies.

B. Task 2. Use Full-Size Cells to Develop Accelerated Test Protocols

B.1 Introduction

With time consuming and costly long-term solid oxide fuel cell (SOFC) operation, the approach towards development of new phase-stable cathodes has been mostly oriented towards thermal annealing studies. Thermal annealing studies on powders and electrodes cannot simulate the phase transformation behavior in cathodes in operating cells. The role of electrochemical potential on phase transformation and performance stability must be considered in SOFCs. Since the targeted operation of ~40,000 hours is required for commercial SOFC applications, finding a way to develop accelerated test protocols that can simulate long-term operation in a fraction of time is highly desired. Such approach would allow for faster material screening, faster cathode and cells evaluation, and would significantly drop down the costs of SOFC system development.

The phase transformation in thermal annealing studies is bound by the laws of thermodynamics. Annealed materials will effectively reach thermal equilibrium that will govern the phase evolution. In other words, the changes on the electrode surface and in the bulk are only affected by fluctuations in the thermodynamic parameters (e.g. temperature, pressure, and molar number). However, an operating SOFC is a non-equilibrium system subjected to continuous and non-linear flux across the material. During electrochemical reaction, the electrode undergoes a transfer of matter and energy with the surroundings and is also subjected to external thermodynamic forces. Furthermore, the presence of electrochemical potential, as a dominating driving force in operating cells, cannot be overlooked. The generated difference in electrochemical potential across the fuel cell can be considered as analogous to temperature gradients or pressure differences that drive phase transformations in other systems. Chiang et al.[1-3] and his group have made considerable efforts to understand electrochemically driven phase transformation in electrodes for lithium-ion batteries, but no such attempt has been made in the SOFC field. Therefore, better understanding of such behavior in complex SOFC systems is of fundamental importance.

This task aims at an attempt to further accelerate the phase transformation in the oxygen electrode by alternating the current input in the cells, which lead to the development of accelerated test protocols (ATPs). ATPs showed up to 60x faster phase transformation and up to 10x faster performance degradation in $(Pr_{0.50}Nd_{0.50})_2NiO_4$ electrodes, when compared to long-term operation under constant current density. Furthermore, the phase stable Nd_2NiO_4 and $(La_{0.6}Sr_{0.4})(Co_{0.8}Fe_{0.2})O_3$ (LSCF6482) electrodes were tested in full cells under ATPs, and showed up to 10x faster performance degradation within 1,100 hours in a comparison with long-term thermal annealing studies and electrochemical operation under constant current density.

B.2 Experimental Method

B.2.1 Preparation of Powders and Electrodes

Starting materials, including $La(NO_3)_3$, $Sr(NO_3)_2$, $Co(NO_3)_2$, $Fe(NO_3)_2$, $Mn(NO_3)_2$, $Pr(NO_3)_3$, $Nd(NO_3)_3$, and $Ni(NO_3)_2$ (99.9% REO, Alfa Aesar, Haverhill, MA) were standardized using thermogravimetric analysis and were used in glycine nitrate combustion process.[4] The synthesized powders were calcined in air with 3°/min heating and cooling rates. Single phase powders were studied via x-ray diffraction (XRD) analysis, using a Rigaku Miniflex II (Houston, TX) equipped with scintillating and high-speed silicon strip (D/teX) detectors. Details on normalizing the flux and peak positions have been reported elsewhere and incorporated the use of multiple external and internal standards.[5] Thermal annealing tests on powders and electrodes were conducted in 3% humidified air flow.

The bilayers comprised of Ni-YSZ and YSZ electrolyte were prepared through a non-aqueous tape-casting and lamination process, which yielded 40 vol% Ni and 60 vol% YSZ in reduced anode. The final composition of the functional anode layer, after reduction, was 50 vol% for both Ni and YSZ. The dense electrolyte membrane was 8 μm thick. A $Gd_{0.20}Ce_{0.80}O_{1.90}$ (GDC-20, Fuel cell materials, OH) layer was screen-printed on YSZ and co-sintered with the anode current collector (Ni mesh embedded in NiO paste) at 1200 °C for 2 hours. Standardized nitrates (Alfa Aesar, 99.9%) were used in a glycine-nitrate combustion process for nickelate powder synthesis.[10] Thermal annealing was performed to obtain a single phase, orthorhombic structure. Micrometer carbon powders were added as a pore former to the cathode powder, which was ball milled to obtain a mean particle size of 200-300 nm. The cathode ink was screen printed and sintered at 1200 °C for 2 hours. The active cathode area is 1 cm^2. Gold grid was then screen-printed (paste obtained from Ferro, 99.9%) and sintered at 900 °C, resulting in a thickness of 10 μm. Pt wires were co-sintered with the current collector for a four probe measurement. YSZ electrolyte tapes (ESL ElectroScience) were fired at 1300 °C for 2 hours and used for thermal annealing tests. Cathodes and current collector were printed following the aforementioned procedure.

B.2.2 Measurement of Electrochemical Performance

Each full cell was electrically connected to the test fixture with Pt wires, and then sealed on a tubular alumina stand with glass paste. A perforated alumina cap was laid on top of the cell and spring-loaded to provide sufficient mechanical contact and air delivery to the cathode side. Anode was provided with 3% humidified H_2 at a flow rate of 200 sccm, and cathodes were supplied with 400 sccm air. Biologic VMP3 multi-channel potentiostat (Bio-Logic USA, Knoxville, TN) equipped with external current boosters was used for i-V sweep and EIS measurements. The i-V measurements were performed with 5 mV/s scan rate, and EIS was measured between 0.1 Hz and 50 kHz, with a scan rate of 30 points per decade. The *dc* and *ac* measurements were performed every 25 hours of operation. Distribution of relaxation time analysis is performed by the DRTTools with a regularization parameter of 0.001. [25] The areas of peaks are calculated by fitting the DRT spectrum with the gaussian functions and integrating the corresponding areas beneath the function.

B.2.3 Accelerated Test

The accelerated tests were performed by injecting the selected current for 2 seconds in the cells, then resting the cell for 1s. For 300 hours of operation this is equivalent to 360,000 cycles (=300 hours × 1 cycle/3-seconds × 3,600 second/hour = 360,000 cycles), while for 1,100 hours of operation 1,320,000 cycles (= (=1,100 hours × 1 cycle/3-seconds × 3,600 second/hour = 1,320,000 cycles) were generated. Cells undergoing accelerated test protocols (ATPs) were compared against cells operated at constant current density.

B.3 Results and Discussion

B.3.1 Electrochemically Driven Phase Transformation

The stabilized long-term performance can be achieved with Nd substitution on the Pr-site[6] in PNO, along with suppressed phase transforamtion.[7] However, the extent of phase transformation in thermally annealed PNNO electrodes (for [Nd] $\leq$ 50%) deviated from the results obtained after operation in full cells. **Figure 1** shows quantified[5] phase evolution in PNNO series on thermally annealed electrodes for 500 hours at 750 °C, and electrochemically operated electrodes in full cells at 0.80 V. Two sets of full cells show reproducible phase transformation. However, it is imperative to note that phase transformation in thermally annealed electrodes is substantially lower than in operated electrodes. This finding brings to a question as to what extent do operating conditions on PNNO materials influence the phase transformation, which has been linked to performance degradation in full cells.

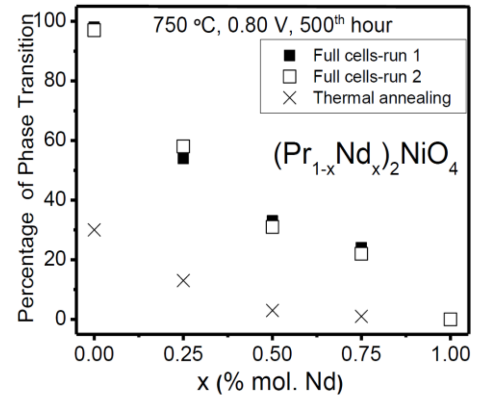

Figure 1. Phase evolution in thermally annealed electrodes (750 °C, 500 hours) and electrochemically operated $(Pr_{1-x}Nd_x)_2NiO_4$ electrodes after 500 hours at 750 °C and 0.80 V

The aforementioned theory was studies via systematic tests on multiple full cells. **Figures 2a-c** show i-V and power density curves on PNNO cells operated at various current densities (0.25, 0.50, and 0.75 A/cm^2, respectively) at 790 °C. The performance remains stable after 300 hours of continuous operation. **Figure 2d** shows reproducible results on three cells at each current density. Relatively stable operation in PNNO cells[6] (0.25%/1,000 hours performance degradation) was observed while being held at 750 °C and 0.8 V for 500 hours, but detected phase transformation after operation.[7] The retained activity and performance stability was linked to startling formation of PNNO nanoclusters, which lead to increase in active area for oxygen reduction reaction (ORR) and exposed surface for direct ORR. However, the focus of this work is to manipulate phase transformation with electrochemical operation since the phase transformation may not be evident from the DC measurements. Consequently, a closer look was given to EIS spectra[6] with an attempt to identify any changes in the electrodes.

In operando distribution of relaxation times (DRT) analysis[8-11] was obtained from the inverse Fourier transform of impedance spectra. DRT allows different processes on electrode to be separated based on their relaxation frequency. Therefore, instead of having a single or double EIS arc,[6] each process will be show as a separate peak in DRT plot, **Figure 3a**.[8] Furthermore, DRT has high resolution ability and can separate processes that resonate within half a decade, while EIS can only separate processes that resonate at frequencies within two to three orders of magnitude. As a result, different processes associated with electrode can be studied. An increase in polarization of cathodic peaks (P1c-P3c)[6] was detected along with shifts to higher frequency, **Figure 3a**. This behavior has been previously associated with increase in resistance for overall ORR in PNNO electrodes.[6, 8, 11] The area specific resistance (ASR) for the cathodic peaks that experience the largest change is shown in **Figure 3b**. Both P2c and P3c (associated with ORR)[6] increase over time. The rate of increase is promoted by fourfold with increase in current density from 0.25 A/cm^2 to 0.75 A/cm^2. The evolution of cathodic peaks clearly indicates increase in electrode resistance, which is not evident from the i-V and power density curves. Therefore, detailed analysis of EIS spectra could potentially provide some insights into phase transformation.

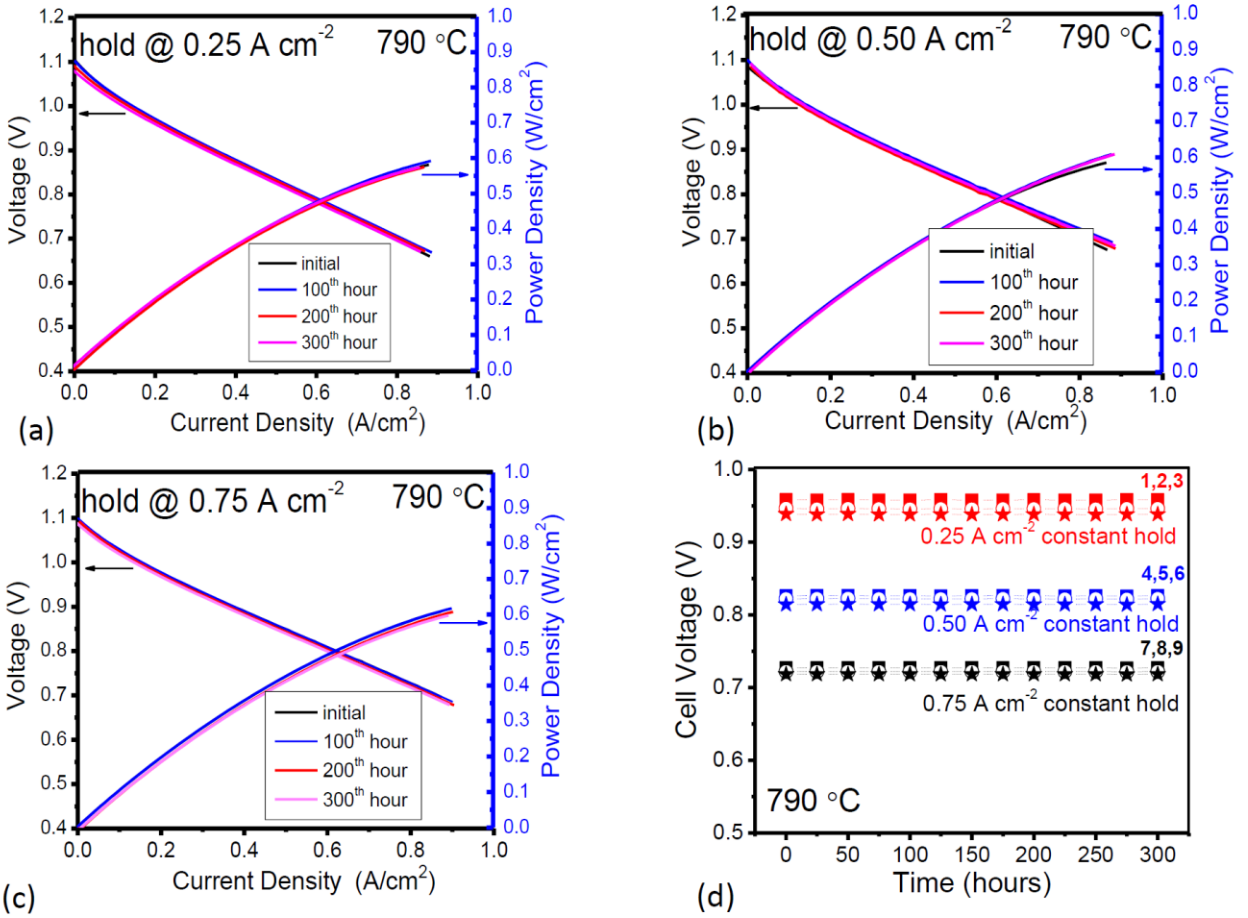

Figure 2. i-V and powder density curves as function of time for cells operated under continuous current at (a) 0.25 A/cm^2, (b) 0.50 A/cm^2, and (c) 0.75 A/cm^2. (a) Performance stability as function of time under various current density.

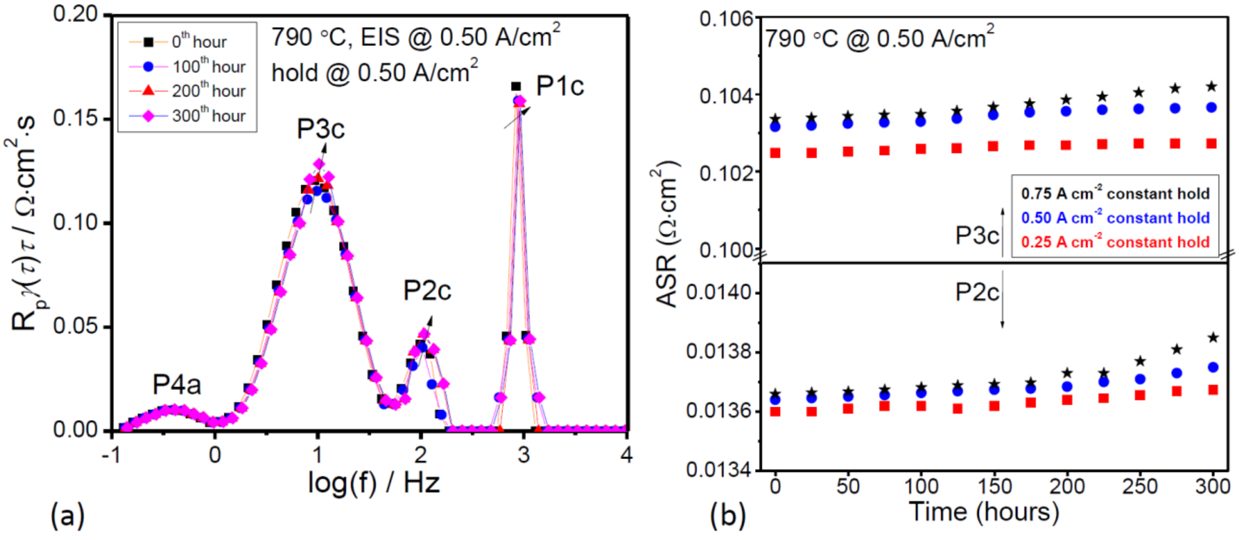

Figure 3. (a) Representative DRT analysis on operating cell measured at 790 °C and 0.50 A/cm^2. (b) Quantified evolution of cathodic peaks as function of time at various operating current density.

In order to correlate changes in electrode polarization with the structural changes, the phase transformation was studied via XRD before and after cell operation. First, a baseline was developed where phase transformation in PNNO was not influenced by electrochemical potential. **Figure 4a** shows that operation at 700 °C and 0.10 A/cm^2 for 300 hours does not lead to phase transformation, as shown by preserved parent phase (indicated with ●).

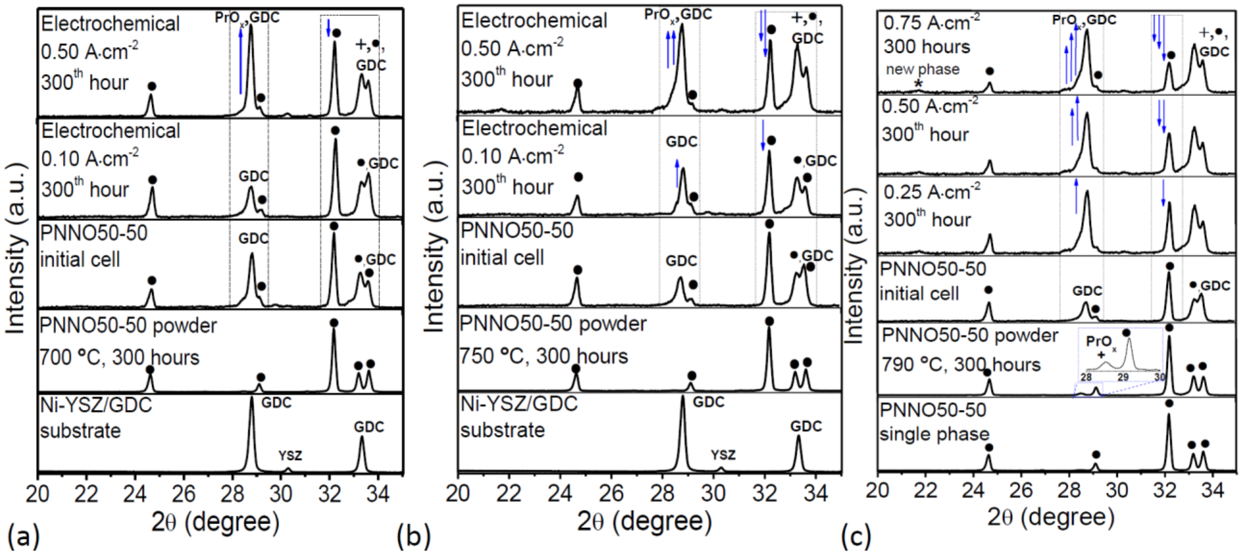

Figure 4. Phase evolution in PNNO electrodes operated under different current densities at (a) 700 °C, (b) 750 °C, and (c) 790 °C. Standard XRD patterns for Ni-YSZ/GDC substrate and PNNO powder are shown in (a) and (b).

However, once the current density is raised to 0.50 A/cm^2 a clear phase evolution follows with formation of PrO_x (+). Therefore, the phase transformation is evidently driven by the electrochemical potential and must not be overlooked when quantifying phase evolution in praseodymium nickelates. With greater confidence in the proposed theory, a systematic work at various temperatures and current densities was performed. **Figure 4b** shows phase evolution after electrochemical operation at 750 °C at 0.10 A/cm^2 and 0.50 A/cm^2. With increase in current density the phase transformation also increases. Similarly, the electrochemical tests in full cells at 790 °C show major phase transformation at 0.50 and 0.75 A/cm^2, **Figure 4c**. It is evident that with increase in current density the formation of PrO_x is promoted. Furthermore, the phase transformation can be further promoted at elevated temperatures, which may be due to increased mobility of oxygen ions in the structure.[12] It is imperative to note that thermally annealed PNNO powder (between 700 – 790 °C) does not show significant phase transformation after 300 hours. In fact, only ~1 mol. % of PrO_x is formed after 300 hours of annealing at 790 °C, **Figure 4c**.

Figure 5 summarizes quantified phase evolution in thermally annealed PNNO powder and electrodes, along with electrochemically operated cathodes. The plot was divided into two regions: (1) a region of thermally driven phase transformation, where thermodynamics dominates, and (2) a region of electrochemically driven phase changes, where electrochemical driving force dominates. After 500 hours of annealing at 790 °C both powders and electrodes (YSZ/GDC/PNNO configuration) show only a few percent of phase transformation. A 1-2% larger phase transformation in electrode was detected due to previously discussed reaction with GDC interlayer.[7] However, it is evident that the electrochemical operation significantly enhances phase transformation in PNNO. At 700 °C the electrodes operated at 0.50 A/cm^2 undergoes 10.6 % phase

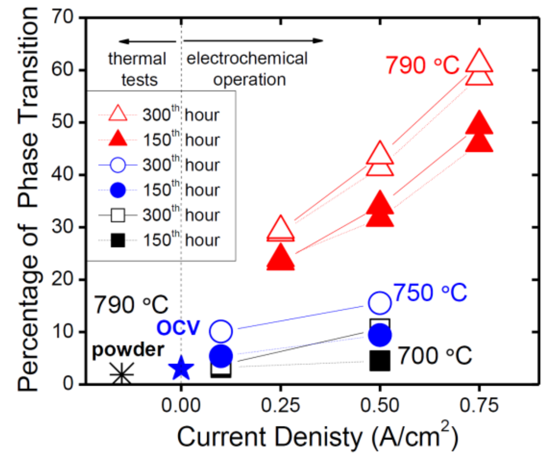

Figure 5. Quantified phase evolution in PNNO powders and electrodes. Powders and electrodes at OCV were thermally annealed at 790 °C for 500h in air. Phase evolution in electrochemically operated electrodes is illustrated as function of current density at various temperatures and operating times.

transformation. With further increase in temperature the phase transformation reached 15.5% at 750 °C and 0.50 A/cm^2. Even more evident results were obtained at 790 °C, where phase transformation was 60x larger than in thermal annealing studies at the same temperature. The baseline studies (0.10 A/cm^2 and 700 °C) which provided zero phase transformation also show enhanced phase degradation with increase in temperature and operation time, further indicating the magnitude of the driving force (electrochemical potential).

Based on these results, the formation of PrO$_x$ seems to be promoted with increase in current density. PrO$_x$ is formed due to oxidation of Pr^{3+} to Pr^{4+} since the effective nuclear charge on Pr cannot hold the *f* electrons as tightly as perhaps is the case for Nd^{3+}.[5, 13] This may explain why the phase transformation in Nd$_2$NiO$_4$ and (Pr$_{0.25}$Nd$_{0.75}$)$_2$NiO$_4$ does not occur even after electrochemical operation shown in **Figure 1**. However, with high Nd content in the structure, the activity of the electrode decreases substantially.[6] The generated Pr^{4+} in PNNO is too small to stabilize in the parent structure and leaves the lattice forming PrO$_x$, which has ~69% thermal mismatch (TEC=22.3 ppm)[14] when compared to PNNO phase. As a result, the local stress[15] in a material will be induced. During electrode operation more PrO$_x$ is generated and the area of the thermal mismatch increases, effectively leading to enhanced phase transformation. With increase in electrochemical potential across the electrode, the local oxidation and reduction occurs at a faster rate (2x higher phase transformation at 0.75 A/cm^2 vs 0.25 A/cm^2 at 790 °C, as illustrated in **Figure 5**), creating inhomogeneous phase and leading to enhanced phase transformation. Therefore, the obtained results seem to closely follow the proposed theory.

Figure 6a shows an SEM image of the cell cross section after operation. EDS analysis was performed on the three regions of the cell, from the GDC interlayer bulk to the cathode/interlayer interface. The quantification of the elemental composition in the three regions, with respect to cathode bulk, is shown in **Figure 6b**. Quantified percentage of Pr and Nd is illustrated against the cell held at OCV. There is a threefold increases of Pr and Nd diffusion into GDC interlayer with increase in current density from OCV to 0.75 A/cm^2, which further confirms enhanced phase transformation in PNNO electrodes.[7] It seems that electrochemical potential not only promotes the phase transformation, but also promotes the reaction with GDC interlayer, which could not be taken into consideration in thermal annealing tests on electrodes.

Figure 7a shows the microstructure of PNNO electrode before operation. After operation and with increase in current density the porosity of the electrode decreases, as illustrated in **Figures 7b-d**. The results indicate that electrode microstructure can also be electrochemically manipulated. The TEM analysis shows a single PNNO phase before electrode operation, **Figure 8a**. After thermal annealing at 790 °C for 500 hours a formation of contrasted phases indicates some formation of

PrO_x, **Figure 8b**. **Figure 8c** shows that after electrochemical operation at 0.75 A/cm^2 for 150 hours the contrasted regions are clearly separated, indicating presence of multiple phases. With increase in operation time (**Figure 8d**) the nanoclusters are formed, which have been addressed in more detail previously and are associated with the active PNNO phase. Elemental mapping on electrodes operated at 0.75 A/cm^2 for 300 hours is shown in **Figure. 9**. STEM analysis in **Figures 9c-f** show fully extruded PrO_x and NiO phases, along with majority of the PNNO phase throughout the electrode bulk. Hence, the TEM results confirm that the phase transformation can be electrochemically enhanced, which supports the studies shown in **Figures 4** and **5**.

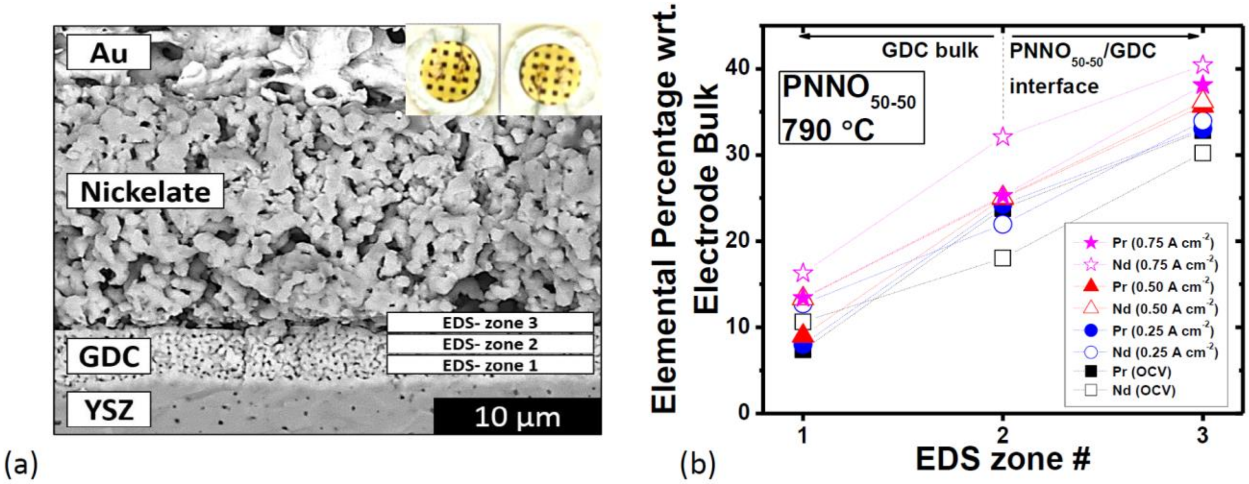

Figure 6. (a) A cross section image showing the configuration for all cell components. The three highlighted regions were used for quantification of elemental composition. Insert image shows an exposure window through Au grid for phase quantification studies. (b) Quantified elemental distribution of Pr and Nd at the three regions shown in (a).

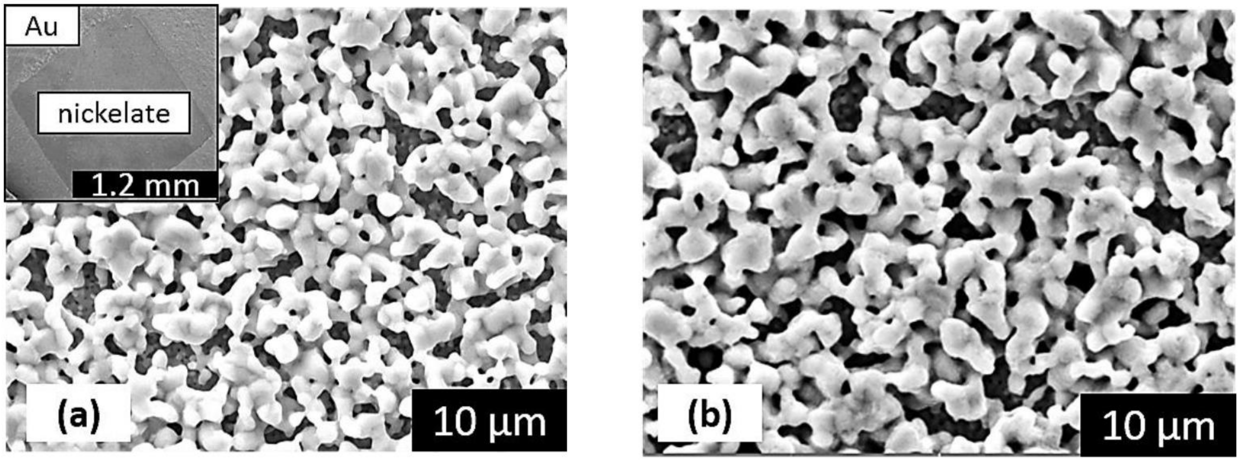

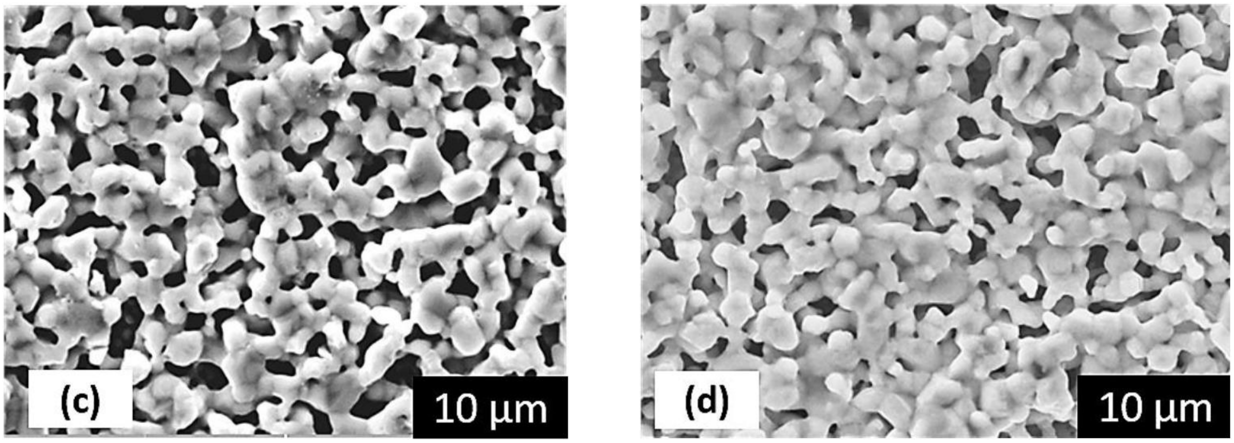

Figure 7. SEM images of the electrodes before operation (a) and after 300 hours of operation at 790 °C at (b) 0.25 A/cm^2, (c) 0.50 A/cm^2, and (d) 0.75 A/cm^2.

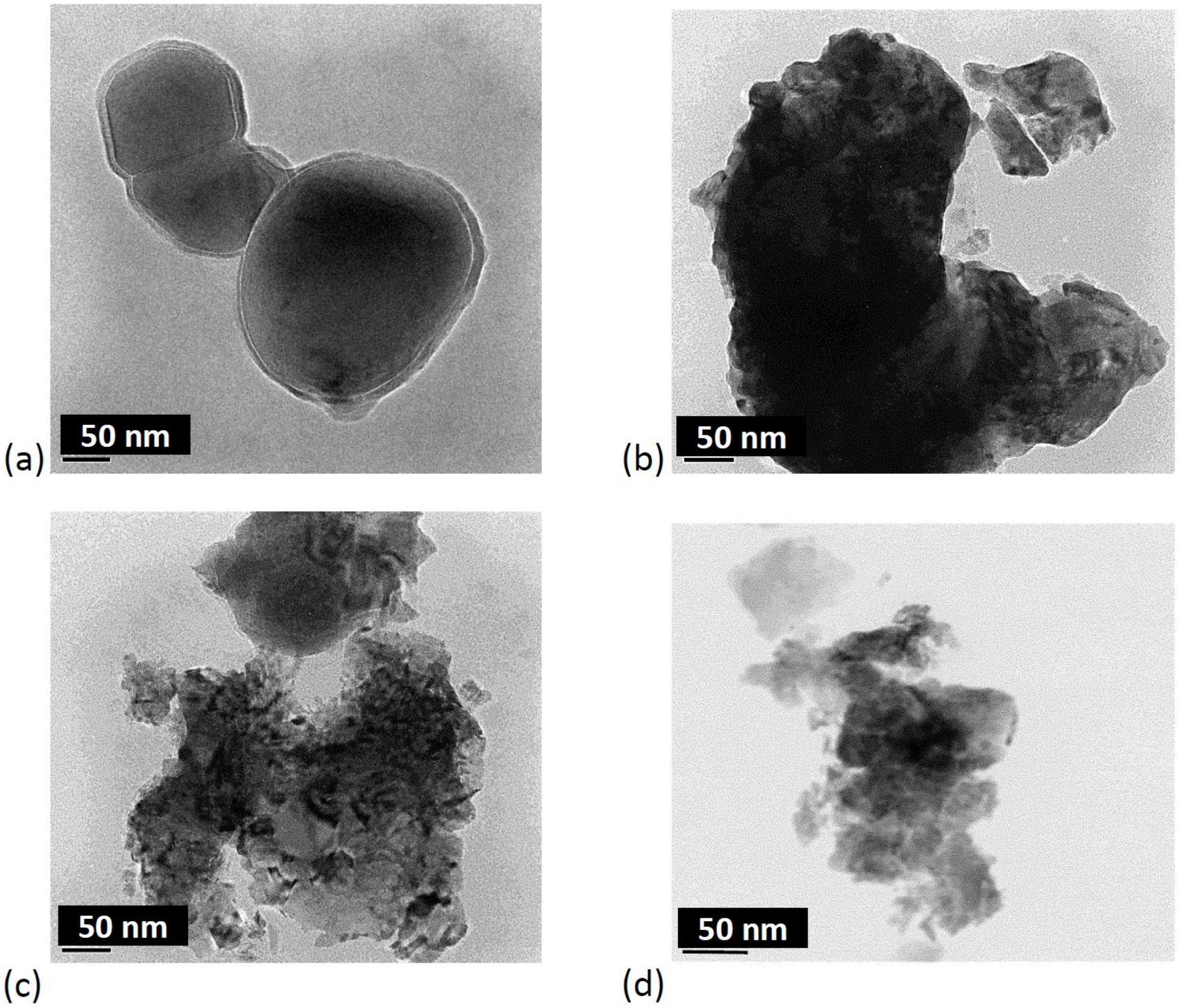

Figure 8. TEM images on PNNO electrodes (a) before operation, (b) after thermal annealing at 790 °C for 500 hours, and (c-d) after electrochemical operation at 0.75 A/cm^2 for 300 hours at 790 °C.

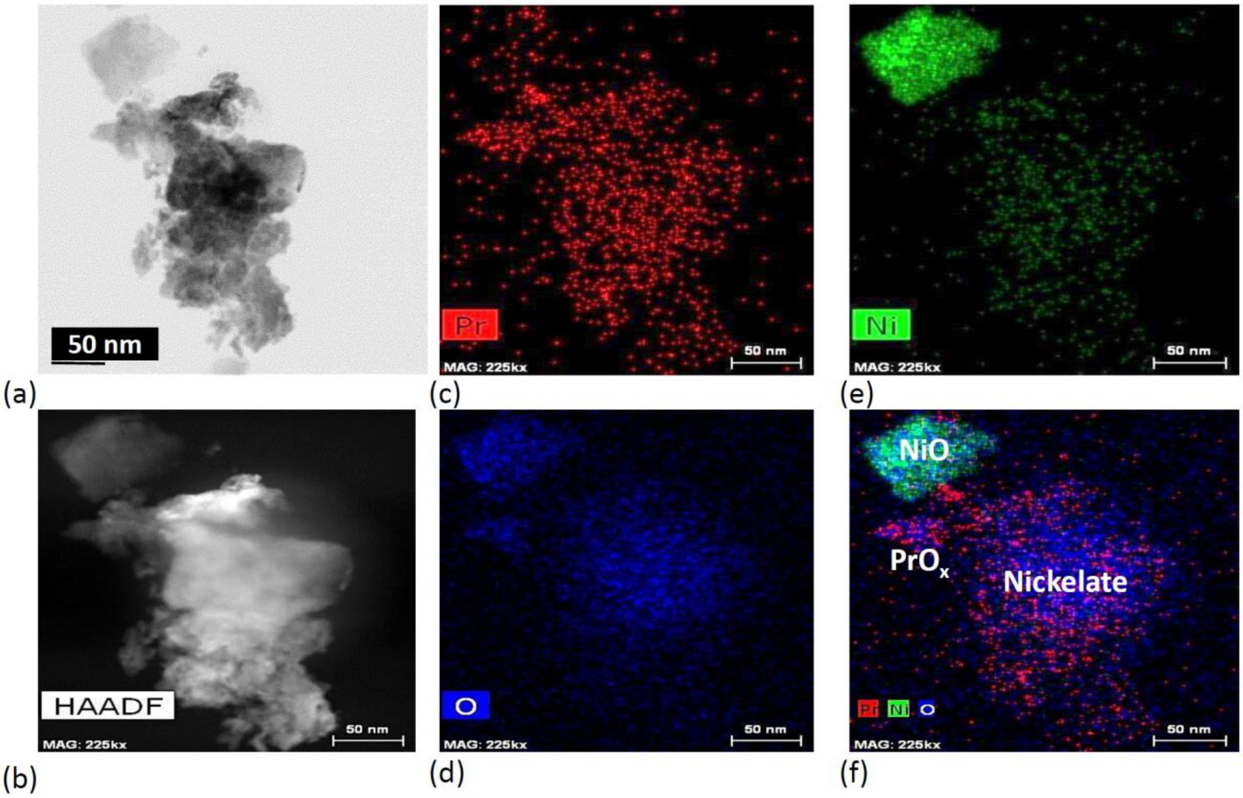

Figure 9. (a-b) TEM images on PNNO electrodes after electrochemical operation at 0.75 A/cm^2 for 300 hours. (c) to (f) are elemental maps of the electrode after operation shown in (a-b).

B.3.2 Accelerated Test Protocols for Nickelates

Figure 10 shows quantified phase transformation in PNNO electrodes at various temperatures during thermal annealing and electrochemical operation. Quantification of the phase evolution was performed by a least squares fitting of the linear combination of XRD standards against the experimental patterns.[5, 16] The least squares method was used to generate the LCOS using the following equation, $COS = \sum_i \alpha_i \cdot Std_i$, where i is the index of a given standard, α_i is a scale coefficient for the i th pattern, and Std_i is the i th standard XRD pattern. The least squares method was then used to minimize the residual $(\sum_\theta (Exp - LCOS)^2)$ between the difference of experimental XRD patterns (Exp) and LCOS over the 2θ region of interest.

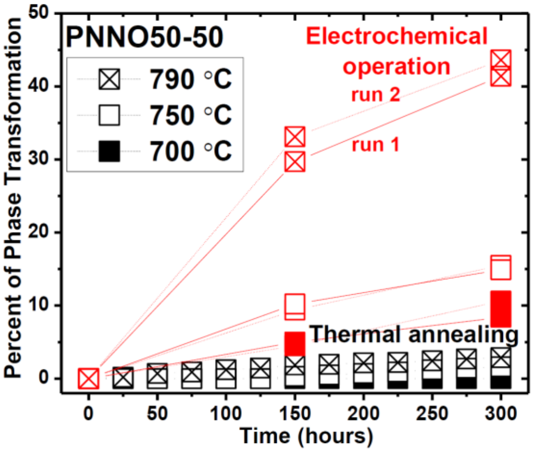

Figure 10. Quantified phase transformation in PNNO electrodes undergoing thermal annealing and continuous electrochemical operation at 0.50 A/cm^2 at various temperatures including 700 °C, 750 °C, and 790 °C. Multiple runs with full cells were conducted to ensure reproducibility.

It can be clearly seen that electrochemical operation at all temperatures promoted phase transformation. At 700 °C and 750 °C the thermal annealing on electrodes shows preserved parent phase. However, with electrochemical operation at 0.50 A/cm^2 the phase transformation increases to 12% after 300 hours. Even more evident is the operation at 790 °C, where phase transformation reaches remarkable 40%, which is 40x increase when compared to thermal annealing studies at 790 °C for 300 hours. It was found that with an increase in current density the phase transformation was further promoted. Having confirmed the electrochemically driven phase transformation behavior in PNNO, an approach was taken to further accelerate the cell life.

Since SOFCs are targeted for ~40,000 hour operation (5 years) with only a few percent degradation per thousand hours, finding a way to screen materials in a faster and more effective way is highly desired. Since thermal annealing studies show only~1% phase transformation in PNNO after 500 hours of annealing at 790 °C,[7] finding the ways to accelerate the phase transformation is of outmost importance as phase transformation has been previously linked to performance degradation in praseodymium nickelates.[6] Having confirmed that electrochemical potential can indeed promote phase transformation, the accelerated test protocols (ATPs) were developed to simulate and mimic the long-term cell operation (10,000-20,000 hours) in significantly shorted periods of time (1,000-2,000 hours).

B.3.2.1 Initial Performance and Cell Reproducibility

Figure 11a shows i-V and power density curves for PNNO cell at temperatures between 600 - 850 °C. The power density reaches 0.70 W/cm^2 at 750 °C, 0.87 W/cm^2 at 800 °C, and over 1 W/cm^2 at 850 °C. In order to ensure accuracy of the results multiple cells were tested as each operating condition, as shown in **Figure 11b**. The i-V curves for the three PNNO cells are within a good agreement (1-2% difference). The measured open circuit voltage (OCV) of 1.10 ± 0.04 V shows reproducible and quality seals, which is in good agreement with other reports. **Figure 11c** show power density as function of temperature at 0.80 V for multiple cells. With increase in temperature from 650 °C to 850 °C the power density increase by fourfold. Higher operating temperatures are desirable for PNNO electrode to enhance oxygen reduction reaction (ORR) and ionic transport.[6-7]

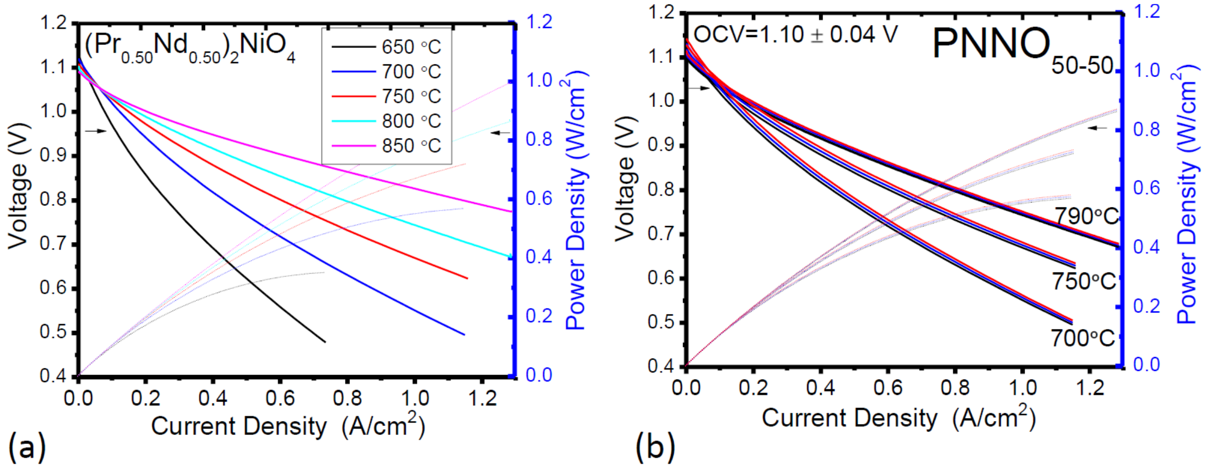

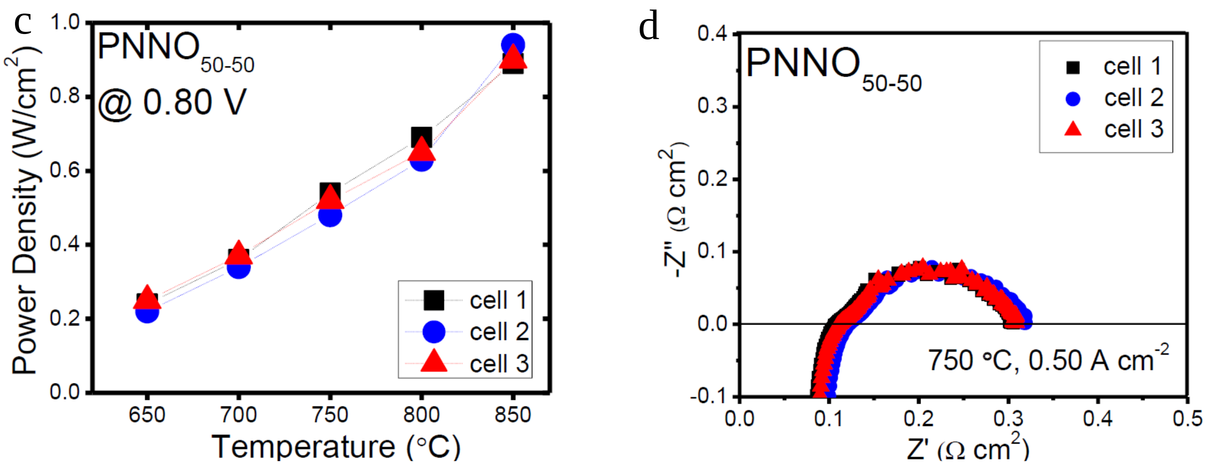

Figure 11. (a) i-V and power density curves in PNNO cells measured at various temperatures. (b) Performance reproducibility with multiple PNNO cells measured at 700 °C, 750 °C, and 790 °C. (c) Power density as function of temperature at 0.80 V for multiple PNNO cells. (d) EIS spectra at 750 °C and 0.50 A/cm^2 on multiple PNNO cells.

Figure 11d shows in operando AC impedance spectra on three PNNO cells at 750 °C and 0.50 A/cm^2. Consistent ohmic resistance (R_{ohm}) of 0.1 $\Omega \cdot cm^2$ indicates reproducible manufacturing technique and stable interfaces. The polarization resistance (R_{pol}) of electrode is 0.21 $\Omega \cdot cm^2$, which is a reasonable value for PNNO electrode at intermediate temperature. By obtaining the required cell reproducibility, which eliminates the effects of variations in R_{ohm} and R_{pol} between the cells, the application of ATPs was justified. The role of ATPs on performance stability and phase transformation in PNNO was studied in great detail.

B.3.2.2 Accelerated Test Protocols- Performance Stability and DRT Analysis

Figure 12 shows the performance stability as function of time at various current densities (0.25 A/cm^2, 0.50 A/cm^2, and 0.75 A/cm^2). PNNO cells operated under constant current density show stable operation after 300 hours at 790 °C. However, ATPs show clear performance degradation (up to 4%/1,000 hours) at all current densities. With increase in current density the rate of performance degradation with ATPs increases (by threefold at 0. 75 A/cm2 when compared to 0.25 A/cm^2 cycling). It may also be advantageous to mention that PNNO operation at 750 °C and 0.80 V only showed 0.25%/1,000 hours degradation.[6] Hence, with ATPs the performance degradation in PNNO was accelerated by 16x.

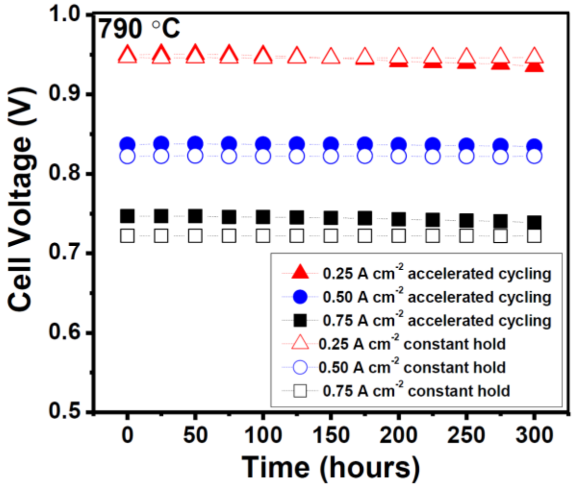

Figure 12. Cell voltage as function of time for various current density values including 0.25 A/cm^2, 0.50 A/cm^2, and 0.75 A/cm^2 at 790 °C for 300 hours. Constant hold vs. accelerated protocols were compared.

Distribution of relaxation times (DRT) analysis[8-11] of EIS spectra is shown in **Figure 13**. **Figure 13a** illustrates four peaks, where P1c-P3c are associated with cathodic processes and P4a is an anodic peak, as described in detail in one of the previous studies.[6] Evolution of in operando DRT spectra for a cell held at constant current density of 0.75 A/cm^2 shows minor changes in the peaks after 300 hours of operation. However, a quantified peak area shows some increase in P3c and P2c peaks. On the other hand, the cell undergoing ATPs at 0.75 A/cm^2 shows significant changes in DRT spectra, **Figure 13b**. **Figures 13c-d** show 4.3% increase in P3c and 2.4% increase in P2c along with shifts to higher frequency. Such changes in cathodic peaks are associated with increase in resistance for overall ORR, which can be linked with phase transformation in PNNO.[6-7] The accelerated increase in R_{pol} (cathode) becomes evident when compared to constant operation. Therefore, to provide a link between the changes in electrode resistance and performance degradation, a detailed phase evolution analysis was performed on full cells before and after electrochemical operation. It is also imperative to note that the previously conducted *in-situ* studies at a synchrotron source on PNNO electrodes showed that the quantity of phase transformation at operating conditions in full cells is in agreement to phase transformation recorded upon cooling. Hence, the quantification of phase transformation in praseodymium nickelates after operation is justified and reflects the actual phase evolution behavior in full cells.

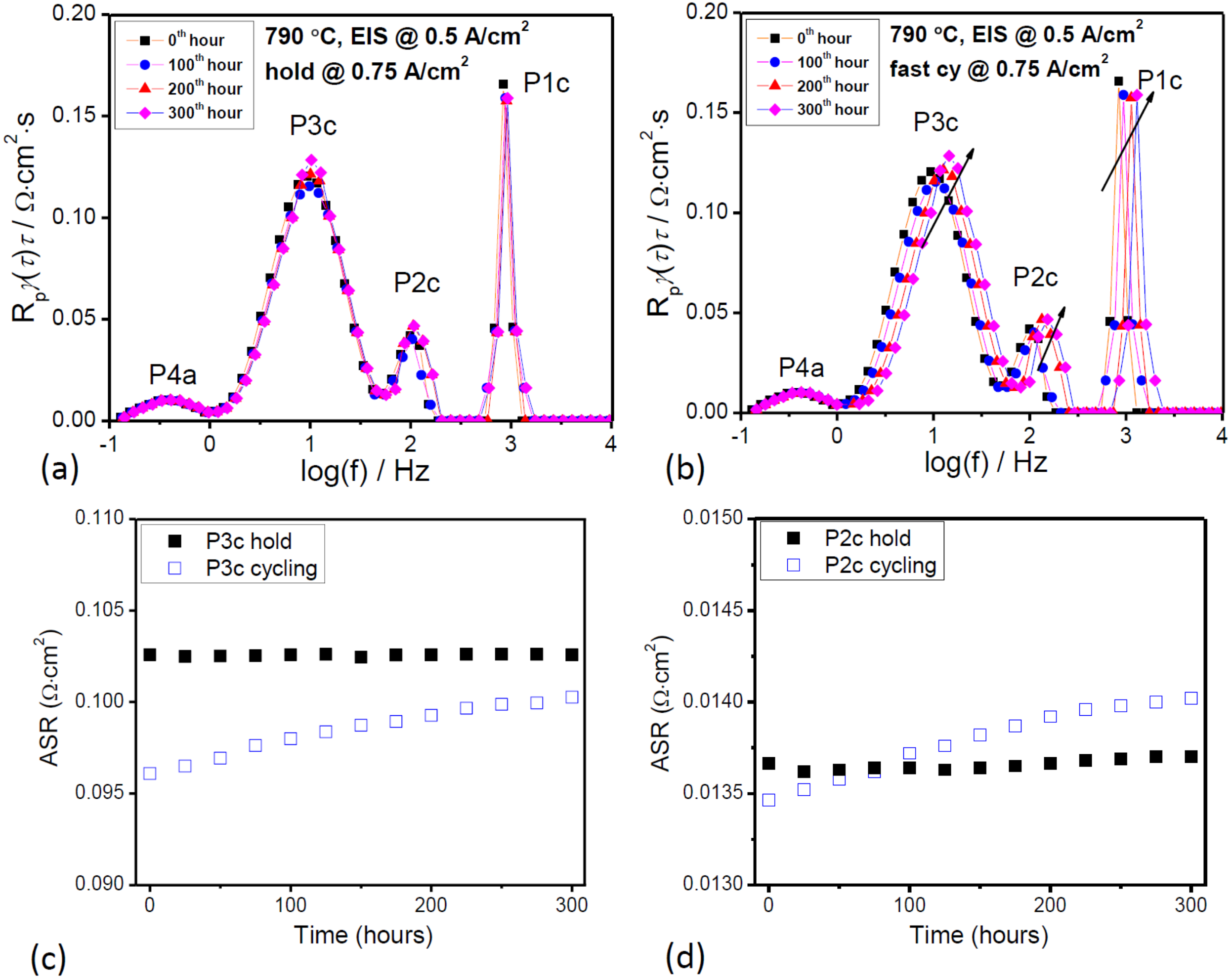

Figure 13. In operando (at 0.50 A/cm^2) DRT analysis as function of time on (a) cell operated at constant current density of 0.75 A/cm^2 for 300 hours, and (b) cell undergoing accelerated cycling at 0.75 A/cm^2. Quantified (c) P3c peak area, and (d) P2c peak area as function of time for both testing methods.

The role of ATPs on phase transformation in PNNO electrodes is illustrated in **Figure 14**. **Figure 14a** shows XRD patterns on common standards along with initial full cell. The parent layered structure can be clearly seen (marked as ●). After constant operation at 0.75 A/cm^2 for 150 hours at 790 °C, the phase transformation occurs showing decrease in intensity of nickelate peaks along with formation of PrO_x (+). **Figure 14b** shows initial and final XRD diffraction patterns on the cell undergoing ATPs at the same conditions. The phase transformation is substantially higher, with the parent nickelate peaks being overshadowed with formation of PrO_x and a higher order $Pr_3Ni_2O_7$ and $Pr_4Ni_3O_{10}$ phases (marked as x, as indicated by evolution of new peaks in 2θ region of 22-27°). Furthermore, the operation after 300 hours (**Figure 14c**) shows further phase transformation, arrows on the highest intensity nickelate peak ($2\theta=32.15°$) show the magnitude of phase transformation with ATPs. In addition, another new peak evolves at $2\theta=27.5°$ further indicating the formation of higher order $Pr_4Ni_3O_{10}$ phase. The $Pr_4Ni_3O_{10}$ phase is known to have a number of distinctive reflections[17] between 20-27° while the $Pr_3Ni_2O_7$ mainly overlaps with the PNO phase.[2] Vibhu et al.[17] showed that $Pr_4Ni_3O_{10}$ electrode could potentially have high activity in SOFCs under oxidizing conditions, however the phase transformation after electrochemical operation was not reported. Furthermore, the highest intensity PrO_x reflection directly overlaps with $Pr_4Ni_3O_{10}$ phase further questioning the initial phase purity. Instead, thermal annealing studies at 800 °C for one month on $Pr_4Ni_3O_{10}$[17] were performed and showed some phase transformation and formation of PrO_x. Accelerated phase evolution and the mechanism of phase transformation in praseodymium nickelates show that ATPs performed in this work may provide further insights on the complexity of the system in a significantly shorter time frame. It is also imperative to note that cell operation under constant current density does not yield formation of $Pr_4Ni_3O_{10}$ phase, hence the ATPs may shed a light on an additional phase transformation mechanism(s) in SOFCs that are otherwise occurring extremely slowly under constant current density, hence are almost never detected.

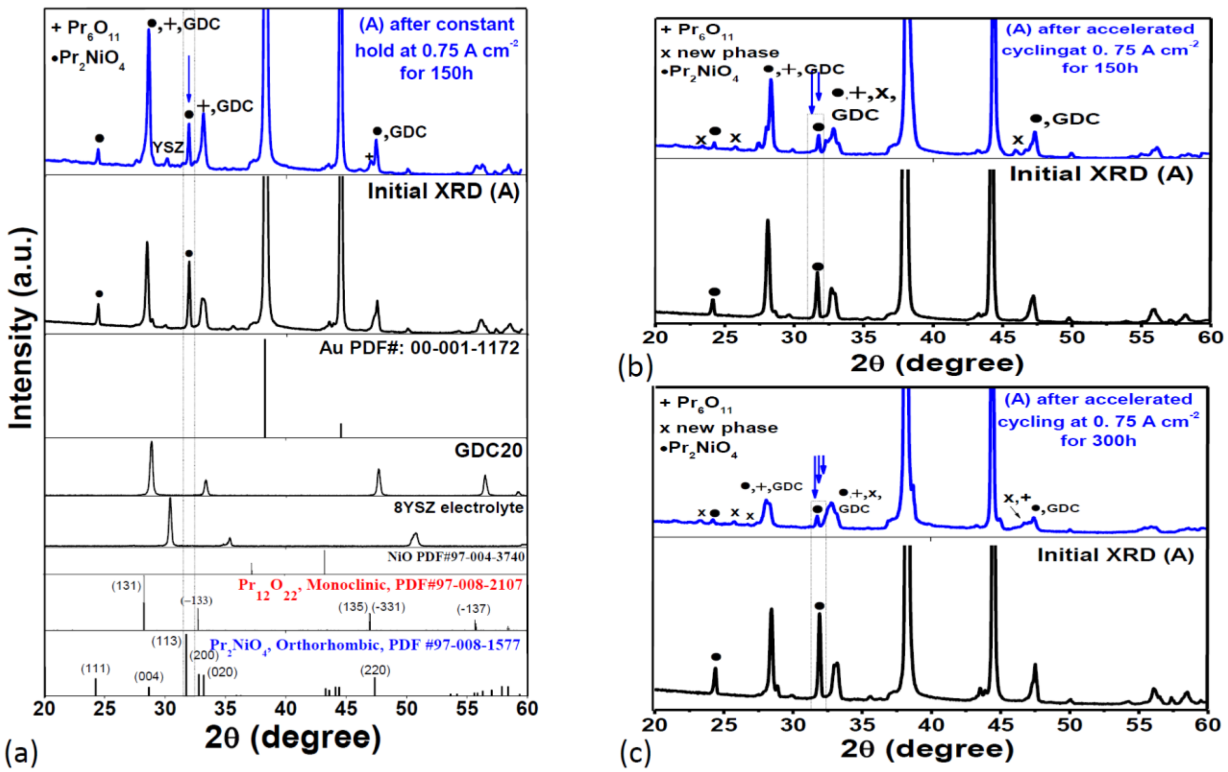

Figure 14. XRD patterns on PNNO electrodes in full cells before and after electrochemical operation at: **(a)** constant current density of 0.75 A/cm2 for 150 hours, **(b)** cycling current density of 0.75 A/cm2 for 150 hours, and **(c)** cycling current density of 0.75 A/cm2 for 300 hours. Standard XRD patterns for each cell component and possible products are shown in (a).

The effectiveness of ATPs on the phase transformation in praseodymium nickelates is best illustrated through the quantitative analysis. **Figure 15** shows quantified phase evolution in thermally annealed PNNO powder and electrodes, along with electrochemically operated cathodes undergoing standard operation (constant current injected for the duration of experiments) and ATPs with alternating current injection (2 seconds at selected current, and 1 second at OCV). The plot was divided into two regions: (1) a region of thermally driven phase transformation where thermodynamics dominates, and (2) a region of electrochemically driven phase changes, where electrochemical driving force dominates. The standard electrochemical operation leads to significantly lower phase transformation when compared to ATPs. Even after only 150 hours of operation the rate of phase transformation in full cells was accelerated by additional 50% with ATPs. With increase in operation time, the power of ATPs was further demonstrated by 67% increase in phase

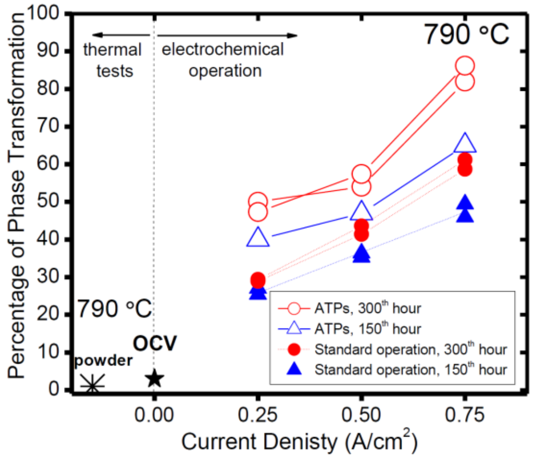

Figure 15. Quantified percentage of phase transformation on PNNO powders and electrodes undergoing thermal annealing tests and two types of electrochemical operation: (1) constant hold, and (2) accelerated tests at various current densities and time.

transformation when compared to standard electrochemical operation. Evidently the ATPs are a promising avenue in electrode evaluation, which take into account the role of electrochemical potential on phase transformation in praseodymium nickelates.

The transformation of parent PNNO phase is clearly promoted with electrochemical operation and increase in current density. Furthermore, ATPs can further accelerate phase transformation by enhancing the net current of cations (in particular the Pr^{4+} formed during phase transformation, which is too small to stabilize in the parent structure and effectively leaves the lattice and forms the PrO_x and higher order phases). Such effect is commonly overlooked in short-term measurements due the absence of a significant driving force ($-\nabla\mu_i$). By simulating the prolonged operations and stimulating the net current of cations in the structure, ATPs can provide fundamental knowledge of electrode and system behavior in a fraction of the time and cost when compared to long-term thermal annealing studies and standard cell operation.

B.3.2.3 Accelerated Phase Transformation in PNNO and NNO

Figure 16 shows the SEM images of the electrode microstructure before and after electrochemical operation in full cells. Initial cell microstructure (**Figure 16a**) is consistent among all cells, as previously discussed.[7] After electrochemical operation for 150 hours under constant current density the microstructure changes significantly leading to substantial decrease in porosity. With increase in current density, the larger the microstructural changes are.

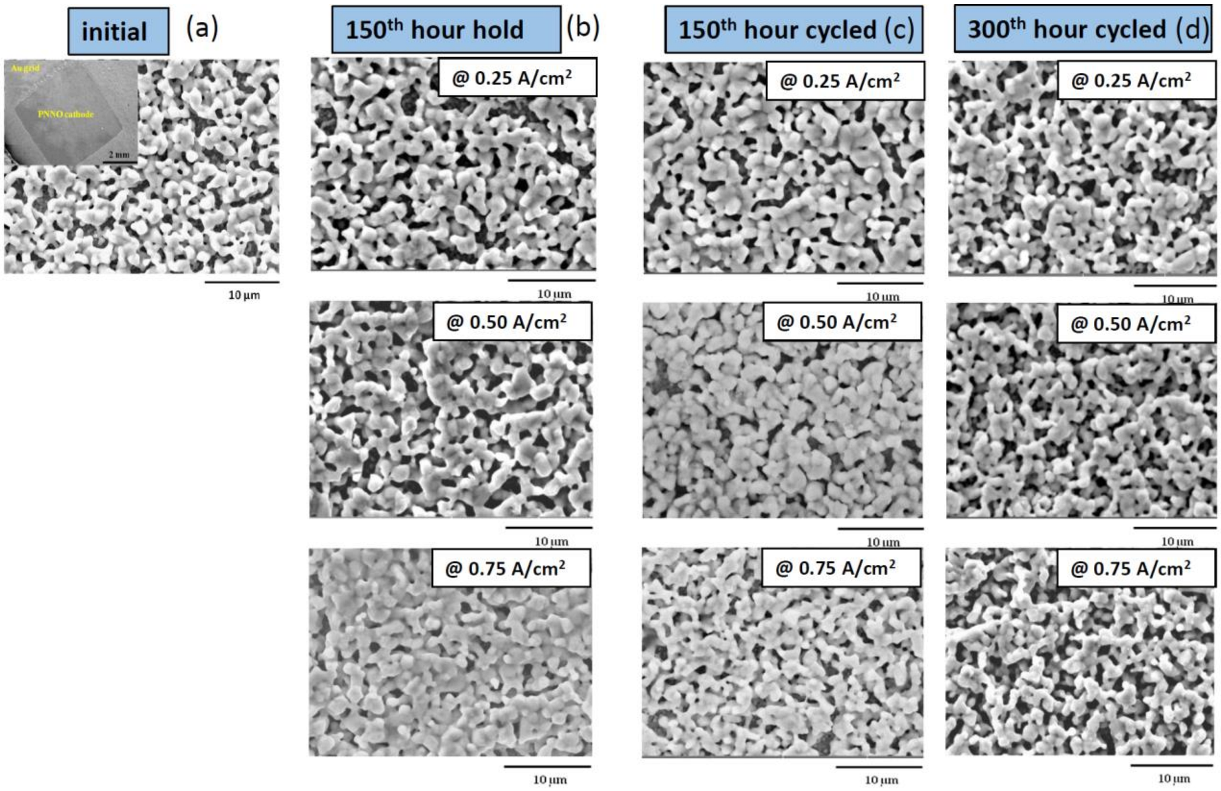

Figure 16. SEM images of the electrode surface before (a) and after electrochemical operation. (b) Cell microstructure after holding at constant currents for 150 hours, (c) after ATPs for 150 hours, and (d) after ATPs for 300 hours.

With ATPs (**Figure 16b**) the changes in microstructure are significantly accelerated showing promoted densification at lower current density. With 300 hour ATPs the microstructural changes are rather startling. Although some densification is evident, it seems that porosity increased (when compared to 150 hour ATPs) and the microstructure is very comparable to the initial cells. This may indicate an additional mechanism in microstructural changes driven by ATPs. It is also imperative to note that TEM analysis is required in order to fully understand the mechanisms behind phase transformation and electrochemical performance. HR-TEM studies showed that nano-cluster matrix of the parent phase was formed through the entire electrode bulk, which was linked to retained electrode activity.

Figure 17 shows TEM analysis on PNNO electrodes, which demonstrates more detailed microstructural changes. **Figures 17a-b** show initial homogeneous phase distribution in PNNO. After electrochemical operation at constant current density for 150 hours (**Figures 17 c-d**) multiple contrasted phases are formed, which are indicative of formation of PrO_x and NiO as byproducts of phase transformation.[7] However, with ATPs at 0.50 A/cm^2 for 150 hours (**Figures 17e-f**) and 300 hours (**Figures 17g-h**) the formation of nano-matrix is significantly promoted, indicating accelerated phase transformation in PNNO.

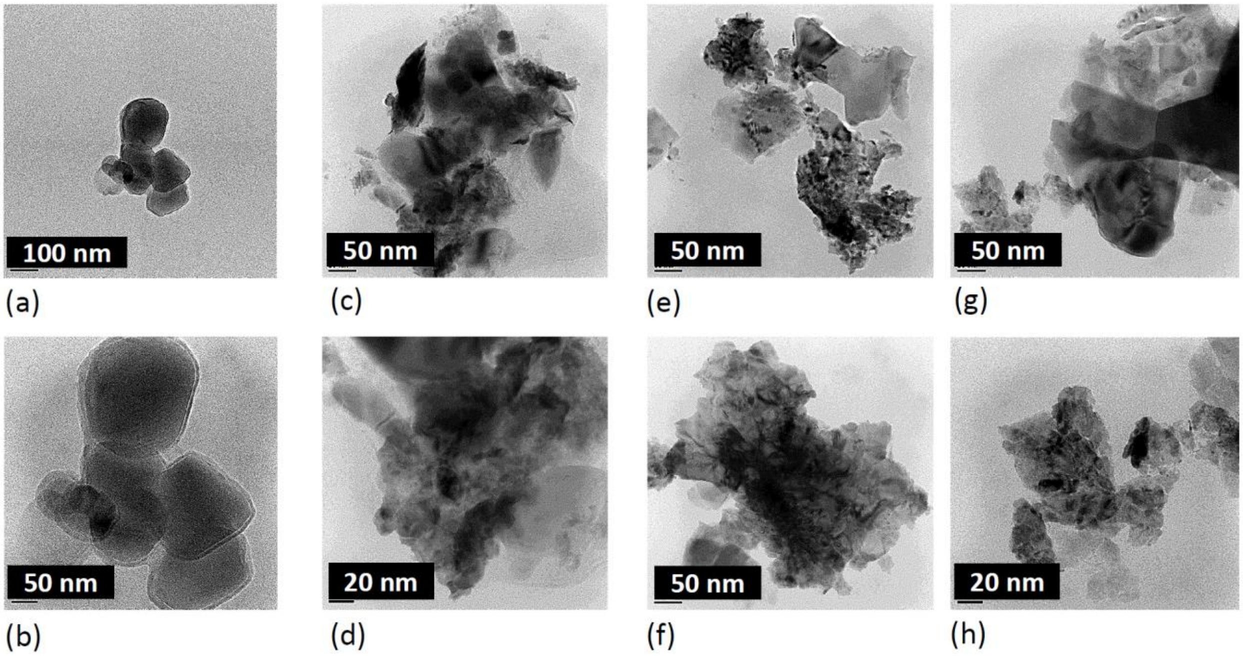

Figure 17. TEM images of PNNO electrode before operation (a-b), and after electrochemical operation at 790 ° C and 0.50 A/cm^2 for cells held at constant current for 150 hours (c-d), undergoing ATPs for 150 hours (e-f), and undergoing the ATPs for 300 hours (g-h).

Figure 18a shows the cross section SEM image of a PNNO cell along with designated EDS zones used for pseudo-quantification of elemental interdiffusion. Summarized elemental distribution at the PNNO/GDC interface and GDC bulk is shown in **Figure 18b**. The cells were operated at 790 C at OCV and 0.75 A/cm^2 (hold, ATPs for 150 hours, and ATPs for 300 hours). It is evident that the reaction between the PNNO and GDC is promoted by threefold with ATPs after 150 hours, and by sixfold after 300 hours. These findings indicated that ATPs indeed accelerate the phase transformation, microstructural changes, and reactions at the interfaces. Such findings allow to simulate cell operations in a fraction of the cost and time.

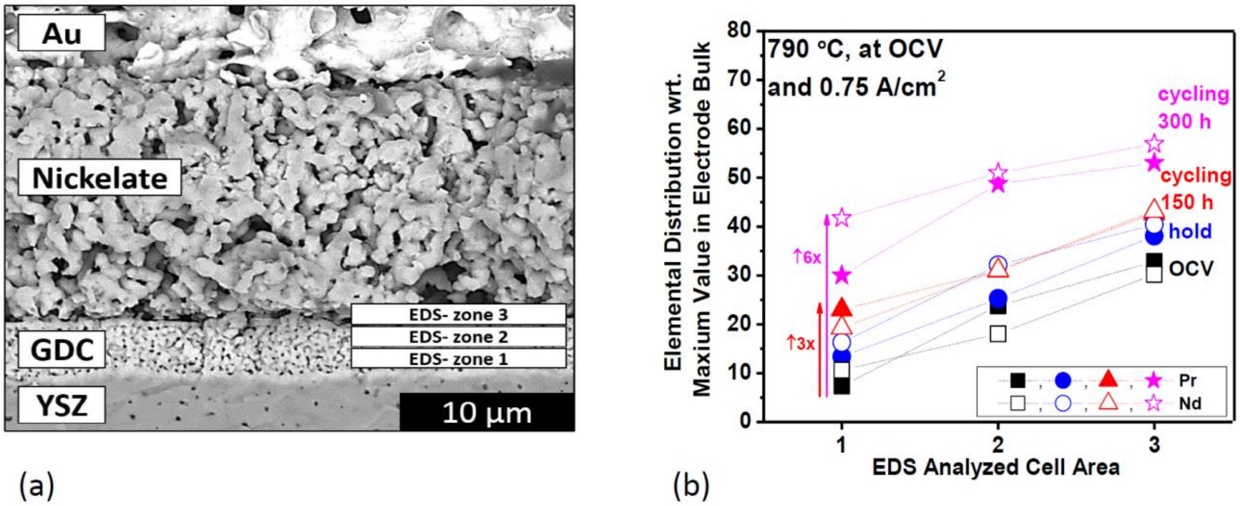

Figure 18. (a) SEM image of a cell cross section showing the cell components along with the three EDS zones used for elemental distribution analysis. (b) Elemental distribution analysis at PNNO/GDC interface and GDC bulk.

To further attest the capacity of ATPs, a highly stable Nd_2NiO_4 (NNO) electrodes[6-7] were also investigated. Thermal annealing studies (up to 2,500 hours) on NNO electrodes at the temperature range between 700-790 °C for did not show any phase transformation in air.[7] Furthermore, electrochemical operation at 0.80 V and 750 °C showed preserved NNO phase after 500 hours of operation with 0.06%/1,000 hour performance degradation.[6]These results show the rigidity of the NNO phase and stable Nd^{3+} oxidation state, which stems from high effective nuclear charge holding the *f* electrons tightly bound and less available for orbital overlaps. The retained performance stability can be linked to stable NNO phase. However, ATPs on NNO electrodes in full cells show a remarkable tenfold increase in performance degradation (0.37%/1,000 hours) after 1,100 hour operation at 750 °C and 0.25 A/cm^2, **Figure 19a**.

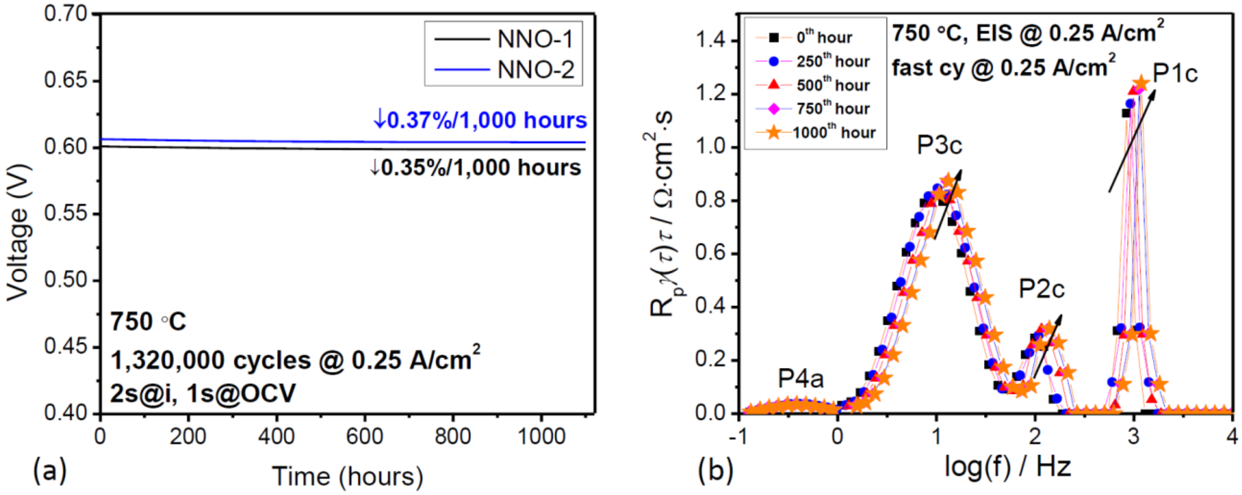

Figure 19. (a) Voltage vs. time for NNO cells operated at 0.25 A/cm^2 and 750 °C for 1,100 hours. ATPs result in over one 1.3 million cycles within 1,100 hours of operation. Two NNO cells were measured to ensure reproducibility. **(b)** In operando (at 0.25 A/cm^2) DRT analysis on NNO cells as function of time.

Two NNO cells show reproducible degradation rates. The DRT analysis confirmed increase in cathode ASR, as can be seen from the increase in area of cathodic peaks and shifts to higher frequency, **Figure 19b**. Even more evident effects of ATPs are shown in phase transformation studies in **Fig. 20**. The XRD analysis on operated NNO electrodes shows clear phase transformation with formation of Nd_2NO_3 oxide and an additional nickelate phase. A possible mechanism is the formation of a higher order phase (*, not reported in the literature), as $NdNiO_3$ reflections do not match the newly emerged peaks in the 2θ range between 20-25°. The results further attest to effectiveness of ATPs on the entire $(Pr_{1-x}Nd_x)_2NiO_4$ series.

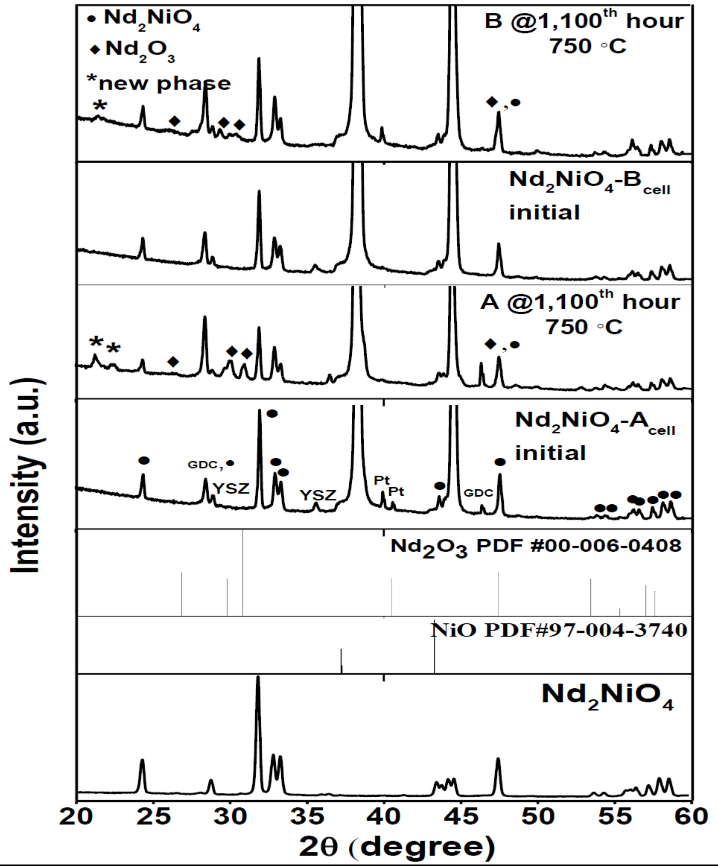

Figure 20. XRD patterns on two NNO electrodes in full cells before and after accelerated electrochemical operation at 0.25 A/cm^2 for 1,100 hours. Standard XRD patterns for NNO, NiO, and Nd_2O_3 products are shown on the bottom.

B.3.3 Accelerated Test Protocols for LSCF

B.3.3.1 Baselines for Reliability and Reproducibility Studies

Figure 21a shows high throughput stands which were used to study the reproducibility of measurements and gain statistical significance of analysis. On average, the power variability was within 10%, indicating good reproducibility of the cell fabrication and test assembly process, as shown in **Figures 21 b** and **c**.

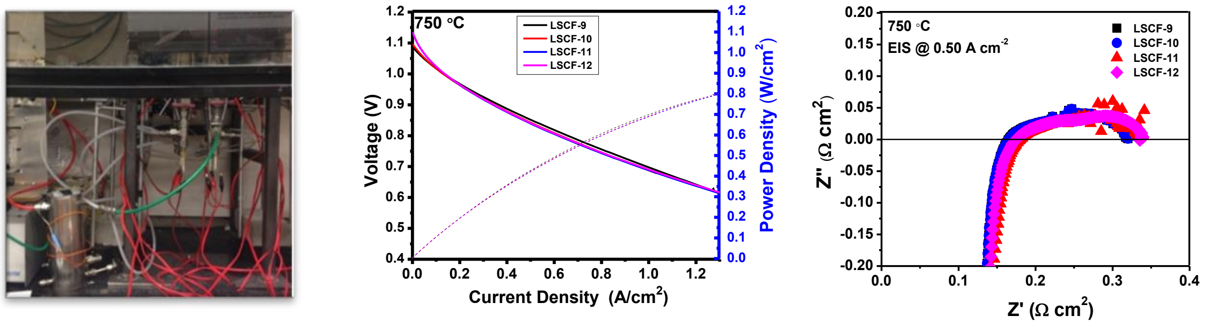

a b c

Figure 21. (a) High throughput fuel cell test stands. Six stands were held in one furnace. The electrochemical performance (b) and EIS (c) of four LSCF-based cells, showing similar results, which enable us to study the cycling effect on the performance stability.

B.3.3.2. Accelerated Test protocols for LSCF-based SOFC

Initial research focused on acquiring the baseline results by applying a constant current on LSCF-based cells. Multiple cells were used to study the data reproducibility. Two current densities were used, 0.5 and 1.0 A/cm^2. **Figures 22a** and **b** show an increase in the ohmic area specific resistance (ASR) as a function of time. The higher current density leads to a faster increase in the ohmic ASR, suggesting the degradation rate of cell performance increases with increasing operation current. **Figures 22c** and **d** show the evolution of ohmic ASR vs. time under cycling. Two cells (**Figures 2c** and **d**) were used with the same experimental conditions. Results were reproducible. **Figure 22e** shows a summary of the percentage increase of the ohmic ASR as a function of time for the cells cycling at various conditions and **Figure 22**(f) is a comparison of effects of operation temperature (750 vs. 850 °C) on the performance degradation. Results shown in **Figures 22 (a)** to **(e)** were obtained 750 °C. The increase in ohmic resistance is accelerated during cycling. Here are a few summaries of results shown in **Figure 22** and listed in **Table I**: (1) during the steady-state operation, a higher operation current (1 A/cm^2) results in a larger increase in the ohmic resistance; (2) cycling accelerates the increase in ohmic ASR. The acceleration effect is more dominant with a higher cycling current, faster cycling frequency, or a higher operation temperature (e.g. 850 °C).

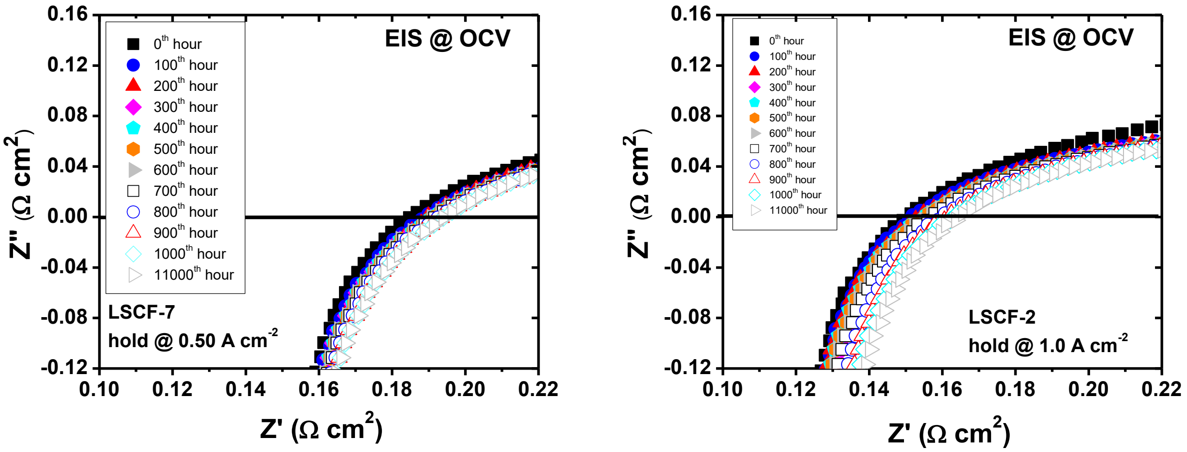

a b

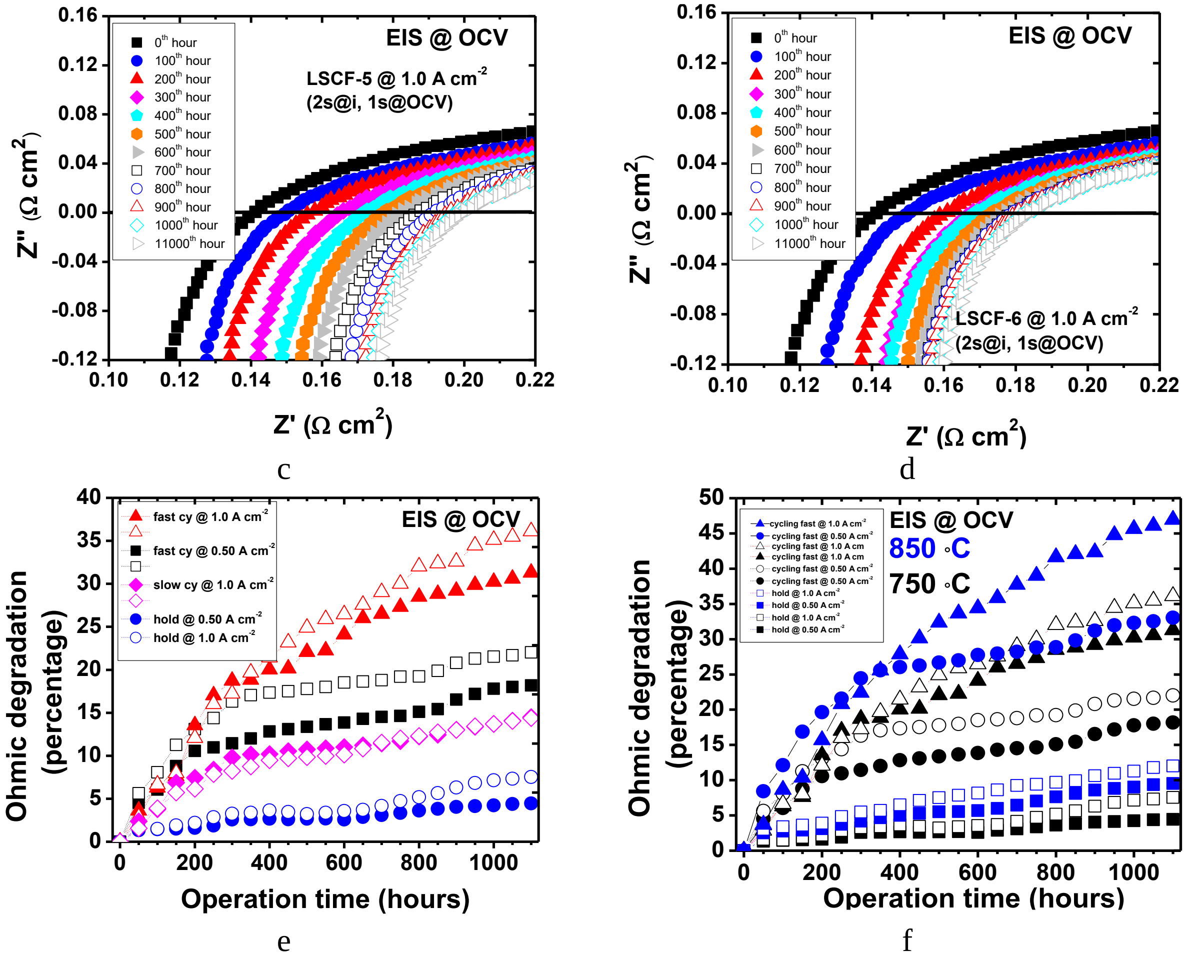

c

d

e

f

Figure 22. The evolution of EIS spectra of LSCF-based cells under a constant current operation, 0.5 A/cm^2 (a) and 1 A/cm^2 (b). The evolution of EIS spectra of two cells which were operated at 1 A/cm^2 for 2-sec, then held at OCV for 1-sec, up to 1,100 hours. (c) and (d). (e) A summary plot of the percentage increase of ohmic ASR as a function of time for the cells cycling at various conditions. (f) A comparison of operation temperature on the cycling effects between 750 and 850 ºC. **(a) to (e) were acquired at 750 ºC.**

Table 1. Percentage of the increase in ohmic ASR and degradation of cell power density (PD) as a function of time for LSCF-cells at 750 ºC.

Operating conditions	Comments, Ohmic ASR and Power Density (PD)		H_2O % air	250 hour	600 hour	1100 hour
Hold @ 0.50Acm^{-2}	Baseline, low current (J)	Ohmic	0.6	1.9	2.6	4.5
		PD		1.3	2.3	3.6
Hold @ 1.0 Acm^{-2}	Baseline, high current (J)	Ohmic	0.6	2.9	3.5	7.5
		PD		1.8	4.0	6.5
cycling @ 0.50A·cm^{-2}; 2s@loading, 1s@OCV	Fast cycle; low *J*	Ohmic	0.6	11.0	13.7	18.2
		PD		4.2	8.4	13.3
cycling @0.50A·cm^{-2}; 2s@loading, 1s@OCV	Fast cycle; low *J*	Ohmic	0.6	14.4	18.5	22.0
		PD		4.2	8.3	13.2
cycling @ 1.0 A·cm^{-2}; 2s@loading, 1s@OCV	Fast cycle; high *J*	Ohmic	0.6	17.0	24.1	31.2
		PD		5.6	11	17.4
	Fast cycle; high *J*	Ohmic	0.6	16.0	26.5	36.0

cycling @ 1.0 A·cm^{-2}; 2s@loading, 1s@OCV		PD		5.6	11	17.5
cycling @1.0A·cm^{-2}; 20s@loading, 5s@OCV	Slow cycle; high *J*	Ohmic	0.6	8.4	10.1	14.0
		PD		2	4.5	7.8
cycling @1.0A·cm^{-2}; 20s@loading, 5s@OCV	Slow cycle; high *J*	Ohmic	0.6	7.9	10.3	14.4
		PD		2.3	5.0	8.2
cycling @ 1.0 A·cm^{-2}; 2s@loading, 1s@OCV	Fast cycle; high *J*, wet air	Ohmic	3.0	20.1	31.5	39.5
		PD		9.2	18.9	23.1
Hold @ 1.0 A·cm^{-2}	Constant & high *J*, wet air	Ohmic	3.0	5.3	7.1	9.2
		PD		1.8	3.6	5.2
cycling @1.0A·cm^{-2}; 2s@loading, 1s@OCV	Fast cycle; high *J*, dry air	Ohmic	0	9.4	18.4	21.6
		PD		4.4	7.6	9.9
Hold @ 1.0 A·cm^{-2}	Constant & high *J*, dry air	Ohmic	0	1.1	2.9	3.9
		PD		1.1	1.4	1.4

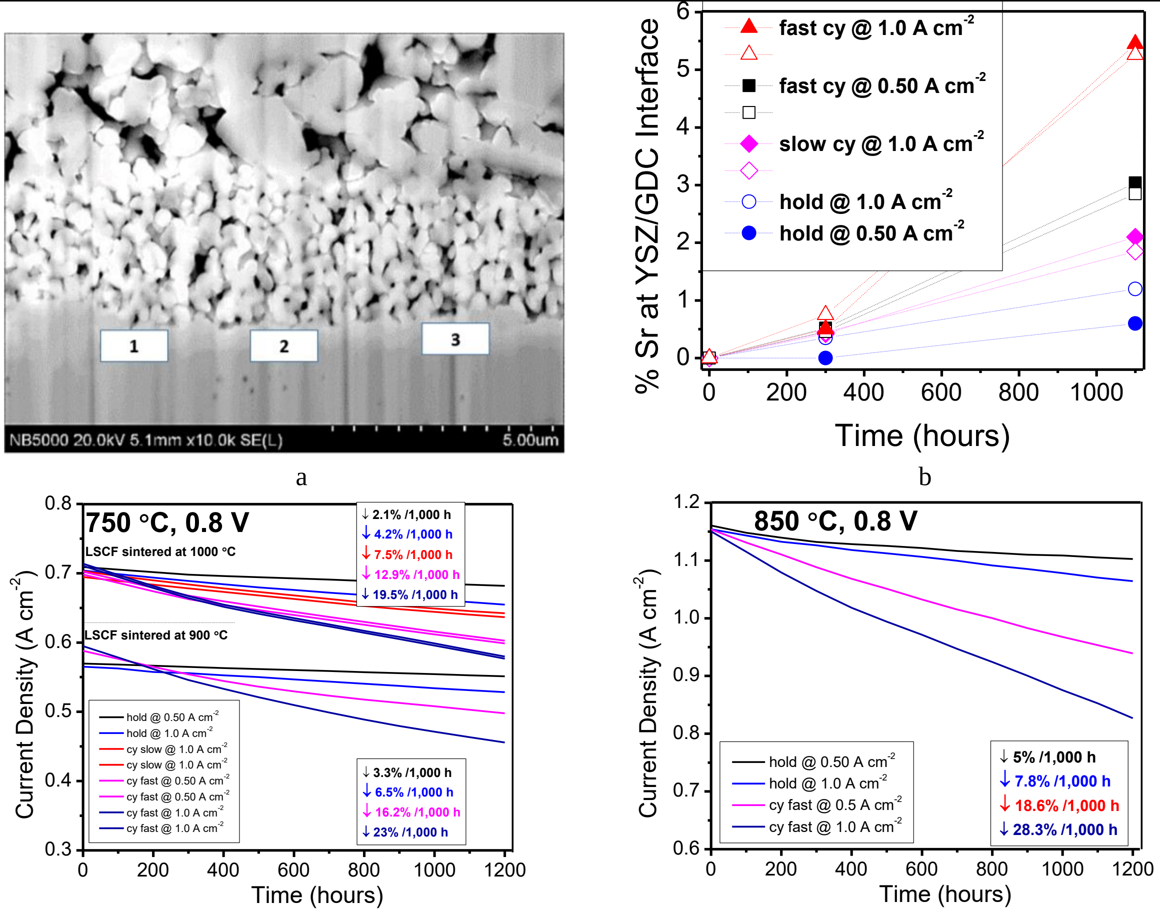

a

b

c

d

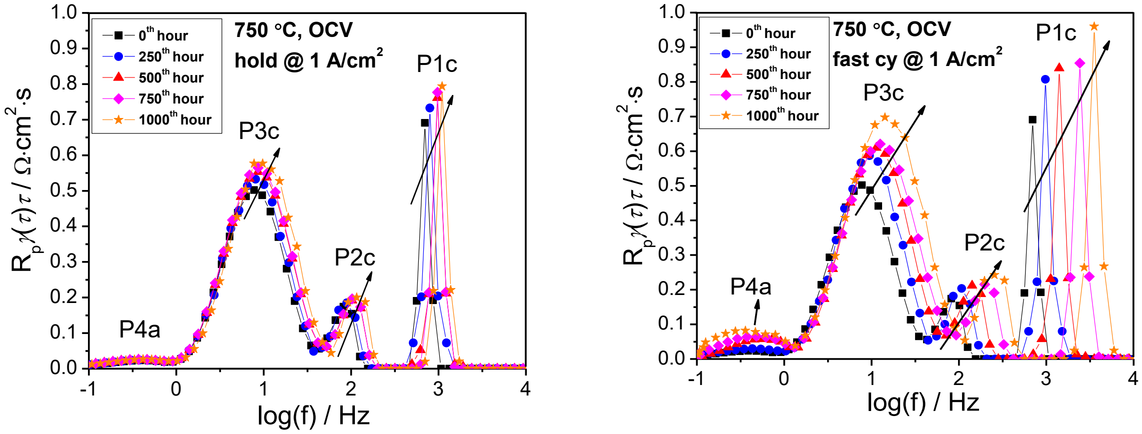

e f

Figure 23. (a) An cross-sectional image of LSCF-based cells for the analysis of GDC/YSZ interfaces (b) Sr concentration at the interfaces as a function of time under various operation conditions. (c) Cell performance upon cycling with LSCF sintered at 900 or 1080 °C. (d) Cyling effect at a higher operation temperature (850 °C). (e) and (f) are DRT analysis showing the evolution of ASR_{ohm} and ASR_p vs. time at 750 °C. Note the anode peaks (P4a) slightly changes upon cycling, while it remains constant and a low value at a constant current.

The GDC layer was used to inhibit interaction between LSCF and YSZ, which results in the formation of insulating $SrZrO_3$ or the diffusion of Zr into LSCF. Therefore, the observation of Sr at the interfaces between YSZ and GDC is a surprise. Furthermore, Sr concentration, shown in **Figures 23 (a)** and **(b)** at the interfaces is much higher in the cells under a faster cycling measurement (see more results in **Table I**). In addition, a higher current appears to result in a faster segregation, thus a higher increase in the ohmic loss. Segregation was not detected at the YSZ/GDC interfaces in the cell before operation. The ohmic loss continuously increases with time under fast cycles, as shown in **Figures 22** (e) and (f). When analyzing the presence of Sr, it is necessary to couple it with La/Co/Fe since the electron bean during EDS analysis may reach to the cathode. If both La and Sr are detected with a ratio close to 6/4, it suggests that this assumption is true, especially if Co and Fe are detected in a corresponding ratio, following the formula of the cathode. None of La/Co/Fe was observed at the YSZ/GDC interfaces. Multiple cells (typically 2-3) are needed to study the **reliability and reproducibility** of each cycling condition, as listed in **Table I**. The Sr segregation at the YSZ/GDC interfaces is closely correlated with the decrease in cell performance (**Table I** and **Figure 23**). It is clear that the measurements between 200- and 1,100-hour periods can be used to simulate the steady-state operation up to 2,000 and 10,000 hours. This means that the accelerated test protocols are valid. **Figure 23** (c) show the role of the sintering temperature on the cell performance upon cycling with LSCF being sintered at 900 or 1080 °C. Higher sintering temperature resulted in an improved performance and performance stability. **Figure 23** (d) shows the cycling effect at a higher operation temperature (850 °C), which leads to a more rapid degradation than that at 750 °C. **Figures 23** (e) and (f) are DRT analysis showing the evolution of ohmic resistance and electrode resistance as a function of time. P1c peaks (highest frequency) are assigned as the ohmic ASR, the area of which increases with time. P2c and P3c peaks are dominated by the electrode polarization resistance. P4a is negligible in this case. P4a does evolve with time during the cycling measurements, which can be used to develop accelerated test protocols. Electrode polarization is shown in **Figure 24a**. The change of polarization resistance is marginal, comparing with the increase in ohmic ASR, suggesting the electrode is still active during long term operation.

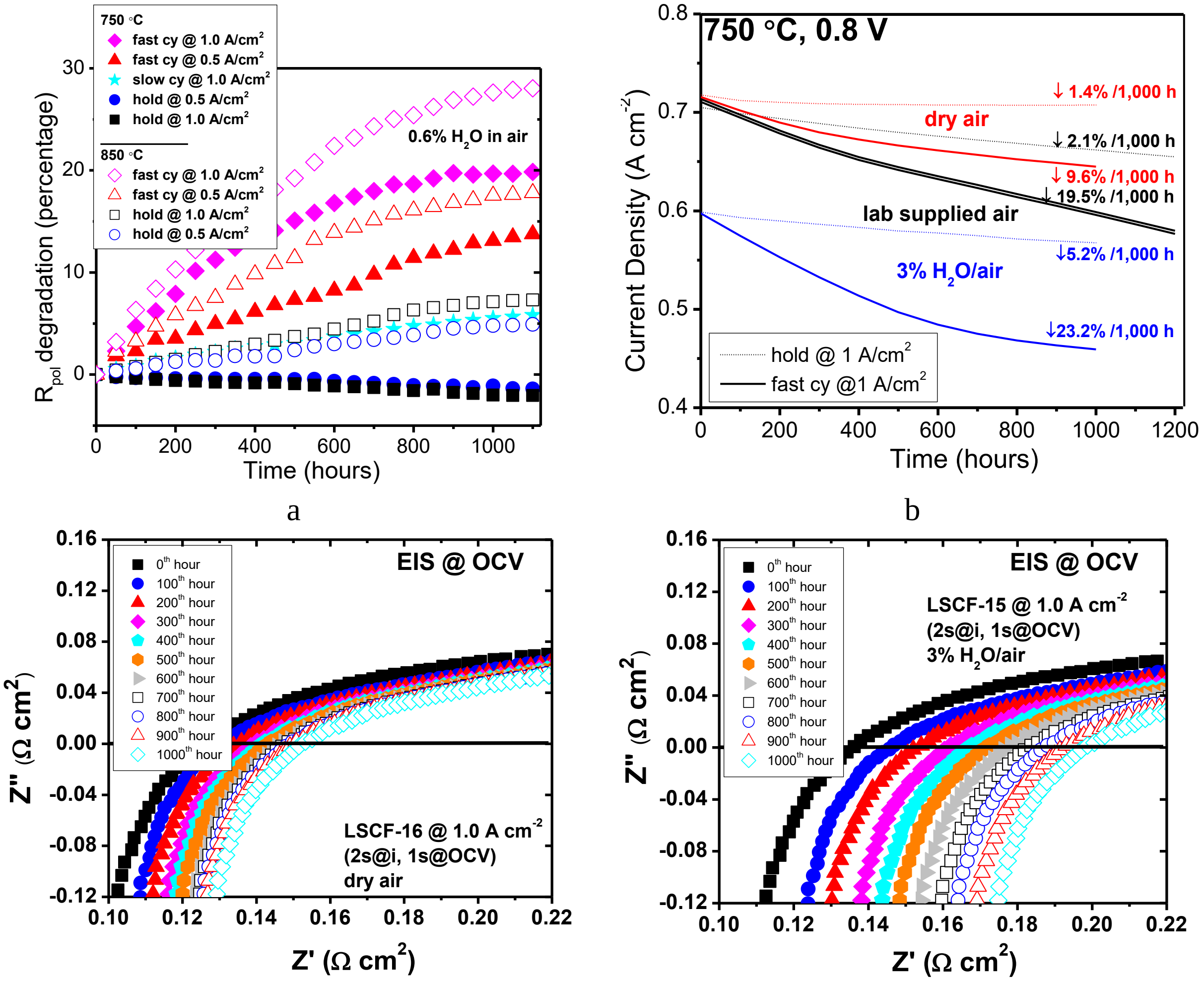

a

b

c

d

Figure 24. (a) Electrode polarization resistance, (b) cell performance, and EIS (c) and (d) as a function of time during cycling measurements with various moisture content.

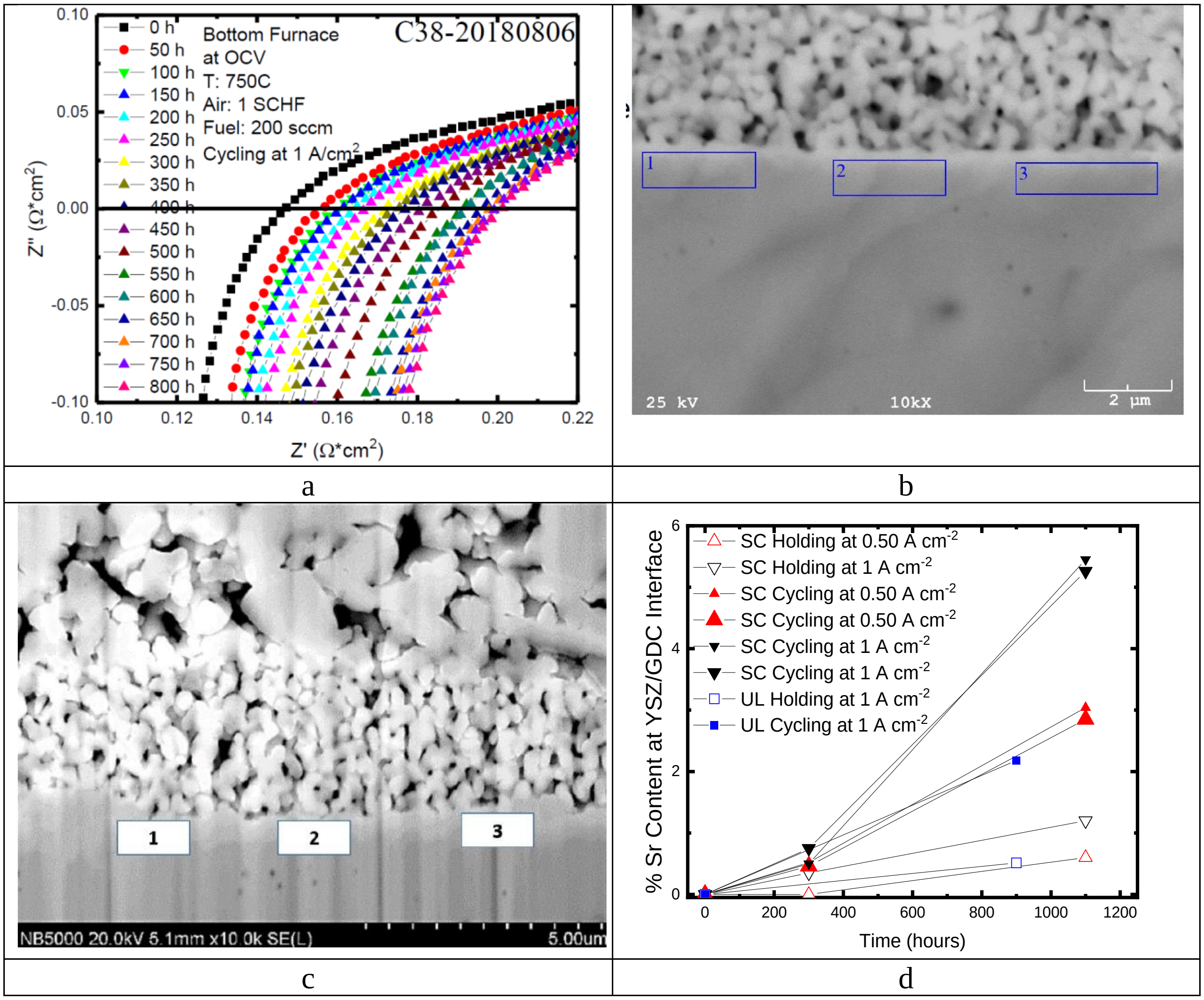

a

b

c

d

Figure 25. (a) EIS as a function of time under ATPs, showing reproducibility of this method. (b) and (c) SEM/EDS analysis of the specimens. (d) Sr content at the interface between YSZ and GDC barrier layer.

B.3.3.3. Large Area SOFC and Effect of Cr on ATP

Figure 26 (a) to (d) show the cell with a large area (16 cm^2) and cycling at 0.3 A/cm^2. Both ohmic and electrode polarizations increase with cycling conditions. While the cycling current density is lower than these shown in **Table 1**. The results shown in **Figures 26a to d** are encouraging to apply ATPs in cells with a large area. The possibility to utilize Sr was explored, which is generated through demixing during ATPs to catch volatile Cr-species, as shown in **Figures 27 a** and **b**. While the initial experimental results show the possiblity, more systematical work is needed to investigate this hypothesis.

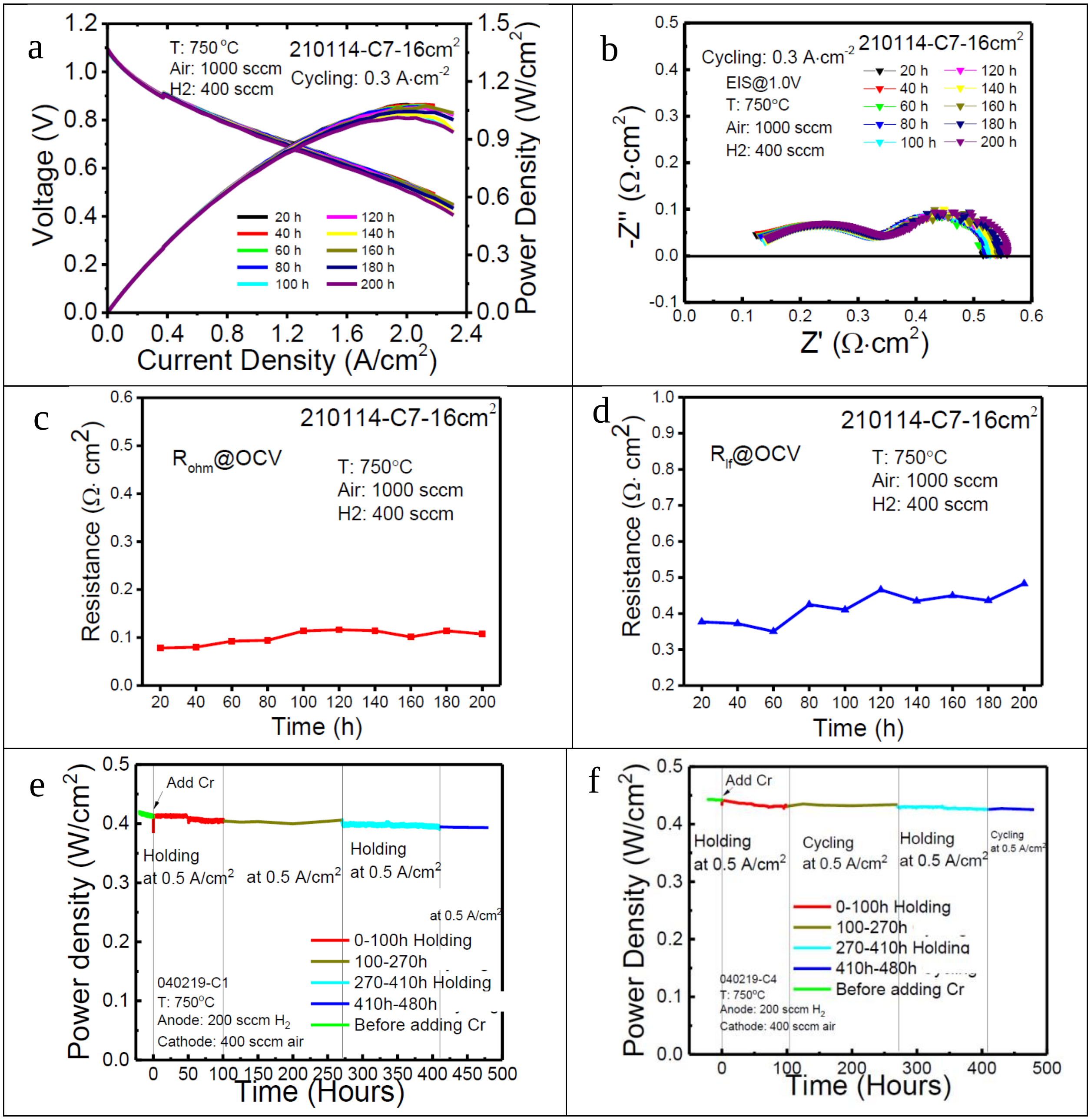

Figure 27. (a) I-V plots of the cell after cycling at 0.3 A/cm^2 (cell area; 16 cm^2). (b) EIS spectra at various cycling time. (c) ohmic polarization vs. time. (d) electrode polarization vs. time. (e) Power density of the LSCF-based cell with steady-state operation. Cr-source was added at 0th hour, which led to the decrease of power density. (f). After Cr-source was added. The cell was cycling at 0.5 A/cm^2, showing the possibility to maintain the current density and power density at a stable value. More studies are needed to test the hypothesis of Cr-getter by using demixed Sr species.

B.3.3.4. Anode Microstructural Evolution under Various Operation Modes

The properties of anode support and its effect on cell performance were investigated under various operation regions, e.g. activation, ohmic, and concentration polarization regions. The results show that when the cell is operating in the concentration polarization region, the performance degradation is much higher than in the other two regions. SEM and EDS were used to analyze the microstructure and its element distribution, as shown in **Figure 28**. The results showed that the grains in origin structure before reduction were uniform and consistent without having large-sized agglomerates in anode. When the cell was operated in the activation polarization region, the microstructure in anode kept uniform and having no Ni agglomeration, shown in **Figure 28a**). As the cell was operated under the concentration polarization region (**Figure 28b**), large-sized agglomeration could be found in the anode. The EDS indicated that the agglomerated particles were mainly Ni. In ohmic polarization region, there are few agglomerates in the anode. The change of microstructure in the anode is consistent with the cell performance degradation, which is ~20 times larger than when the cell operates in the concentration polarization than that under ohmic polarization region.

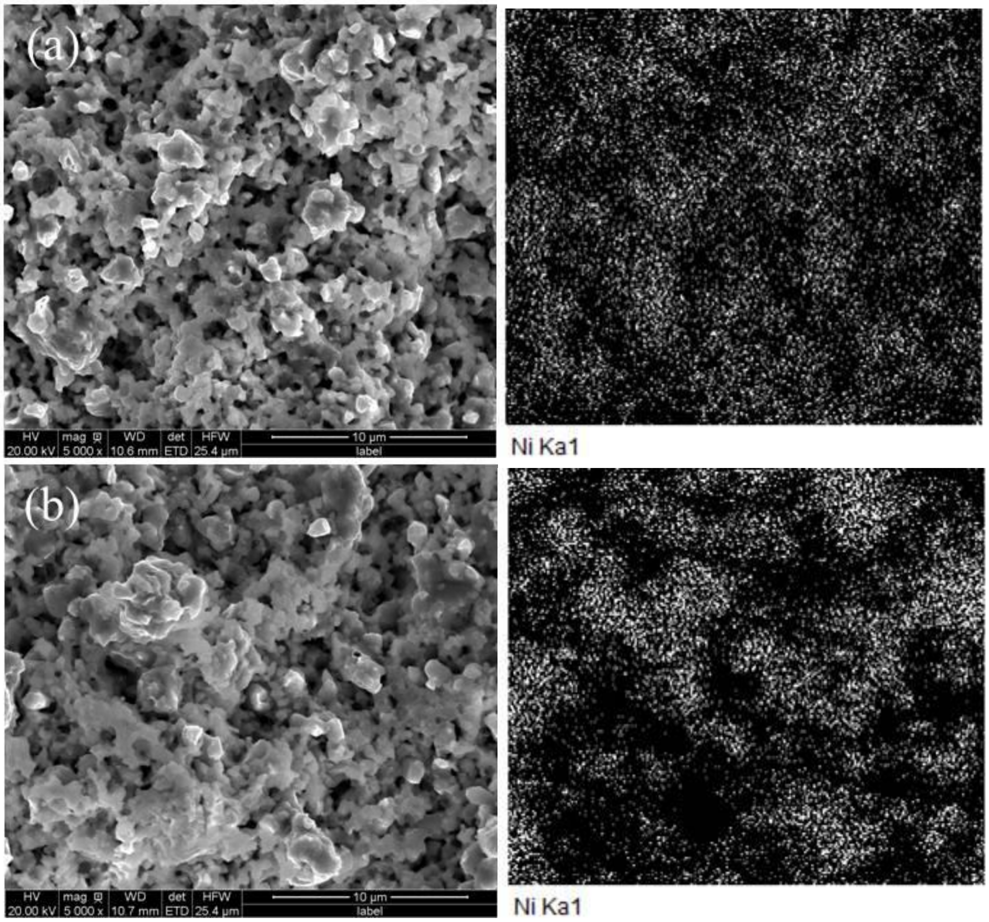

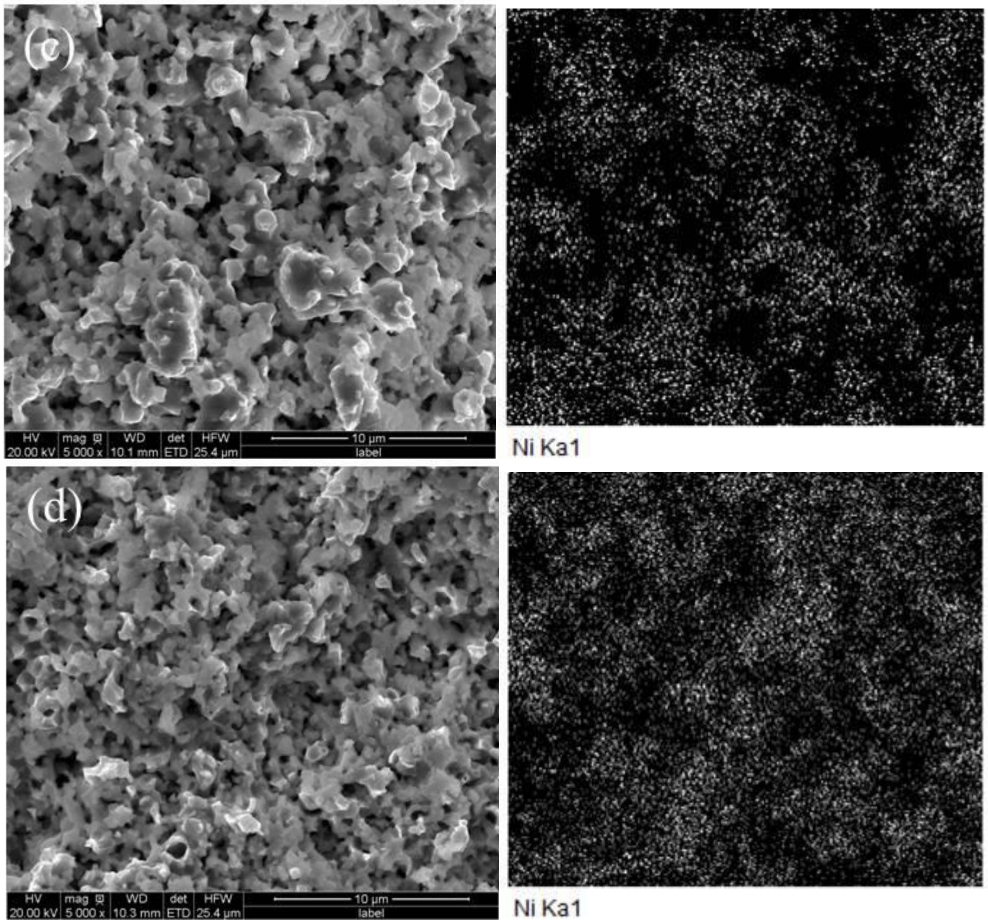

Figure 28. Images of anode structure and its EDS under various polarization intervals: (a) active polarization; (b) concentration polarization; (c) ohmic polarization; (d)un-reduction.

B.4 Summary

A general accelerated test profile was developed by cycling an SOFC from open circuit (current = 0) to a predetermined operating current density to accelerate the local redox environment. The cell operating current densities during the accelerated test were between 0.25 and 1 A/cm^2. Two cycle frequencies were used: fast cycle was done by holding the cell at an operating current for 2 seconds and then at the open circuit for 1-second; while the slow cycle was holding for 20 seconds at an operating current and 5 seconds at open circuit condition.

For nickelate based cathodes, cells operated at a constant current density were compared to cells undergoing ATPs, which are composed of intermittent current injection to the cell. The performance degradation was accelerated by 16× in PNNO electrodes when compared to standard cell operation. DRT analysis showed a clear increase in cathode ASR, which has been linked to phase transformation. ATPs demonstrated 67% increase in phase transformation when compared to standard electrochemical operation in PNNO cells. Furthermore, highly stable NNO electrodes were tested with ATPs and underwent surprising sixfold increase in performance degradation (0.37%/1,000 hours) after 1,100 hour operation at 750 °C and 0.25 A/cm^2. The parent NNO phase also underwent phase transformation in multiple cells, with formation of Nd_2O_3.

For LSCF-based cathodes, the following parameters were studied: current density, operation temperature, moist level, sintering temperature, cycling current, cycling frequency, operation time, and cathode composition. During the steady-state operation, a higher operation current (1 A/cm^2) results in a slightly larger increase in the ohmic resistance than the cell operated at 0.5 A/cm^2. An accelerated increase in ohmic resistance was observed during the use of ATPs. The acceleration effect is more dominant with a higher cycling current, faster cycling frequency, a higher operation temperature (e.g. 850 ^oC), and a greater moist level. When the cells were tested under ATPs at the fast cycle at 850^{o}C with the presence of 3% H_2O in the air stream, it was observed that the ohmic resistance increase was accelerated by nearly 10×, suggesting the feasibility of using this protocol for acceleration test. The accelerated increase in ohmic resistance was linked with the increase of Sr concentration at the YSZ/doped ceria interfaces, which was also observed in cells operated under stead-state conditions.

Presence of Cr. A Cr-source was added in LSCF-based cells to evaluate the role of Cr-volatile species on the effectiveness of ATPs. During steady-state operation, the cell performance decreases after the addition of Cr source due to the poisoning effect of volatile Cr species in the air stream. When ATP was adopted, however, the current density and power density were rather stable, suggesting the possibility to use the segregated Sr from ATPs to capture volatile Cr species. More studies are needed to test the hypothesis of Cr-getter by using demixed Sr species.

For the Ni-YSZ anode, the operation conditions were found to play a key role on the microstructural evolution. The results show that when the cell is operating in the concentration polarization region, the performance degradation is much higher than in the other two regions (activation and ohmic regions). This degradation is likely resulted from the microstructural changes in cells operated under the concentration polarization region, when large-sized Ni-agglomerations were observed in the anode.

Evidently the ATPs are a promising method in SOFC electrode evaluation, which take into advantage the role of electrochemical potential on phase transformation and structural changes in electrodes

C. Task 3. Pinpoint the Locations of Degradation and Investigate the Role of Barrier Layer on the Cathode Phase Stability

C.1 Introduction

Recent development of SOFCs able to operate at intermediate or low temperatures (<800° C)[12–17] helps circumvent this issue, thus prolonging the lifespan of the cell material and widening the pool of materials which can potentially be employed for cell construction. Capability of operating at lower temperatures can ultimately make SOFCs more cost-effective. Much effort has been made for materials development of the key cell components[15,16,18–21] – i.e., electrolyte, cathode, and anode, to improve the cell performance. In particular, recent studies have been aimed at identifying and minimizing the major loss processes occurring during cell operation and limiting its performance. Most of the recent research efforts tend to evaluate the performance of a specific cell component, such as the cathode or the anode, by optimizing the electrode material composition and its intrinsic properties (e.g. thickness, porosity and conductivity) or experimental conditions (e.g. operating temperature), while keeping the remaining critical cell components unvaried. In this approach, improvement of cell performance is generally attributed exclusively to optimization in the specific property of the electrode material or experimental parameter. However, the controlled processes, which include gas diffusion, ionic transport and charge transfer reactions, may exhibit deviation from expected behavior due to unavoidable experimental errors. Separation of the contributions of such processes occurring in different cell components is paramount to optimize cell performance since deep insights into the mechanisms which govern its operation are typically needed for this purpose.

Regarding the degradation and phase stability of cathode, much needs to be done from a theoretical point of view to elucidate the origin of stability by conducting *ab initio* calculations. For instance, it is known that PNO is unstable and decomposes to form $Pr_4Ni_3O_{10}$, Pr_6O_{10} at elevated temperatures[18], which is of concern for SOFC operation. Dogdibegovic et al. studied the effects of $(Pr_{1-x}Nd_x)_2NiO_4$ (PNNO)[5, 16, 18-19] and the buffer layer[20], e.g., Gd doped CeO_2 (GDC), on the long-term stability of PNO. They found that a rapid degradation rate of 3.5% occurs for PNO cells within 150 hours. After 1000 hours at 0.8 V and 750°C, the performance degradation rate of PNO reaches 6.4%, while the performance of $(Pr_{0.75}Nd_{0.25})_2NiO_4$ (PNNO7525), $(Pr_{0.5}Nd_{0.5})_2NiO_4$ (PNNO5050), and $(Pr_{0.25}Nd_{0.75})_2NiO_4$ (PNNO2575) remained stable, with minor degradation rates of 0.56%, 0.25%, and 0.13%, respectively. Upon increasing Nd content, the diffusion rate of Pr into bulk GDC decreases. Consequently, the phase transition and reaction with the GDC buffer layer are suppressed. For the buffer layer, GDC promotes the decomposition of PNO. When the GDC is the buffer layer, results from energy-dispersive X-ray spectroscopy (EDS) indicates that Pr diffuses into the GDC layer, wherein the PNO contains Pr vacancies in the bulk. To date, it is unclear when the Pr vacancy occurs in PNO and the role of the interstitial O ions and cation vacancies on the activity and stability of PNO-based cathodes.

The aims of this task include (1) to systematically investigate the role of gas composition in both anode and cathode on the feasibility of using EIS and DRT to deconvolute the cell impedance, (2) to perform Density Functional Theory (DFT) studies to investigate (i) the effect of Pr vacancies on oxygen-ion transport and performance of PNO, (ii) the origin of the enhanced stability of PNNO, and (iii) to devise other effective Ln^{3+} dopants that improve the stability of PNO, and (3) to perform experiments on the use of dense barrier to investigate the cathode stability (see the section C.3.3.3. Effect of dense GDC barrier layer on the applicability of ATPs).

C.2 Experimental Method

C.2.1 Structural and Post Analysis

XRD patterns were obtained simultaneously on all cells before and after the cell operation without any manipulations on the cathode and current collector surfaces. External Al sample holder, Ni/YSZ/GDC ceramic substrates (or YSZ/GDC substrates for symmetric cells), and single phase PNNO and PrO_x powders were used as external standards to ensure a proper peak positioning and normalized flux. Surface and cross sectional images on cells were obtained using the Tescan Vega-3 (Brno, Czech Republic) SEM with EDS capability. Focused ion beam (FIB) and EDS analysis was performed on nano DUE'T double beam NB5000 microscope (Hitachi, NY, 10591). TEM images on operated electrodes were obtained with JEOL 2010F (JEOL Inc., MA, 01960).

C.2.2 DFT Calculation of Defects in $(Pr,Ln)_2NiO_4$

Spin-polarized DFT calculations were undertaken using the VASP[21] computational package. The projector augmented wave (PAW) method[22-23] and the Perdew–Burke–Ernzerhof (PBE) [24] functional, were used to describe the electron-ion and exchange-correlation interactions. A cutoff energy (E_{cut}) of 550 eV was used in order to expand the wavefunction. For Ni containing oxides, the generalized gradient approximation (GGA)+U method was used, wherein U = 6.3 eV[25]. The total energy convergence criterion was set to $< 10^{-6}$ eV and the force convergence criterion to < 0.01 eV $Å^{-1}$. A Monkforst-Pack[26] 4×4× 1, 2×1×1 k-point grid was used for the unit cell of Pr_2NiO_4, while a supercell of 2×3×1 I4/mmm was used for $Pr_{24}Ni_{12}O_{48}$. CI-NEB[27] was used in order to calculated the oxygen, Pr and Nd diffusion barriers. Here, the Bader charge analysis[28] was used to evaluate the oxidation states of the elements. The trivalent La, Nd, Pm, Sm, Gd, Tb, Dy, and Ho were described by treating localized 4f electrons as frozen core electrons. This method has been successfully used to predict lattice parameters, defect formations, migration energies, ionic conductivity and superconductivity parameters. [29-32]

C.3 Results and Discussion

C.3.1 Call Attention to the Use of DRT to Pinpoint Degradation of SOFCs

C.3.1.1 Theoretical Analysis on the EIS and DRT Methods

Electrochemical impedance spectroscopy (EIS) is a widely used in-situ technique for SOFCs performance evaluation.[17,22,23] A small AC perturbation is applied to the cell and the impedance of the cell versus AC frequency is recorded based on voltage respondence. The impedance spectrum provides abundant information about the reaction kinetics and transport process. The full cell impedance is consistent of three parts, the ohmic resistance (R_o), the charge transfer reaction impedances of cathode (Z_c) and anode (Z_a).

$$Z_{cell}(\omega) = Z_c(\omega) + R_o + Z_a(\omega) \quad [1]$$

The high frequency intercept of the real axis in the Nyquist plot is ohmic resistance, R_o, which is considered contributed from the resistance of ionic transport in the electrolyte and independent of AC frequencies. The rest impedance provides useful information on different dynamic process in the electrodes.

Traditional EIS analysis is performed *via* the complex nonlinear least-squares fitting based on a provided equivalent circuit model (ECM). The fitting result highly depends on the quality of the ECM used.[24] The downside of this approach is that the complete ECM requires a deep understanding and prior knowledge of the electrochemical system (and processes occurring within it) which are not available in many practical cases. By contrast, the distribution of relaxation time (DRT) approach represents a valid alternative which allows to investigate the system without any initial assumptions. [25] This approach can be used to directly convert the impedance spectra from the frequency domain to the relaxation time domain, by means of Eq.[2]

$$Z_{cell}(\omega) = R_o + \int_{-\infty}^{+\infty} \frac{\gamma}{1+j\omega\tau} d(ln\tau) \quad [2]$$

where γ is distribution function of relaxation time, ω is the angular frequency and τ is the relaxation time. The transformed DRT spectrum has better resolution than the EIS, in that, it provides deeper insights into the nature of various processes which govern cell operation and aid unravelling the ways in which they depend on the operating conditions or materials characteristics. [26,27] For each relaxation time distribution appearing in the DRT spectra, the integrated area under the peak correspond to the contribution to polarization resistance arising from the associated process. Schichlein et *al*. first applied this concept in the DRT application on the deconvolution of SOFC impedance spectra. [28] Since then DRT have been extensively used for identifying the ECM of the electrochemical system, leading to a detailed mechanistic interpretation of EIS results.[29] In recent years, DRT have been successfully used to investigate and advance the study and application of new materials for proton conductor fuel cells,[30] oxygen-ion conducting solid oxide fuel cells (O-SOFC), and solid oxide electrolytic cells (SOEC), by enabling identification of crucial performance-determining processes, *e.g*. degradation mechanisms, Cr poisoning[31,32] and Sr segregation.[33,34]

For the charge transfer reaction that follows a Butler-Volmer type kinetics, at the cathode side, the current density, i, can be expressed as:

$$i = i_{0,c} exp(b_{OER}\eta_c) - i_{0,c}\left(\frac{C_{O_2}}{C_{O_{2},0}}\right)^{l} \exp(-b_{ORR}\eta_c) + C_c \frac{d\eta_c}{dt} \quad [3]$$

where $i_{0,c}$ is the exchange current density of the cathode, l is the order of reaction respective to oxygen, C_{O_2} is the oxygen concentration at the triple phase boundary, $C_{O_{2},0}$ is the reference concentration, η_c is the overpotential of the electrode, b_{OER} and b_{ORR} are Tafel slope of OER and ORR respectively, and C_c is the area specific capacitance. By introducing a sinus wave perturbation, $\tilde{\imath} = \delta i \exp(j\omega t)$, to the system:

$$\tilde{\imath} = i_{0,c}\left[b_{OER}\exp(b_{OER}\eta_{OE}) + b_{ORR}\left(\frac{C_{O_2}}{C_{O_2,0}}\right)^{l}\exp(-b_{ORR}\eta_c)\right]\widetilde{\eta_c} - \frac{l i_{0,c}}{C_{O_2,0}}\left(\frac{C_{O_2}}{C_{O_2,0}}\right)^{l-1}\exp(-b_{ORR}\eta_c)\,\widetilde{C_{O_2}} + j\omega C_c\widetilde{\eta_c} \qquad [4]$$

where ω is the angular frequency of the sinus wave. The OER (R_{OER}), ORR (R_{ORR}) and total charge transfer resistance ($R_{ct,c}$) are defined in the cathode:

$$R_{OER} = \left[i_{0,c}b_{OER}\exp(b_{OER}\eta_{OE})\right]^{-1} \qquad [5]$$

$$R_{ORR} = \left[i_{0,c}b_{OER}\exp(b_{OER}\eta_{OE})\right]^{-1} \qquad [6]$$

$$R_{ct,c} = (R_{OER}^{-1} + R_{ORR}^{-1})^{-1} \qquad [7]$$

On can easily obtain

$$Z_c(\omega) = \frac{\widetilde{\eta_c}}{\tilde{\imath}} = \frac{\left[R_{ct,c} + \frac{R_{ct,c}\frac{l i_{0,c}}{C_{O_2,0}}\left(\frac{C_{O_2}}{C_{O_2,0}}\right)^{l-1}\exp(-b_{ORR}\eta_c)\,\widetilde{C_{O_2}}}{\tilde{\imath}}\right]}{1 + j\omega C_c R_{ct,c}} = \frac{R_{ct,c} + Z_{D,O_2}}{1 + j\omega C_c R_{ct,c}} \qquad [8]$$

where $Z_{D,O_2}$is the oxygen diffusion impedance

$$Z_{D,O_2} = R_{ct,c}\frac{l i_{0,c}}{4FD_{O_2}C_{O_2,0}}\left(\frac{C_{O_2}}{C_{O_2,0}}\right)^{l-1}\exp(-b_{ORR}\eta_{OE})\frac{-\widetilde{C_{O_2}}}{\frac{d\widetilde{C_{O_2}}}{dy}|_{TPB}} \qquad [9]$$

For the anode one can also write:

$$Z_a(\omega) = \frac{R_{ct,a} + Z_{D,H_2O} + Z_{D,H_2}}{1 + j\omega C_a R_{ct,a}} \qquad [10]$$

The total impedance consists of basically six components including ohmic resistance, charge transfer reactions in the cathode, oxygen diffusion, charge transfer reactions in the anode, steam diffusion and hydrogen diffusion.

$$Z_{cell}(\omega) = R_o + \frac{R_{ct,c} + Z_{D,O_2}}{1 + j\omega C_c R_{ct,c}} + \frac{R_{ct,a} + Z_{D,H_2O} + Z_{D,H_2}}{1 + j\omega C_a R_{ct,c}} \qquad [11]$$

The ohmic resistance can be separated from high frequency intercept. The other five components do have an imaginary component and each of them has a specific distribution of relaxation time. As a result, if the relaxation time distribution for two components is the same, these two components may not be differentiated from this analysis.

C.3.1.2 The Effect of Anode Gas Composition on EIS/DRT Analysis

The DC current-voltage (IV) and AC electrochemical impedance measurements were acquired to evaluate the cell performance and eventual loss processes, that are predominantly related to diffusion processes that may limit the reaction at the electrode-electrolyte interface (triple-phase boundary), charge-transfer processes at the electrode surface and thermal stability. During the various measurements, the operational temperature was maintained constant at 750 ^{o}C while the percentage fraction of H_2 in the fuel mixture and/or the identity of carrier gas at the anode were varied. Firstly, a series of IV curves were measured to evaluate the overall loss processes that occur during cell operation. **Figure 29a** displays the returned set of four IV curves acquired while tuning the percentage fraction of H_2 in the H_2/N_2 fuel mixture at the anode from 20% - 97%. As illustrated in this figure, the gradient becomes progressively steeper across the series of measurements, implying an increase in the resistance as a function of decreasing partial pressure of H_2. This observation is particularly evident at the high current density limit. These results indicate a reduction in the cell performance as a function of the depletion of H_2 at the triple phase boundary, which may imply a performance limiting factor for the operation of the SOFC, particularly at critically low concentrations of H_2 (e.g., at 20% H_2).

In addition to DC measurements, AC electrochemical impedance spectra (EIS) were also recorded at the same temperature and percentage fractions of H_2. **Figures 29b** and **c** display the EIS acquired at open-circuit voltage (OCV) conditions (~1.1 V) and 0.5 A cm^{-2} (~0.9 – 0.7 V). The results of the measurements are reported in the form of Nyquist plots where the frequency-dependent real (Z') and imaginary (-Z'') parts of the impedance are plotted in the x and y axis, respectively.

The EIS curves in **Figure 29b** feature *at least* two distinct but overlapping arcs. The most prominent arc is observed at low frequencies, while the second feature arises at high frequencies and intercepts the real impendence axis Z' at ~ 0.180 Ω cm^{2}. Upon closer inspection of the curves, it is noted that the magnitude and profile of the traces are markedly dependent on the partial pressure of H_2 ($p(H_2)$). Indeed, upon increasing $p(H_2)$, the low frequency arc shifts to lower Z' values and decreases in amplitude. In addition, the Z' intercept, which represents the ohmic resistance, consistently shifts to lower values. Therefore, it can be deduced that, under a set of operating conditions, higher $p(H_2)$ leads to lower total (ohmic and polarization) resistance and, as such, to an overall improvement in the cell performance.

These same trends are also noted in **Figure 29c** wherein the tuning $p(H_2)$ leads to more pronounced changes in the profile and magnitudes of the arcs, thus implying that the total resistance is more drastically affected by the overall composition of the gas fuel mixture at lower loading voltages. Both IV and EIS results were obtained by tuning the amount of reactant H_2 at the anode while maintaining the cathode at the same conditions through the various measurements. It can therefore be implied that all changes in cell performance may be, to *first approximation*, attributed to changes in operating conditions at the anode.

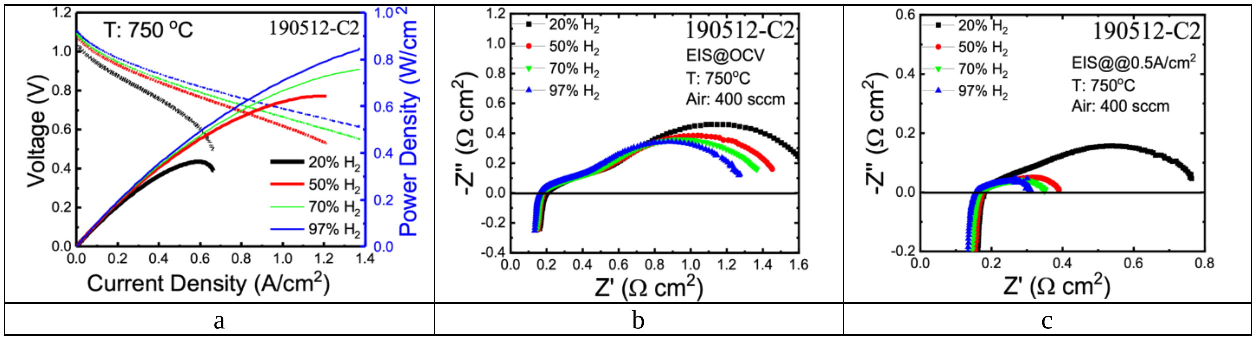

a b c

Figure 29: (a) IV curve and power density plot for the Ni-based anode at various H_2 in N_2 carrier gas (3% humidity), *i.e.* 97% H_2 (blue), 70% H_2 (green), 50% H_2 (red) and 20% H_2 (black). The curves were recorded at 750° C. A steady decline in the cell performance is observed as the partial pressure of H_2 in fuel gas mixture is decreased. (b) EIS@OCV, and (c) EIS@0.5A/cm^2 under various anode gas compositions (20% H_2, 50% H_2, 70% H_2 and 97% H_2, balanced by 3% H_2O and N_2). The ESI spectra exhibit a marked dependence on the composition of the humidified H_2/N_2 fuel mixture.

The combination of IV and EIS measurements offers valuable, but rather generic insights into the loss processes, which may limit cell performance. However, the intrinsic limitation of such techniques is their inability to provide process-specific information which might be useful to understand performance-limiting factors and optimize cell design and operation. Specifically, EIS measurements do not typically offer insights into the kinetics, mechanism, or nature for any loss processes, since overlapping or even individual arcs may be result from a convolution of several signals arising from different processes. Under these circumstances, the use of DRT approach provides a viable way of disentangling such coupled processes.

To this end, the DRT spectra were acquired as a function of $p(H_2)$ at OCV and 0.5 A cm^{-2} (**Figures 30a** and **b**, respectively). Both sets of measurements exhibit at least five distinct, although in some cases overlapping, Gaussian shape distributions (P1 – P5 in order of increasing relaxation times), which can be attributed to various physical and chemical processes, namely gas diffusion, charge transfer and electrochemical reactions that occur during cell operation and contribute to the overall polarization resistance. Amongst the five peaks, P1 and P5 are better resolved *cf.* the other peaks, with the latter dominating the DRT spectra at low $p(H_2)$. In order to better assess the dependence of the polarization resistance on the $p(H_2)$, quantitative analysis is performed by integrating the area under each peak as described in the experimental methodology, thus allowing to obtain the contribution of each peak (i.e. process) at various concentrations of H_2. The analysis is displayed in the bar charts in **Figure 30c** and **d**, which report the results acquired at OCV and 0.5 A cm^{-2}, respectively. These figures are coupled with **Table 2**, which reports the numerical values of the polarization resistance estimated through the analysis.

As also noticed from **Figure 30a**, P5 provides the largest contribution to the overall polarization resistance, especially at low $p(H_2)$, when compared to P1 – P4. The polarization resistance associated with this peak at 20% H_2 is estimated as 0.756 Ω cm^2 (out of a total polarization resistance of 1.184 Ω cm^2) and remains the largest across the whole series of measurements performed at OCV when compared to those associated with P1 – P4. This contribution shows, however, a sharp decreases as the percentage fraction of H_2 in the fuel mixture increases from 20% to 50%, and subsequently to 70%. No substantial changes occur thereafter, suggesting that the concentration of H_2 no longer represents a limiting factor for the process associated with P5 in these concentration regimes. Quantitative analysis on P1 – P4 is more challenging due to the smaller areas subtended the distributions and overlap between different spectral features.

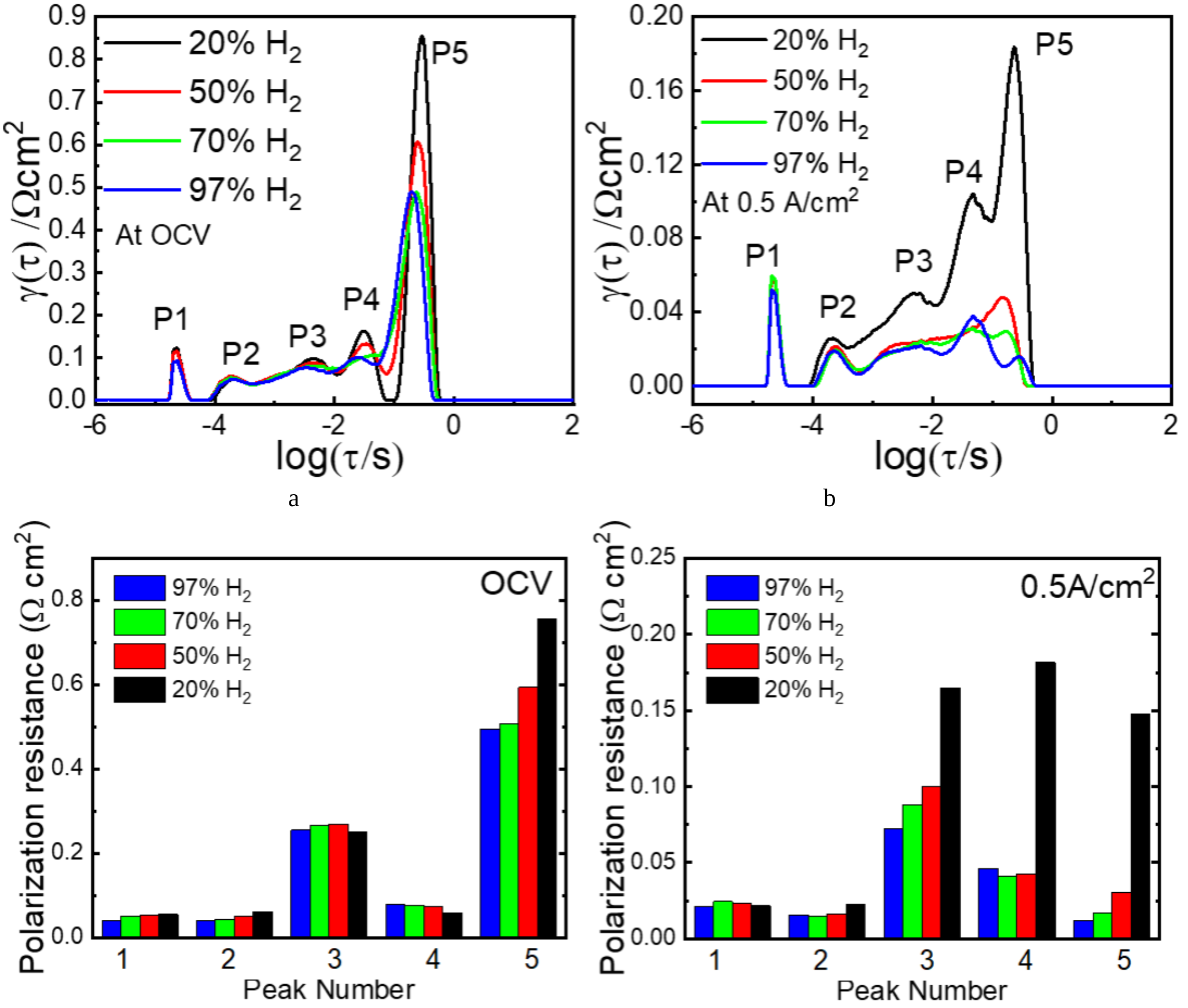

a b

c d

Figure 30: DRT analysis of the peaks *vs* H_2 concentration at (a) OCV and (b) 0.5 A cm^{-2}. Five peaks are observed in the spectra. The various gas mixtures contained, 20% H_2 (black line), 50% H_2 red line, 70% H_2 (green), 97% H_2 (blue). The polarization resistance of each peak as a function of the percentage fraction of H_2 in the DRT spectra is reported at (c) OCV and (d) 0.5 A cm^{-2}.

An attempt to estimate of the polarization resistance was however performed and the corresponding results are also reported in **Figure 30c** and **Table 2**. The analysis highlights less pronounced changes in the polarization resistance associated with other peaks *cf*. P5 and in some cases different trends. In particular, while P3 still appears to yield lower or comparable resistance at high *cf* low concentrations of H_2, P4 is estimated to be the only relaxation time distribution which is negatively affected by increasing $p(H_2)$, with its contribution to the polarization resistance increasing of about ~30% across the measurements from low to high partial pressure of the reactant, wherein the total polarization resistance is estimated to be 0.914 Ω cm^2. By comparison, as also noticeable in the corresponding EIS spectra, the results at 0.5 A cm^{-2} return lower overall polarization resistance (**Figure 30b** and **d** and **Table** 2), which are estimated to about 50% lower *cf*. OCV conditions. While P5 seems to dominate the DRT spectra, the distributions of P2-P5 are considerably overlapped, making it challenging to deconvolute the individual contributions of each peak to the overall polarization resistance. The multi-Gaussian peak fitting returns comparable contributions of P3 – P5 at 20% H_2 fraction. A drastic decrease of the polarization resistance associated with three peaks (and P2 to some extent) is observed upon increasing $p(H_2)$, especially with reference to P5, wherein the associated resistance decline by a total of 80%. This observation in stark contrast with the results at OCV wherein this distribution is always dominating the DRT spectra. It is also to be noted that the P3 and P4 exhibit a different trend as a function of $p(H_2)$ when compared to the equivalent results obtained at OCV conditions.

Table 2: Polarization resistance (Ω cm^2) associated with different peaks (processes) observed in the DRT spectra at OCV and 0.5 A cm^{-2} as a function of varying H_2 concentration in the H_2/N_2 gas mixture.

	OCV				**0.5 A cm^{-2}**			
Peak #	97% H_2	70% H_2	50% H_2	20% H_2	97% H_2	70% H_2	50% H_2	20% H_2
1	0.042	0.051	0.053	0.055	0.021	0.025	0.022	0.022
2	0.042	0.045	0.050	0.062	0.016	0.014	0.017	0.022
3	0.255	0.266	0.270	0.251	0.073	0.088	0.100	0.165
4	0.080	0.078	0.074	0.060	0.046	0.041	0.043	0.182
5	0.496	0.508	0.594	0.756	0.012	0.017	0.030	0.147

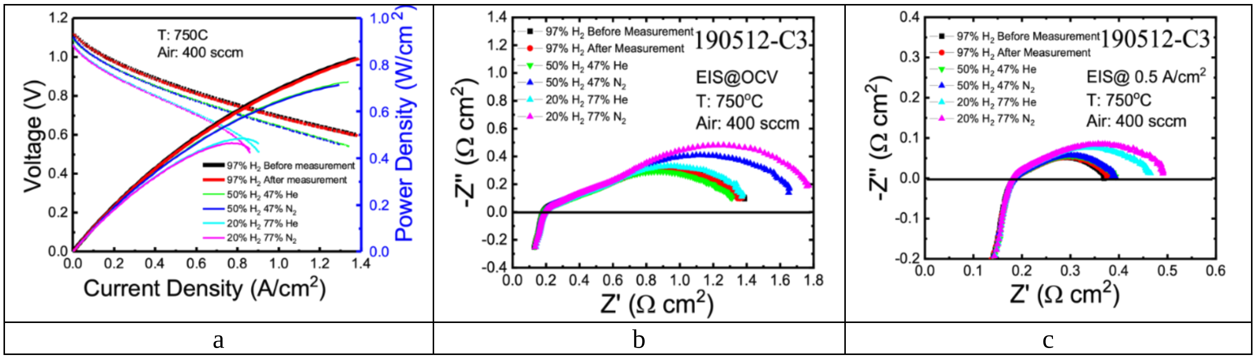

a b c

Figure 31. Balanced gas effect in anode, replace the N_2 in the anode with He. (a) IV, (b) EIS@OCV, and (c) EIS@0.5A cm^{-2} *vs* anode gas composition.

For better understand the nature of the processes associated with the DRT spectral distributions, measurements were carried out changing the carrier gases from N_2 to He. **Figures 31a** to **c** show the IV and EIS measurements acquired for the two gases at two different $p(H_2)$, namely 50% and 20%. While the IV curves show no substantial difference between the two gases, the low frequency arc in the EIS spectra show some dependence, more evidently at OCV conditions (**Figure 31b**), wherein the use of He yields overall lower polarization resistance. By contrast at 0.5 A cm^{-2}, the concentration of H_2 appears the dominant factor affecting the polarization resistance. The corresponding DRT spectra are reported in **Figures 32a** and **b** with associated analysis in panel (c) and (d) and **Table** 3. The DRT spectra recorded for this assembly at OCV and 20% H_2 in N_2 show that P4 and P5 are coupled and merged in single Gaussian-like distribution, but separation of the peaks becomes more visible at higher $p(H_2)$. The results suggest that the polarization resistance is considerably reduced (~20%) when He is used as balanced gas, especially at higher concentration of H_2, with P3 – P5 being the most visibly affected. Furthermore, the results at 0.5 A cm^{-2} suggest that, although the concentration of H_2 appears to have a determining effect on the polarization resistance, the use of H_2/He fuel mixture contributes to lower the contribution of P5 to the overall resistance to larger extent when compared to the other peaks (and *cf*. H_2/N_2). In the next section, more discussion will be presented on such contributions in the context of variation in the operating conditions at the cathode, to assess the contribution of various processes as a function of tuning concentration of O_2 and nature of the balance gasses.

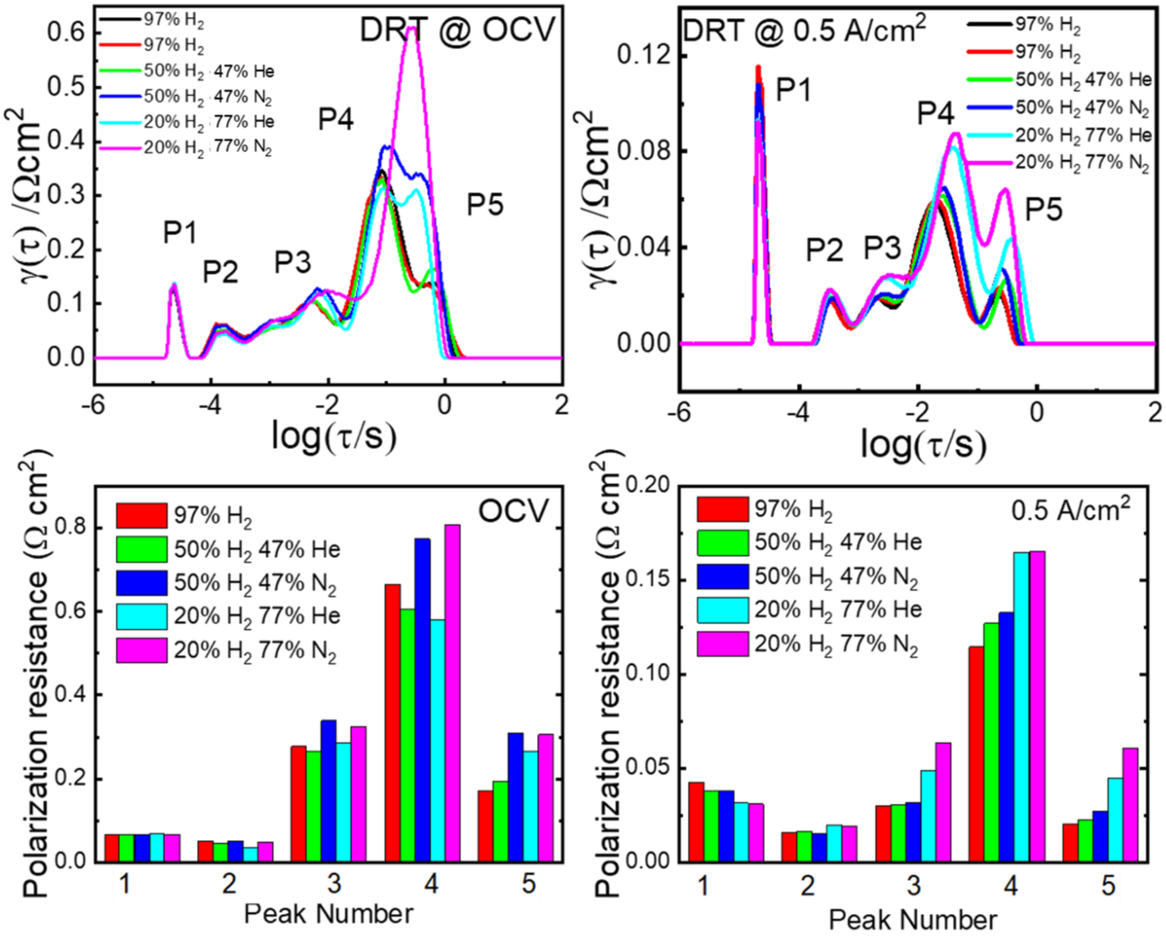

Figure 32. DRT analysis of EIS at (a) OCV and (b) 0.5A cm^{-2} with helium or nitrogen as balanced gas. The polarization resistance of each peak as a function of the percentage fraction of H_2 and nature of balanced gas (N_2 *vs* He) in the DRT spectra is reported at (c) OCV and (d) 0.5 A cm^{-2}.

Table 3: Polarization resistance (Ω cm^2) associated with different peaks (processes) observed in the DRT spectra at OCV and 0.5 A cm^{-2} as a function of varying H_2 concentration and the carrier gas (N_2 *cf*. He).

			OCV		
Peak #	97% H_2	50% H_2/He	50% H_2/N_2	20% H_2/He	20% H_2/N_2
1	0.065	0.067	0.065	0.069	0.067
2	0.051	0.045	0.052	0.036	0.048
3	0.278	0.266	0.338	0.285	0.324
4	0.664	0.606	0.774	0.581	0.808
5	0.172	0.194	0.310	0.266	0.306

0.5 A cm^{-2}					
Peak #	97% H_2	50% H_2/He	50% H_2/N_2	20% H_2/He	20% H_2/N_2
1	0.043	0.038	0.038	0.031	0.031
2	0.016	0.016	0.015	0.020	0.019
3	0.030	0.031	0.032	0.049	0.064
4	0.114	0.127	0.133	0.165	0.165
5	0.021	0.023	0.027	0.045	0.061

C.3.1.3 The Effect of Cathode Gas Composition on EIS/DRT Analysis

Analogous IV and EIS measurements were acquired to evaluate the contribution of the cathode to the cell performance (**Figure 33a** to **c**). Again, the operational temperature was maintained at 750° C and the percentage fraction of O_2 in N_2 was varied between 10% - 100%, while fixing the fuel composition at 97% H_2 (3% H_2O).

The IV traces in **Figure 33a** display *qualitatively* a similar trend to the analogous curved acquired for the anode, *i.e.* a steeper gradient of the curves corresponds to lower partial pressure of O_2 ($p(O_2)$) and thus lower performance, implying that the concentration of O_2 is a determining factor for optimal cell operation. As in the **Figures 30a** and **b**, the EIS spectra in **Figure 33** display multiple, convoluted arcs. The ohmic resistance in this series of measurements does not exhibit any substantial dependence on $p(O_2)$. However, a considerable variation in polarization resistance is observed while tuning the gas composition, with the lowest total resistance found, as expected, at 100% O_2 pressure. Again, the overall resistance is substantially decreased in the measurements acquired at 0.5 A cm^{-2}, as observed in **Figures 33a** and **b**.

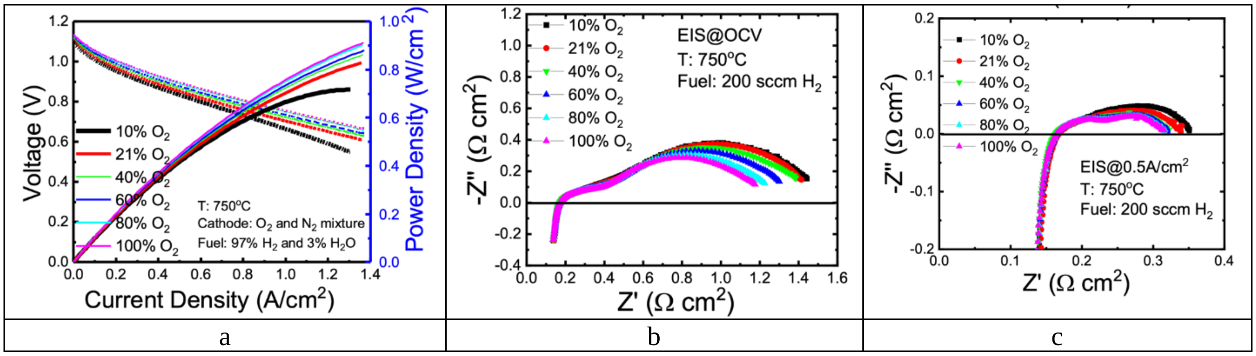

a b c

Figure 33. IV, EIS@OCV, and EIS@0.5A/cm2 vs cathode gas composition (10% O2, 21% O2, 60% O2 and 100% O2, balanced by N2)

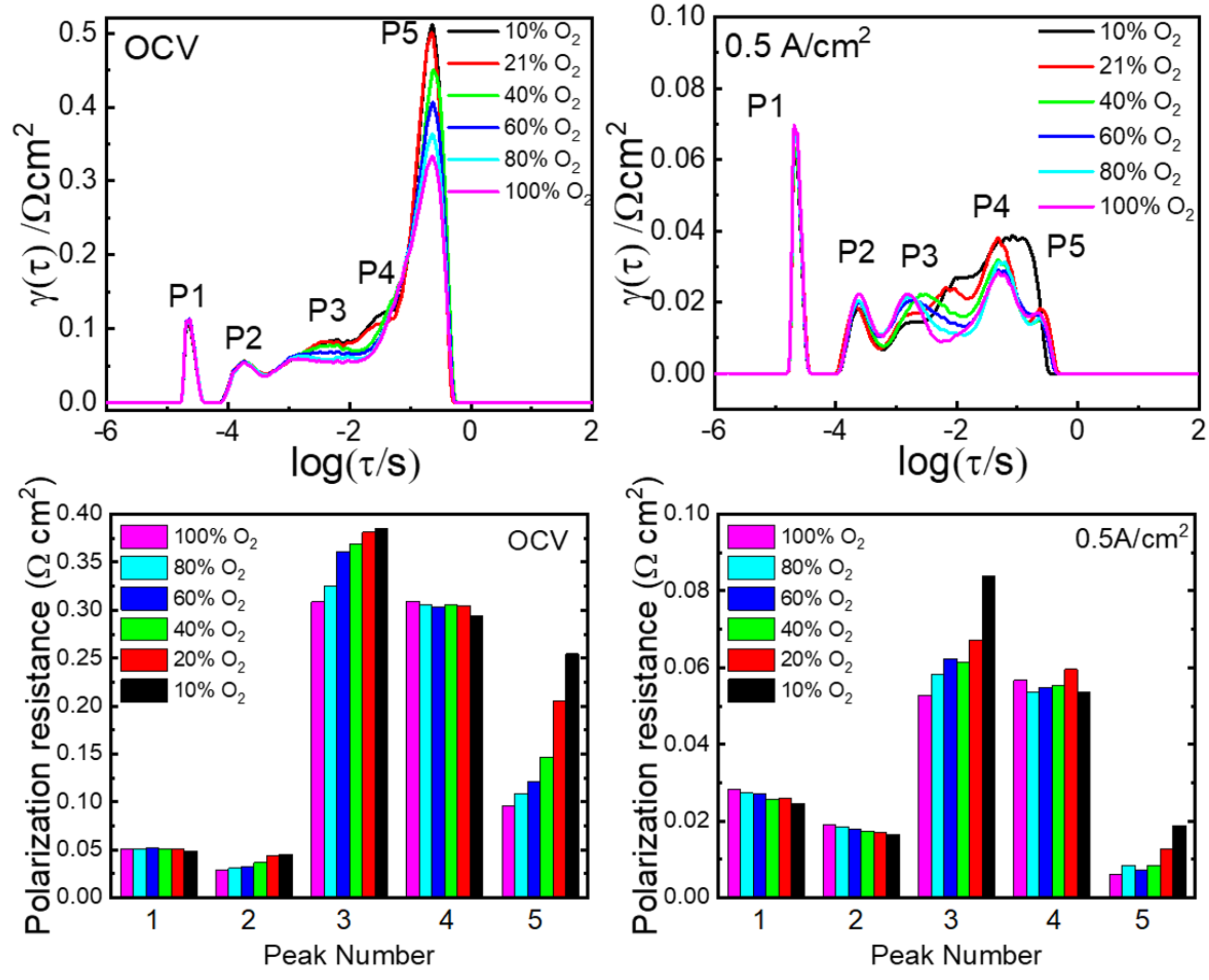

Figure 34. DRT analysis of the peaks vs O_2 concentration. @OCV and @0.5A/cm^2.

The corresponding DRT spectra are reported in **Figures 34a** and **b** with the analysis by integration of distributions P1 – P5 is illustrated in the bar charts in panels (c) and (d) (*v*. also **Table** 4. The polarization resistance ranged between 0.792 – 1.027 Ω cm^2 across the series of measurements at OCV with the lowest estimated values corresponding to the highest $p(O_2)$. Amongst the five distributions, P5 and P3 are the most heavily affected by the concentration of O_2 across all measurements, displaying decreased contributions to the polarization resistance at high $p(O_2)$. Measurements acquired at 0.5 A cm^{-2} return approximately a five-fold decrease in the resistance polarization when compared to analogous data acquired at OCV conditions. Again P5 and P3 display decreased contributions to the resistance as a function of increasing $p(O_2)$.

Effect of the buffer gas on the cell performance was explored and is reported in **Figure 35**. The IV curves in **Figure 35a** show the same trends for both N_2 and He, however a decrease in the resistance as is observed when He is used at a low concentration of O_2. When the concentration of O_2 is increased to 60%, the effect of the balanced gas becomes negligeable, presumably due to the reactant making up the largest fraction of the mixture. The observation is consistent with the EIS spectra, shown in **Figures 35b** and **c** (OCV and 0.5 Acm^{-2}, respectively), wherein the low-frequency arcs return a lower polarization resistance when He is used. Again, buffer gas effect becomes negligeable at high $p(O_2)$. By analysis of the DRT spectra (**Figure 36)**, it is observed that while P1 and P2 are not affected by neither concentration of O_2 and the nature of balanced gas, some dependence on the balanced gas is observed for the other peaks, primarily P5 and P4.

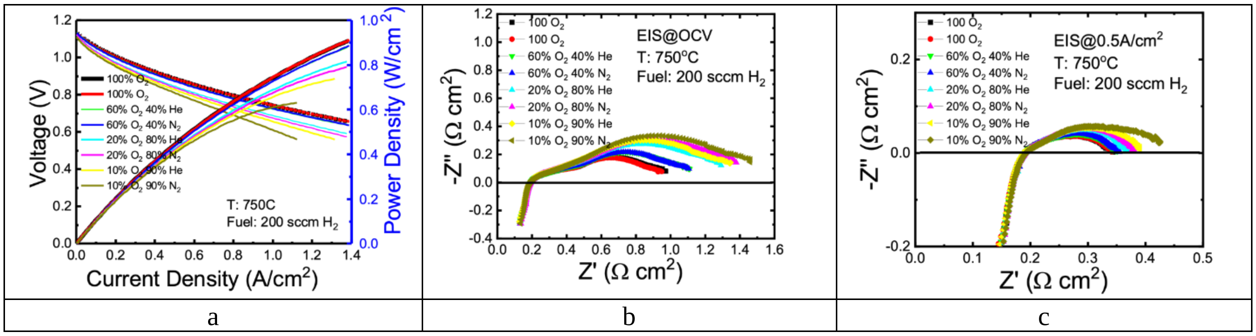

a b c

Figure 35 Changing the balanced gas in the cathode atmosphere on the IV and EIS of the fuel cell.

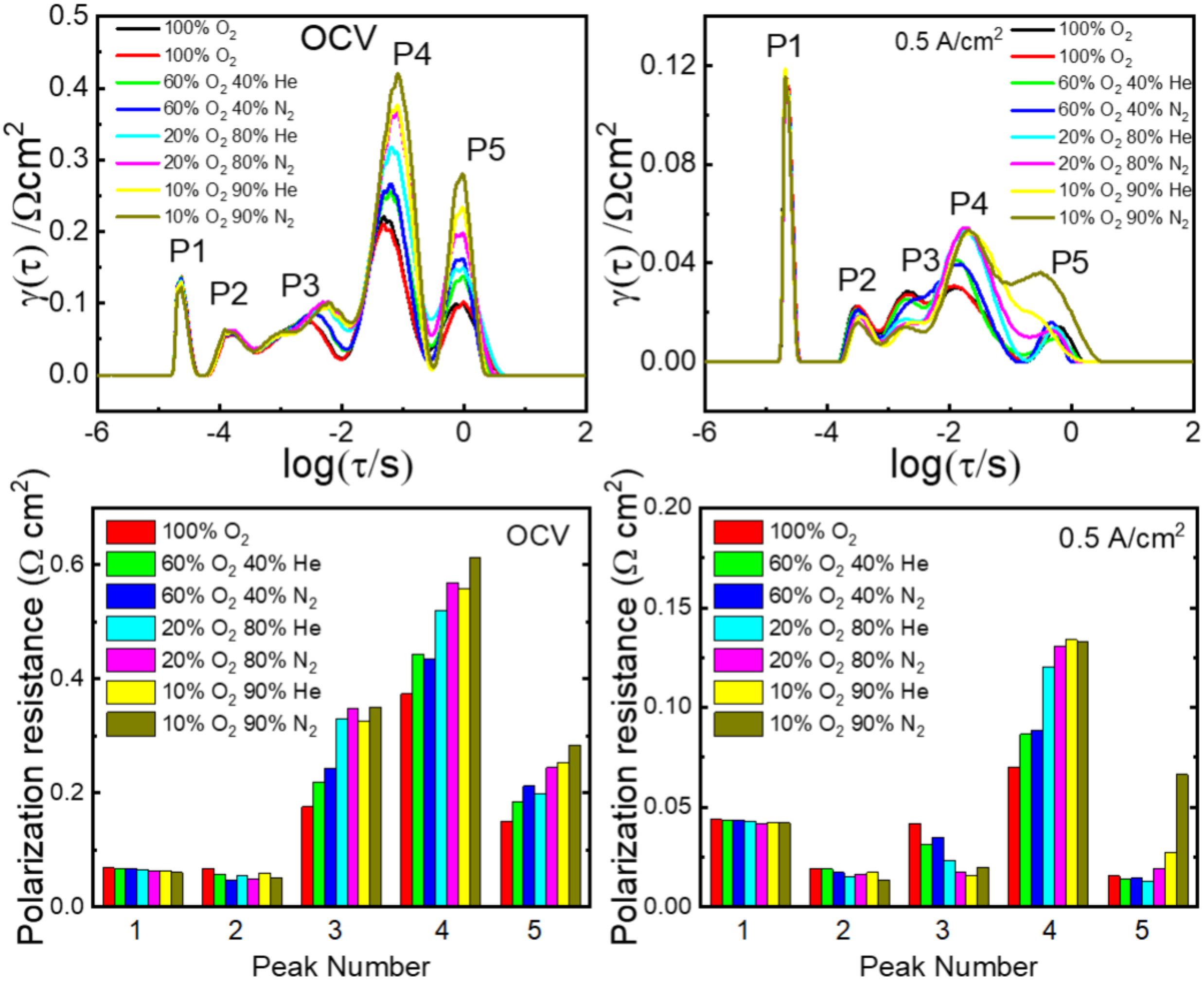

Figure 36. DRT analysis of EIS at OCV or 0.5 A/cm2 with different O_2 concentration and balanced gas.

Table 4: Polarization resistance (Ω cm^2) associated with different peaks (processes) observed in the DRT spectra at OCV and 0.5 A cm^{-2} as a function of varying O_2 concentrations

	OCV					
Peak #	100% O_2	80% O_2	60% O_2	40% O_2	20% O_2	10% O_2
1	0.051	0.051	0.051	0.051	0.050	0.048
2	0.029	0.031	0.032	0.037	0.043	0.046
3	0.308	0.325	0.361	0.369	0.381	0.385
4	0.309	0.305	0.302	0.305	0.305	0.294
5	0.095	0.108	0.121	0.147	0.205	0.254
	0.5 A cm^{-2}					
Peak #	100% O_2	80% O_2	60% O_2	40% O_2	20% O_2	10% O_2
1	0.028	0.027	0.027	0.026	0.026	0.025
2	0.019	0.019	0.018	0.017	0.017	0.017
3	0.053	0.058	0.062	0.061	0.067	0.084
4	0.057	0.053	0.055	0.055	0.060	0.054
5	0.006	0.009	0.007	0.008	0.013	0.019

C.3.1.4 Discussion

Comparison of the results obtained from the anode and cathode assessment allows to obtain an assignment of the DRT spectra and provides insights into the contribution of anode and cathode processes to overall resistance. Firstly, the marked dependence of P5 on the buffer gas used in the fuel mixture (anode) as observed in **Figures 32c** and **d** implies that this distribution can be probably attributed to contribution to the resistance arising from gas diffusion processes. This is in agreement with previous studies performed on similar SOFC assemblies, wherein a low frequency peak (1-10 Hz) is typically attributed to such processes, [26,35–37] in general with reference to the diffusion of fuel gas mixture at the anode. As this peak dominates the DRT spectra in **Figures 32a-b**, it is concluded that anode diffusion resistance may represent the most important contribution to the anode polarization resistance in this SOFC, at least at low concentrations of H_2. The relaxation peak does, however, show dependence on the $p(O_2)$ used at the cathode in **Figures 34 and 35**. By contrast, P1 appears invariant on both concentration of $p(O_2)$ at the cathode and nature of the buffer gas at the both electrodes. A small dependence on the $p(H_2)$ may be observed in **Figure 32**. Comparison with similar studies reported in recent literature may suggest that this peak arises from to charge transfer and ionic conduction processes.[35,36,38] While results from distributions P2 – P4 are somewhat harder to interpret (*v*. **Figure 32a**), the results (**Figures 32 and 34**) suggests that that the contribution to processes associated with these peaks is dependent on either or both $p(H_2)$ and $p(O_2)$, *that is*, increased amount of reactants favor a decrease in the resistance. A less pronounced effect is observed when considering the use of the different balanced gases, especially if compared to P5. In accord with previous literature,[36] these trends suggest that these contributions to polarization resistance arise from electrochemical processes.

An important consideration surrounding the analysis of the DRT spectra and corresponding assignments should be made with reference to the dependence of various contributions on the operating conditions chosen for the experiments, namely $p(H_2)$, $p(O_2)$ and buffer gases. The analysis and assignments are conducted and based on the assumption that each process occurring during operation of the SOFCs is completely decoupled from the others. This assumption represents at best an approximation but enables to assess various contributions of anode and cathode processes to the overall resistance of the SOFC assembly.

However, under certain condition that the relaxation times of two processes strongly couples with each other, the deconvolution is challenging. **Figure 37** shows similar DRT spectra under different operating conditions: (a) EIS was acquired at OCV under two operating conditions (i) 20% O_2 and 97% H_2; (ii) 100% O_2 and 50% H_2/3%H_2O; (b) EIS was acquired at 0.5 A/cm^2 under two operating conditions (i) 10% O_2 and 97% H_2 and (ii) 21% O_2 and 50% H_2. By changing both oxygen concentration and hydrogen concentration, similar spectrum patterns can be obtained. Two or more variables make the deconvolution problems more complex and require more attention on the separation of anode and cathode impedance. Though DRT analysis itself does not depend on the physical process, a better deconvolution process should be based on more reasonable fitting functions relying on a better understanding of the process mechanisms.

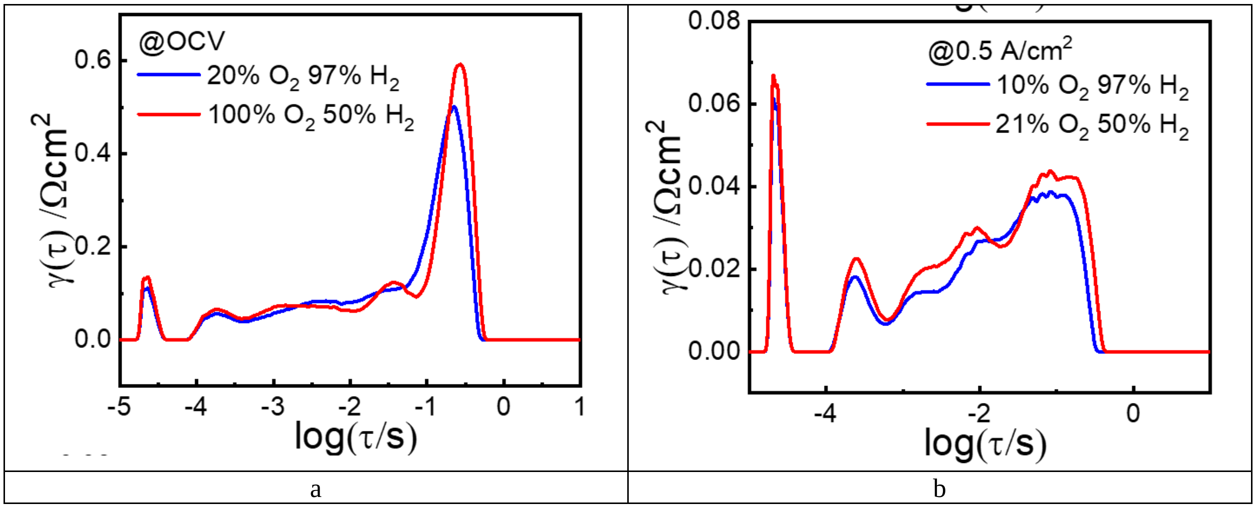

a

b

Figure 37. Similar DRT spectra under different operating conditions: (a) EIS was acquired at OCV under two operating conditions (i) 20% O_2 and 97% H_2; (ii) 100% O_2 and 50% H_2/3%H_2O; (b) EIS was acquired at 0.5 A/cm^2 under two operating conditions (i) 10% O_2 and 97% H_2 and (ii) 21% O_2 and 50% H_2.

In summary, systematic electrochemical studies were performed to evaluate the contributions of cathode and anode to the overall resistance of the solid oxide fuel cell. IV and EIS measurements were first undertaken to evaluate the overall cell resistance. DRT analysis allowed obtaining process-specific information regarding losses occurring during operation of the cell. The analysis allowed deconvoluting and quantifying contributions of processes occurring at the anode and cathode and their dependence on operating conditions, such as concentration of reactants or nature of the carrier gas. Judging from the DRT spectra, five peaks were observed in an SOFC, which are attributed to the charge and mass transfer in electrodes and across the interfaces. While it is natural to assign a specific peak to an electrode, this work shows that both electrodes contribute to a peak at the same time. More importantly, it is possible that two distinctive operations may exhibit a similar DRT spectrum. While DRT analysis is indeed very powerful, extra attention is needed when using it to assign a peak to a specific electrode process.

C.3.2 Effect of Defects on Properties of Nickelates and Nickelate/Ceria Interfaces

Praseodymium nickelate, Pr_2NiO_4 (PNO), is a promising electrode to promote oxygen reduction reaction (ORR) in a solid oxide fuel cell. It however, exhibits phase transformation during an electrochemical operation. The origin for the simultaneous phase transformation and high electrochemical performance still remains obscure. The aim of this section is to carry out a systematic Density Functional Theory (DFT) study to elucidate the mechanism for this conjugated phenomenon. Both electronic structure/charge and normal-mode analysis suggest the presence of peroxide. This study shows that the formation of peroxide (O_2^{2-}) is attributed to both oxygen interstitials and Pr vacancies. The peroxide species limits the oxygen ion migration due to the additional energy required to break its O-O bond, which leads to a decrease in ORR activity. Subsequently, the diffusion paths of Pr-ions was studied while comparing them with those of other Ln^{3+} ions (La, Nd, Pm, Sm, Gd, Tb, Dy, and Ho) in PNO. The formation energies for various Ln^{3+} cation occupancies are calculated, as well as segregation energies in $CeO_2(111)$ surfaces. Finally, criteria for effective Ln^{3+} dopants are developed. La, Nd, and Pm are proposed as potential substituents in PNO to obtain a stable structure

C.3.2.1 Formation of Pr Vacancy and Oxygen Peroxide Species in PNNO

A Monkforst-Pack[26] 4×4× 1, 2×1×1 k-point grid was used for the unit cell of Pr_2NiO_4, while a supercell of 2×3×1 I4/mmm was used for $Pr_{24}Ni_{12}O_{48}$. Both configurations are displayed in **Figure 38**.

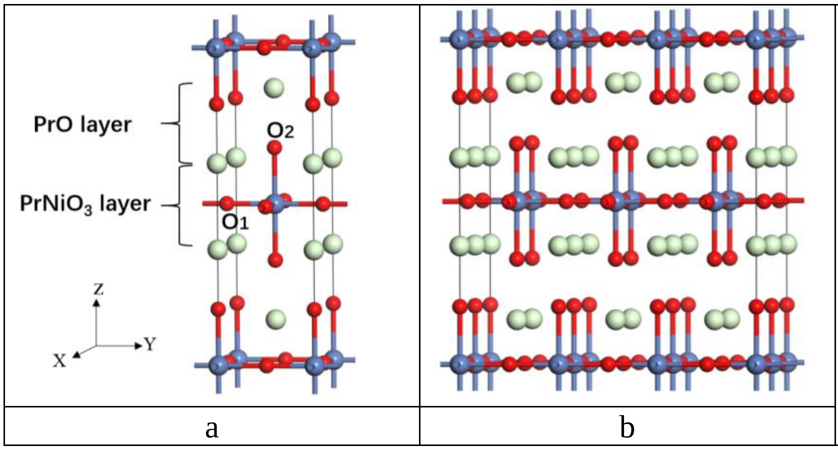

a

b

Figure 38. (a) The optimized I4/mmm Pr_2NiO_4, (b) $Pr_{24}Ni_{12}O_{48}$ 2×3×1 supercell structure. O1 and O2 means two non-equivalent oxygen atoms in Pr_2NiO_4.

Table 5. Structure parameters (Å) of the optimized I4/mmm bulk Pr_2NiO_4

	This work	SM Aspera et al. [33]	Experiment [34]
a	3.85	3.76	3.86
b	3.85	3.76	3.86
c	12.50	12.55	12.58
Ni-O1	1.92	1.88	
Ni-O2	2.21	2.35	
Pr-O2	2.34	2.21	
Pr-Pr (along c)	3.44	3.39	
Pr-Pr (along the ab plane)	3.85	3.76	

PNO has two stable structures[35-37], tetragonal at high temperatures (space group: I4/MMM) and orthorhombic at low temperatures (space group: Bmab). The geometric and electronic structures of I4/MMM PNO were theoretically studied [38-39]. Here, the high-temperature tetragonal I4/MMM structure was used as the model system to investigate the chemical and physical properties of PNO and PNNO while comparing the studies with literature[33]. The calculated lattice parameters and bond lengths of PNO are given in **Table 5**. In this work, the lattice parameters a and b for PNO is in better agreement with experimental values[34], compared to those computed by Aspera et al. [33]. The Ni-O2 distance is 0.29 Å longer than Ni-O1 and the Pr vacancy is created at the center of the 2×3×1 PNO supercell. The optimized structure and the structure distortions around the Pr vacancy are shown in **Figure 38a**. The optimized structure associated with the Pr vacancy shows that the adjacent Pr ion above the Pr vacancy moves 0.18 Å towards the vacancy. The oxygen ions around the Pr vacancy (in the X-Y plane) expand by 0.18 Å. The neighboring oxygen ions below the Pr vacancy are also affected by the vacancy. The first neighbor is shown to move down by 0.23 Å along the Z-axis, whilst the second neighboring oxygen ions contracts by 0.36 Å.

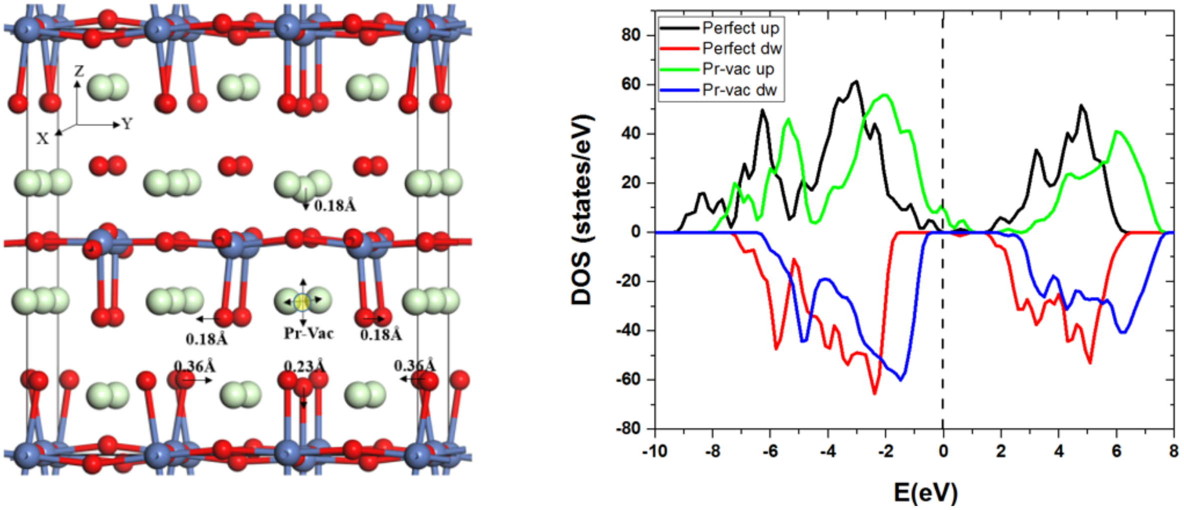

(a) (b)

Figure 39. (a) The optimized $Pr_{23}Ni_{12}O_{48}$ structure. (b) The total density of states for perfect PNO and PNO with Pr vacancies。

The total density of states (TDOS) of $Pr_{23}Ni_{12}O_{48}$ and $Pr_{24}Ni_{12}O_{48}$ with Pr vacancies are given in **Figure 39b**. **Figure 39b** shows that, relative to the Fermi level, the spin up and down TDOS of $Pr_{23}Ni_{12}O_{48}$ move to a higher energy when compared to the TDOS of $Pr_{24}Ni_{12}O_{48}$. This indicates that PNO becomes electron deficient after the removal of a Pr ion, thus shifting the Fermi level to lower energy. The TDOS of $Pr_{23}Ni_{12}O_{48}$ substantially increases at the Fermi level, which indicates that the conductivity improves upon the introduction of a Pr vacancy. This analysis is consistent with the observation of an enhanced conductivity of divalent alkali-earth (e.g., the Ba, Sr, Ca) doped PNO.

A stoichiometric Pr_2NiO_4 is known for its ability to host a large number of oxygen interstitials in the Pr-O layer (**Figure 38**) to form $Pr_2NiO_{4+\delta}$ (PNO+δ)[40-43]. Theoretical studies were performed to calculate the electronic structure of PNO+δ[38-39] and molecular dynamic simulations[44] were carried out to study the oxygen ion diffusion path via an interstitial-mediated mechanism. In this work, the different interstitial O configuration was calculated in PNO with a Pr vacancy. The optimized 6-interstitial O configurations are collected in **Figure 40a**, in which the relative energies of various interstitial O configurations are given with respect to the most stable interstitial O configuration

(configuration 6). For the PrO layer with a Pr vacancy, configurations 4, 5 and 6 in **Figure 40a** show that the interstitial O ions and O ions of octahedral NiO_6 form peroxides (O_2^{2-}) with bond lengths of ca. 1.5 Å and a charge of ca. 1.43-1.50 |e|. This latter observation is also confirmed by the electronic localized functionals in the inset of **Figure 40b**. The normal mode wavenumbers of O_2^{2-} in configuration 6 is calculated to be, 872.1, 358.9, 326.8, 295.8, 249.6, and 113.6 cm^{-1}. DFT calculations by Sadykov et al.[45] also found the formation of O_2^{2-} in a related Pr nickelate $Ca_2NiO_{4+\delta}$. For the PrO layer without Pr vacancy, in the three interstitial O configurations (1, 2, and 3), the interstitial oxygen ion remains in the center of the Pr4 tetrahedron, with a charge of ca. 1.31 |e|. From an energetic viewpoint, it is evident that O_2^{2-} is significantly more stable than the interstitial oxygen ions; the O_2^{2-} is more stable in the vicinity of the Pr vacancy. For the interstitial O, in configurations 1, 2, and 3, the variation in the total energy is 1< 2 < 3, which suggests that the interstitial O favors a longer-range arrangement relative to the Pr Vacancy. Once the $(O_2)^{2-}$ is formed in configurations 4, 5, and 6, the variation in the total energy is 6 < 5 < 4. The Pr vacancy creates a large site for interstitial O with O^{2-} to form $(O_2)^{2-}$. The resulting $(O_2)^{2-}$ relieves steric strain with neighboring atoms thereby lowering the total energy.

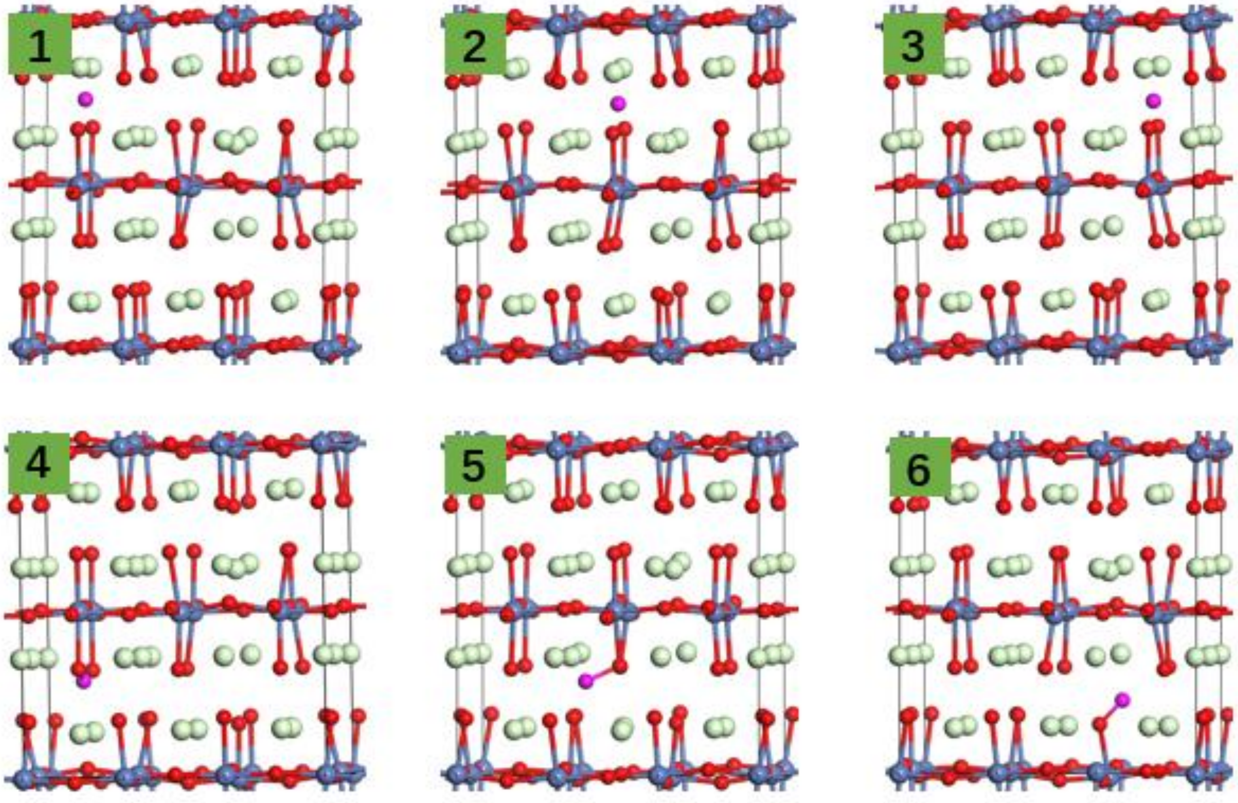

(a)

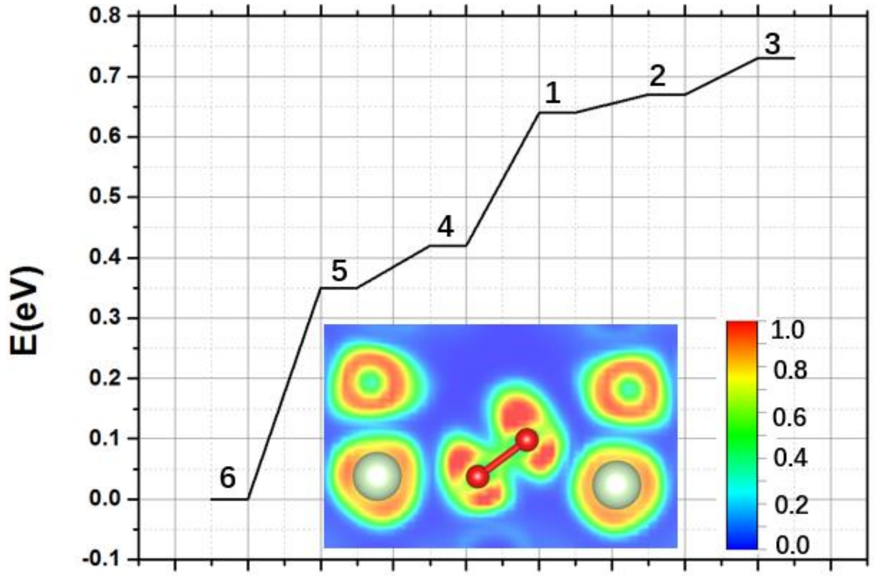

(b)

Figure 40, (a) the optimized interstitial oxygen configurations, (b) the relative energies for different configurations. The inset in b is the electronic localized functional of the peroxide in configuration 6.

The contributions of O_2^{2-} and interstitial oxygen ions to the TDOS of the $Pr_{23}Ni_{12}O_{49}$ were compared. **Figure 41** shows that compared with the interstitial oxygen ion, the O_2^{2-} has an additional peak localized at ca. -22 eV, which is the bonding state of O_2^{2-} and is predominantly composed of the O 2s orbitals. The DOS between -5 to 5 eV represent the partially occupied antibonding states of O_2^{2-} which predominantly comprises of O 2p orbitals. The interstitial oxygen ion does not have these features. The formation energy of an interstitial oxygen ion is expressed by the following equation:

$$E_f = E_{def} - E_{Perfect} - \frac{1}{2} E_{O2}$$

where E_{def} is the total energy of $Pr_{24}Ni_{12}O_{49}$ or $Pr_{23}Ni_{12}O_{49}$, $E_{perfect}$ is the total energy of $Pr_{24}Ni_{12}O_{48}$ or $Pr_{23}Ni_{12}O_{48}$, E_{O2} is the total energy of a single O_2 molecule.

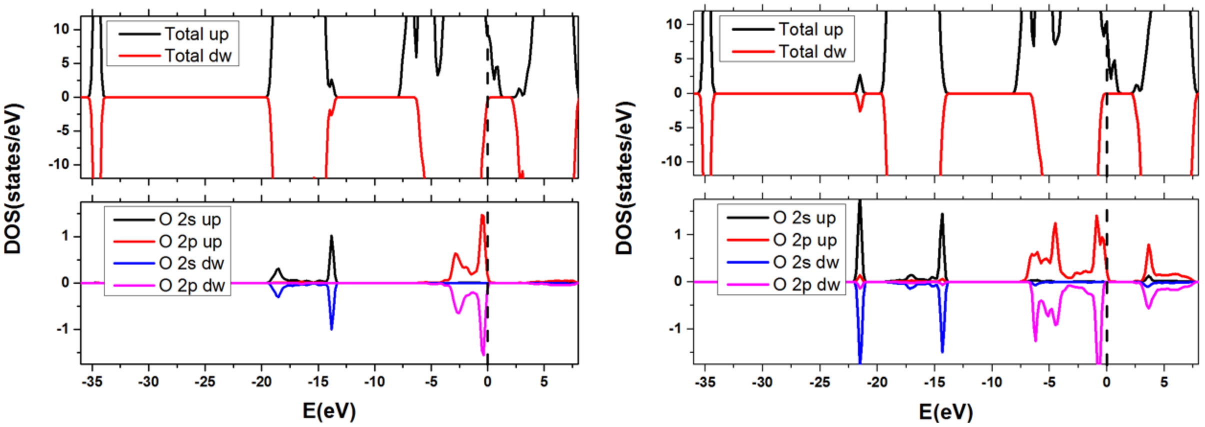

(a) (b)

Figure 41, (a) the total density of states and projected density of states of interstitial oxygen, (b) the total density of states and projected density of states of peroxide.

Table 6. The charge (|e|), $d_{O\text{-}Pr}$: O-Pr, $d_{O\text{-}O}$: O-O distance (Å), formation energies, E_f (eV) of interstitial O in PNO with or without Pr vacancy.

	Configurations	Charge	$d_{O\text{-}Pr}$	$d_{O\text{-}O}$	E_f
$Pr_{23}Ni_{12}O_{49}$	1	1.32	2.28	2.64	0.59
	2	1.31	2.30	2.70	0.62
	3	1.31	2.30	2.70	0.67
	4	0.75	2.39	1.50	0.37
	5	0.73	2.34	1.50	0.30
	6	0.72	2.43	1.48	-0.05
$Pr_{24}Ni_{12}O_{49}$		1.31	2.33	2.64	-1.46

The interstitial O formation energies with or without the Pr vacancy are compared in **Table 6**. It is obvious that the formation energies of O interstitials increases to greater extent with the Pr vacancy, increasing from -1.46 to -0.05-0.37 (for O_2^{2-}), 0.59-0.67 (for oxygen ion) eV. The increased interstitial O formation energy suggests that formation of the O interstitials is hindered. Consequently, the O interstitial content (oxygen nonstoichiometric δ) decreases with the formation of Pr vacancies. The oxygen nonstoichiometric δ also reduces upon the substitution of Sr with La[46] in $(La_xSr_{1-x})_2NiO_{4+\delta}$ and Nd[47] in $(Nd_xSr_{1-x})_2NiO_{4+\delta}$. Compared with pristine $Pr_2NiO_{4+\delta}$, $La_2NiO_{4+\delta}$ and $Nd_2NiO_{4+\delta}$, the smaller oxygen nonstoichiometric δ of $Pr_2NiO_{4+\delta}$ with Pr vacancy resembles the Sr^{2+} substitutions with La^{3+} of $(La_xSr_{1-x})_2NiO_{4+\delta}$ or Nd^{3+} of $(Nd_xSr_{1-x})_2NiO_{4+\delta}$. This attests to the observation that when compared with the pristine PNO, the cation induces electron deficiencies and, consequently, a decrease in the oxygen nonstoichiometric δ.

For PNO with the Pr vacancy, the O_2^{2-} limits the O ion transport. The surface-exchange and bulk-diffusion coefficients decrease as the O interstitial content decreases. Therefore, both these factors lead to the loss of ORR activity.

C.3.2.2 Role of Pr-vacancies and Oxygen Peroxide on the Diffusion of Pr^{3+} and Stability

Pr^{3+} diffusion is an important factor for the understanding of the long-term instability of PNO. For simplicity, studied were performed to on the diffusion paths of both Pr^{3+} and Nd^{3+} in PNO and PNNO. The goal of this part of study is to explain the enhanced long-term stability of PNNO. Two paths for Pr^{3+} or Nd^{3+} diffusion were considered, as shown in **Figure 42**: one along the Y-axis and the other along the Z-axis. The Pr^{3+} or Nd^{3+} diffusion paths were calculated through a Pr vacancy. A lower diffusion barrier was observed for Nd^{3+} diffusion than that for Pr^{3+} by 0.1 and 0.2 eV for the two different paths (1.53 vs 1.63, 3.37 vs 3.57 eV). This lower barrier for Nd^{3+} diffusion originates from the relatively smaller radius of Nd^{3+} compared to Pr^{3+}. From **Table 7**, one can see that the Nd-O and Nd-Pr bond lengths are all shorter than those of Pr-O, Pr-Pr by ca. 0.02 Å. The smaller diffusion barriers indicate that Nd^{3+} diffuses more easily than Pr^{3+}**.** The diffusion of Nd^{3+} into the GDC can effectively block the diffusion of Pr^{3+}, and therefore restricts the decomposition of PNO. **Figure 43** is a schematic to illustrate this process.

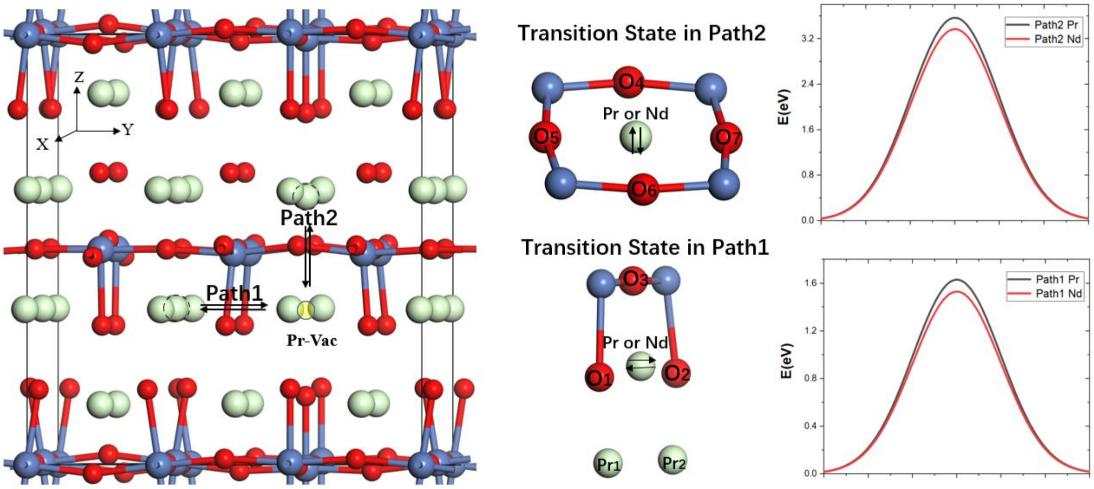

Figure 42, the diffusion path and corresponding transition state configurations.

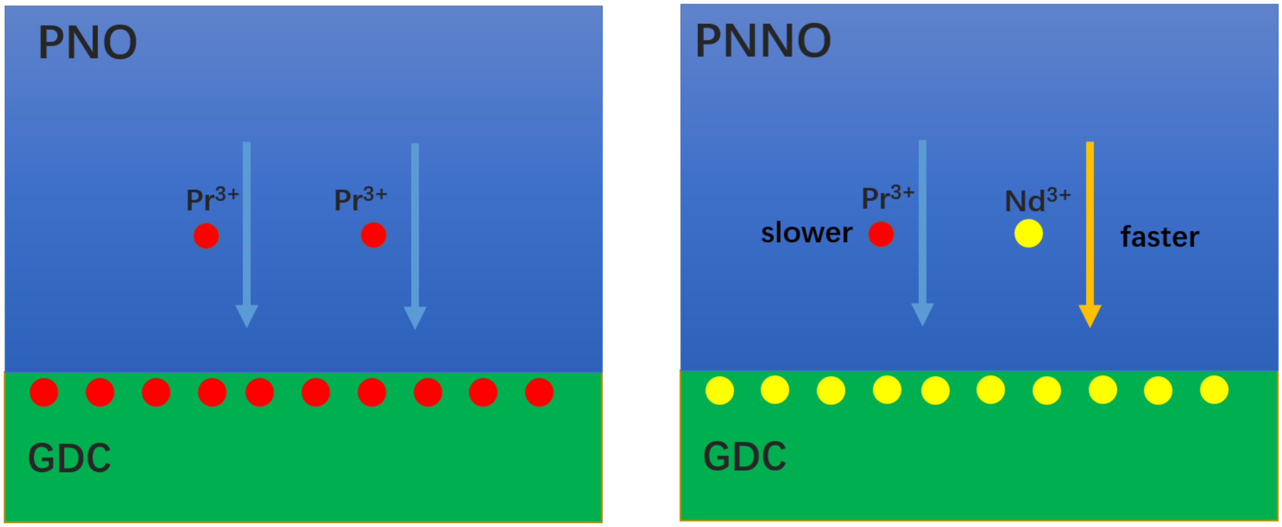

Figure 43. A schematic diagram of the mechanism for the enhanced long-term stability in PNNO.

Table 7. The barriers (eV) for path1 and path2 of Pr or Nd diffusion, the Pr/Nd-O or Pr distances (Å) in transition states.

		Pr diffusion	Nd diffusion
	barriers	1.63	1.53
Path 1	Pr/Nd-O1	2.34	2.32
	Pr/Nd-O2	2.34	2.32
	Pr/Nd-O3	2.32	2.30
	Pr/Nd-Pr1	3.24	3.22
	Pr/Nd-Pr2	3.24	3.22
Path 2	barriers	3.57	3.37
	Pr/Nd-O4	2.23	2.21
	Pr/Nd-O5	2.23	2.21
	Pr/Nd-O6	2.23	2.21
	Pr/Nd-O7	2.23	2.21

C.3.2.3 Selection of Proper Dopant to Improve the Stability of PNO

Other Ln^{3+} dopants (La, Pm, Sm, Gd, Tb, Dy, and Ho) were then considered in PNO. First, the Ln^{3+} diffusion along path 1 was calcualted. **Figure 44a** displays the calculated diffusion energy barriers, showing that the energy barriers increase as the Ln^{3+} Shannon radius increases, which mostly originates from steric hindrances. However, the diffusion barriers are affected by steric hindrances and the electronic interactions of the diffusion Ln^{3+} in the transition state. **Figure 44a** shows that although the radius of La^{3+} is larger than Pr^{3+}, the diffusion energy barrier of La^{3+} is slightly lower than that of Pr^{3+}. This is due to the stronger La-O bond when compared to that of the Pr-O bond at the transition state structure.

In order to evaluate the thermal stability of the dopants in PNO of different concentrations, the formation energies were calculated based the equation below.

$$E_f(Pr_{2-x}Ln_xNiO4) = E^{bulk}_{Pr2NiO4} - (2-x)E^{bulk}_{Pr} - xE^{bulk}_{Ln} - E^{bulk}_{Ni} - 2E_{O2}$$

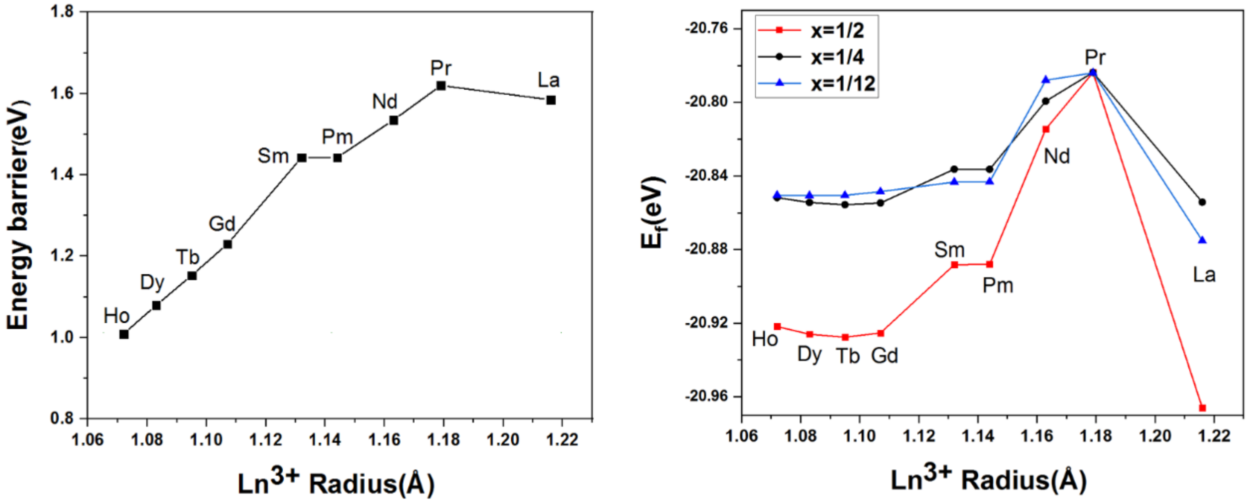

(a) (b)

Figure 44, (a) the energy barriers of Ln in PNO as a function of their Ln^{3+} Shannon radius.(b) the formation energies of Ln in PNO as the function of their Ln^{3+} Shannon radius with different concentrations.

A 2×3×1 PNO surpercell was used with one Ln dopant as x= 1/12; 2×1×1 PNO supercell with one Ln dopant as x = 1/4 and with two Ln dopants as x= 1/2. The calculated formation energies are displayed in **Figure 44b**. From **Figure 44b**, one can see for the concentration x = 1/12, the formation energy of La doped PNO is much lower than that of PNO. This implies that the La-O interaction is much stronger than Pr-O which is helpful in stabilizing Ln^{3+} at the transition state. All Ln dopants in PNO are helpful in reducing the formation energies, especially in large concentrations. This means that Ln^{3+} dopants are useful in increasing the thermal stability of PNO. As **Figure 43** shows, when Ln^{3+} diffuses to GDC, it is able to remain at the interfacial region rather than diffuse out. This leads to quenching of the Pr diffusion, preventing it from diffusing to the deeper bulk site of GDC. At the interface, there exists interdiffusions of Pr and Ce. So, for simplicity, only 12 layer 2×2 $CeO_2(111)$ surface was used to simulate the segregation behavior of Ln^{3+} dopants. The 4×4× 1 Monkforst-Pack[26] *k*-point grid and 12 Å vacuum layer were used to separate neighbor images. The generalized gradient approximation (GGA)+U method, wherein U = 5.5 eV[31] was used to describe the 4f electrons of Ce. The bottom three layers were fixed to mimic the bulk. Different layers of Ce were used with Ln and calculated the differences in the total energy. E1 is defined by the energy difference between the 2nd Ce doping layer and 1st Ce doping layer, while E2 is defined by the energy difference between the 3rd Ce doping layer and 1st Ce doping layer. It is found that E1 and E2 are almost identical while E2 is noticeably larger than E1 in all cases.

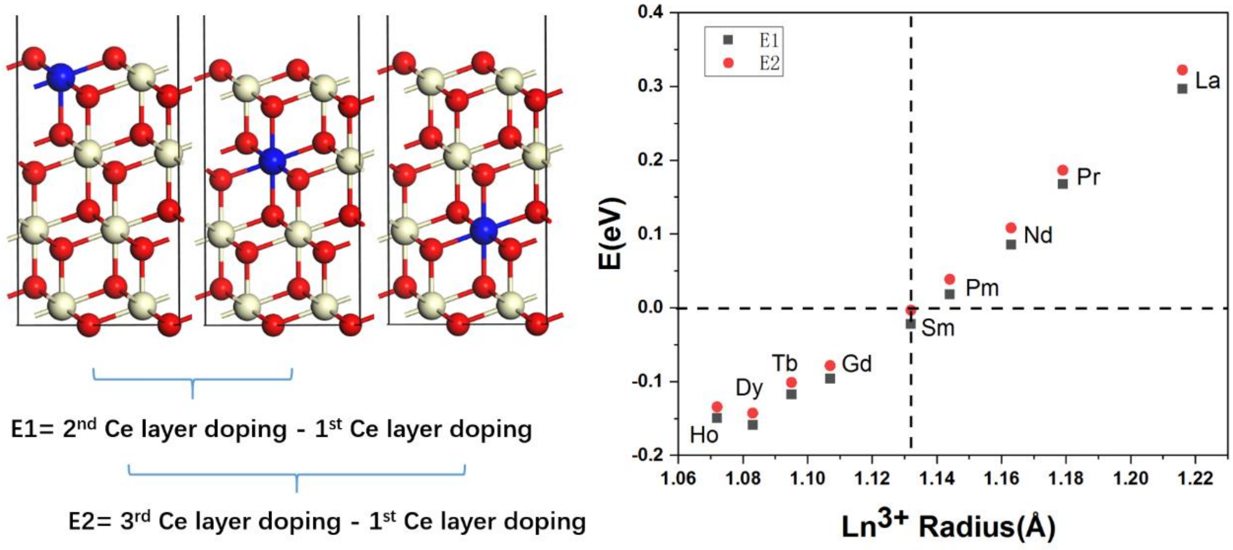

a b

Figure 45, (a) the Ln doping configurations (b) the segregation energies of Ln in CeO_2 as the function of their Ln^{3+} Shannon radius.

Figure 45 demonstrates that Sm is located at the zero boundary line and its radius is the smallest for the series of Ln^{3+} studies, thus favoring the CeO_2 surface layer position. In experiments, the PGCO and PNNO are effective in blocking layers, due to the positive segregation energies of Pr and Nd. This is also in good agreement with the predictions. Here, La and Pm could be potential dopants because of their positive segregation energies, as well as lower diffusion barriers and more negative formation energies.

C.3.3. Effect of Dense GDC Barrier Layer on the Applicability of ATPs in LSCF

The experimental results shown in the Section B do suggest the feasibility of the accelerated measurements to investigate the oxygen electrode of an SOFC. Indeed, the performance degradation for LSCF has been linked with the kinetic demixing of Sr, which subsequently migrates through the porous doped ceria barrier layer, as shown in **Figure 46**. While the exact mechanism for Sr migration remains obscure, it is believed that the vapor phase is highly likely involved, which shows that the highly humidity in air results in faster performance degradation. A dense doped ceria layer was employed, which is assumed to suppress the degradation, even under the accelerated measurements. Shown in **Figure 46** are plots of multiple cells with a dense GDC and under rigorous accelerated test (1 A/cm^2 and high frequency). The ohmic resistance increase was indeed suppressed.

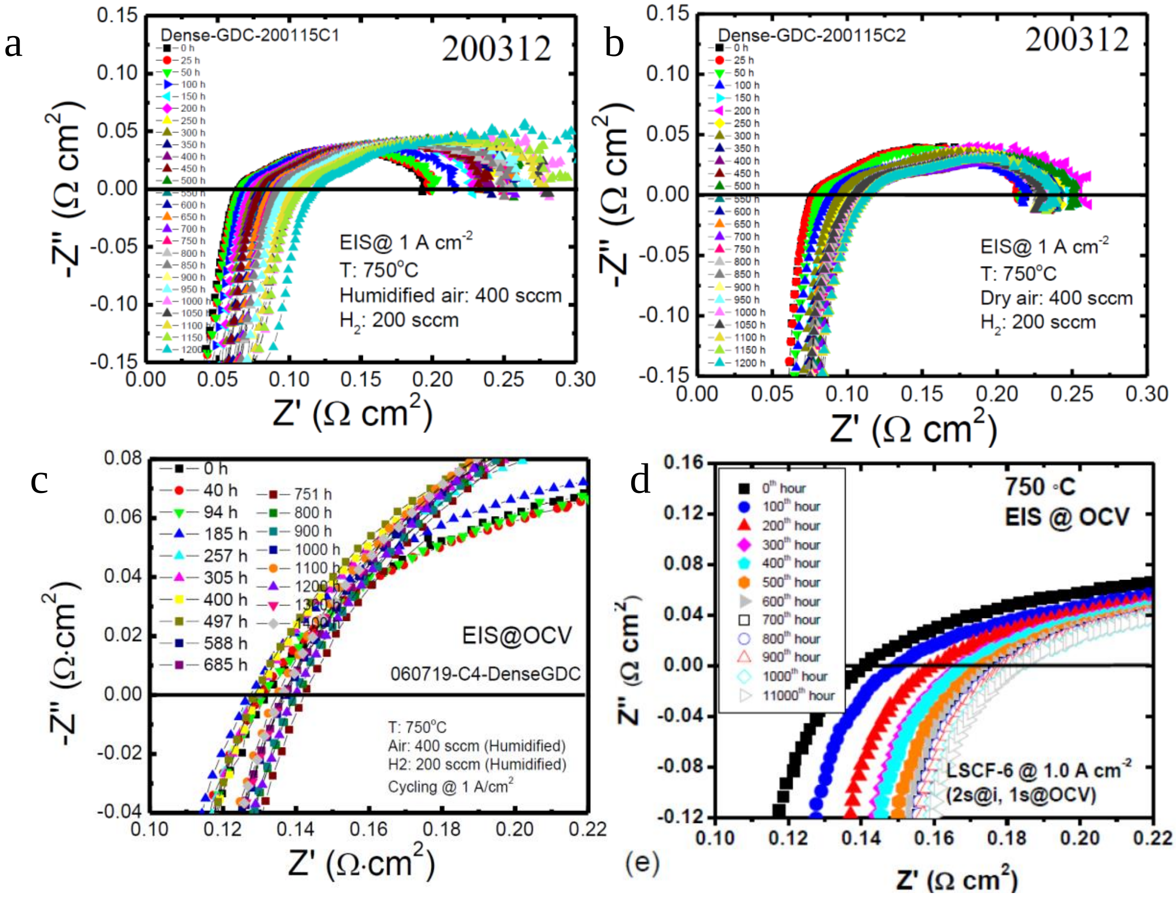

Figure 46. (a) impedance spectra of a cell with dense GDC measured under humidified air and under ATP at 1A/cm^2. (b) impedance spectra of a cell with dense GDC measured under dry air and under ATP at 1A/cm^2, which exhibited slower increase in ohmic ASR, in comparison with **Figure 46a**. (c)) impedance spectra of a cell with dense GDC measured under humidified air and under ATP at 1A/cm^2. Impedance was measured under OCV. (d)) impedance spectra of a cell with porous GDC measured under humidified air and under ATP at 1A/cm^2, which exhibits the greatest increase in ohmic ASR, comparing the other plots (**Figures 46a to c**).

C.4 Summary

Identification of electrode process. DRT analysis allowed obtaining process-specific information regarding losses occurring during operation of the cell. The analysis allowed deconvoluting and quantifying contributions of processes occurring at the anode and cathode and their dependence on operating conditions, such as concentration of reactants or nature of the carrier gas. While it is natural to assign a specific peak to an electrode, this work shows that both electrodes contribute to a peak at the same time. More importantly, it is possible that two distinctive operations may exhibit a similar DRT spectrum. While DRT analysis is indeed very powerful, extra attention is needed when using it to assign a peak to a specific electrode process.

Role of Pr-vacancies and O-interstitials on the activity and stability for nickelate cathodes towards oxygen reduction reaction. Charge, electronic structure, and normal mode analysis shows that the O-interstitials and O in the PrO layer form peroxide (O_2^{2-}) within the Pr vacancy. The formation energies of O-interstitials increase more in the presence of Pr vacancies. The O_2^{2-} limits oxygen-ion transport due to the required additional energy to break its O-O bond. Subsequently, the diffusion paths of Pr-ions were investigated and compared them with other Ln^{3+} ion (La, Nd, Pm, Sm, Gd, Tb, Dy, and Ho) in Pr_2NiO_4. The formation and segregation energies were calculated for different Ln ions (La, Pr, Nd, Pm, Sm, Gd, Tb, Dy, and Ho) in PNO and CeO_2(111) surfaces. Finally, based on the criteria for effective Ln^{3+} dopants: due to their more negative formation energies, lower diffusion energies, and positive separation energies, Pm and La are suggested as potential dopants in PNO to enhance it stability without decomposition.

Effect of dense GDC barrier layer. When a dense GDC barrier layer was used, the increase of ohmic resistance was suppressed. Hence, the migration of Sr through a porous barrier layer and subsequent reaching to the interface between YSZ and doped ceria was indeed the cause for cell performance degradation in LSCF based cathodes. More importantly, the ATP developed in this work can accelerate the demixing process of Sr from LSCF.

D. Milestone status

MILESTONE STATUS REPORT DE-FE0026097

Task/Sub task#	Project Milestone Description	Project Duration – Start: 10/01/2017 End: 09/30/2021												Planned Start Dates	Planned End Dates	Actual Start dates	Actual End dates
		Project year (PY) 1				PY2				PY3							
		Q1	Q2	Q3	Q4	Q1	Q2	Q3	Q4	Q1	Q2	Q3	Q4				
2	Development of Accelerated Test Protocols	■	■	■	■	■	■	■	■	■	■	■	■	10/1/2017	7/30/2021	10/1/2017	4/30/2021
2.1	Baseline tests and examinations	■	■	■	■	■	■	■	■					10/1/2017	9/30/2019	10/1/2017	6/30/2019
2.2/2.3	Test profiles and protocols for electrode			■	■	■	■	■	■	■	■	■		10/1/2017	7/30/2021	10/1/2017	4/30/2021
2.4	Cr-poisoning acceleration studies		■	■	■	■	■	■	■	■	■			1/1/2018	6/30/2019	1/30/2018	9/30/2019
3	Pinpoint the degradaton location		■	■	■	■	■	■	■	■	■	■		3/1/2018	6/30/2021	3/1/2018	6/30/2021

E. Cost Status

The cost status reports the actual cost status of the award when compared with the original Baseline Cost Plan (i.e., the "Forecasted Cash Needs" originally provided on the SF-424A, Section D and as set forth in the Project Management Plan submitted with the Application and Revised with Task 1.0 of SOPO).

COST PLAN/STATUS In $

	Year 1: 10/01/17-09/30/18				Year 2: 10/01/18-09/30/19				Year 3: 10/01/19-09/30/20				Year 4 10/20-			Total
	Q1	Q2	Q3	Q4	Q1	Q2	Q3	Q4	Q1	Q2	Q3	Q4	Q1	Q2	Q3	
Forecasted																
Federal	$40,000	$40,000	$50,000	$40,000	$40,000	$40,000	$40,000	$40,000	$40,000	$40,000	$30,000	$30,000	$30,000	$20,000	$5,077	$525,077
Non-federal	$30,000	$20,000	$10,000	$10,000	$10,000	$10,000	$10,000	$10,000	$8,000	$8,000	$8,000	$8,000	$8,000	$3,000	$3,774	$156,774
Total	$70,000	$60,000	$60,000	$50,000	$50,000	$50,000	$50,000	$50,000	$48,000	$48,000	$38,000	$38,000	$38,000	$23,000	$8,851	$681,851
																$0
Actual																$0
Federal	$20,000	$50,000	$50,000	$35,000	$40,000	$20,000	$40,000	$40,000	$40,000	$10,000	$20,000	$50,000	$50,000	$50,000	$10,077	$525,077
Non-federal	$30,000	$20,000	$10,000	$10,000	$10,000	$10,000	$10,000	$20,000	$8,000	$8,000	$8,000	$5,000	$4,000	$2,000	$1,774	$156,774
Total	$50,000	$70,000	$60,000	$45,000	$50,000	$30,000	$50,000	$60,000	$30,000	$30,000	$30,000	$30,000	$54,000	$52,000	$11,851	$681,851
																$0
Varianc																$0
Federal	-$20,000	$10,000	$0	-$5,000	$0	-$20,000	$0	$0	$0	-$30,000	-$10,000	$20,000	$20,000	$30,000	$5,000	$0
Non-federal	$0	$0	$0	$0	$0	$0	$0	$10,000	$0	$0	$0	-$3,000	-$4,000	-$1,000	-$2,000	$0
Total quarterly	-$20,000	$10,000	$0	-$5,000	$0	-$20,000	$0	$10,000	$0	-$30,000	-$10,000	$17,000	$16,000	$29,000	$3,000	$0
																$0
Cumulative Variance	-$20,000	-$10,000	-$10,000	-$15,000	-$15,000	-$35,000	-$35,000	-$25,000	-$15,000	-$45,000	-$55,000	-$38,000	-$22,000	$7,000	$0	$0

F. Personnel

The contractor will be USC and the PI will be Prof. Xiao-Dong Zhou, who will be assisted by Dr. Stephen Jung, senior research engineers at LGFCS, a postdoc and students will participate in the project.

Dr. Xiao-Dong Zhou is an Associate Professor in the Department of Chemical Engineering at USC. Prior to that, he was a Senior Research Scientist at the Pacific Northwest National Laboratory from 2005-2010. He obtained his Ph.D. in Ceramic Engineering from University of Missouri Rolla. Dr. Zhou received *J. B. Wagner Jr. Young Investigator Award* in 2007 from the Electrochemistry Society (ECS) - High Temperature Materials Division and DOD DARPA's Young Faculty Award in 2011. He currently serves as the Chair for the division. Dr. Zhou's research interest focuses on synthesis, characterization and theoretical understanding of materials for SOFCs. Since 2001, his career has been highlighted by 80 peer-reviewed articles that are related to the proposed research. In addition, he has published 8 invited book chapters, contributed to over 100 presentations; and received 6 US patents/disclosures. He is an associate editor of the Journal of the American Ceramic Society.

Dr. Emir Dogdibegovic (Graduate Student): Emir Dogdibegovic was a graduate student and received his Ph.D. under the supervision by Dr. Zhou. He obtained his B.S. degree in chemistry with minors in physics and math from Hood College, MD. He serves as a president of ECS Student Chapter at USC. He enjoys creating and building instrumentation as a proprietary tool for research. Currently, he is working on structural and electrochemical analysis of Ruddlesden-Popper type MIEC cathode materials to understand the material stability and system performance under operating conditions.

Mr. Yudong Wang (Graduate Student): Yudong Wang is a Ph.D. candidate in Prof. Zhou's group. He obtained his B.S. degree in chemistry from University of Science and Technology of China. He enjoys creating and building instrumentation as a proprietary tool for research. Currently, he is working on structural and electrochemical analysis of Ruddlesden-Popper type MIEC cathode materials to understand the material stability and system performance under operating conditions.

Dr. Wanbing Guan: (Visiting Scholar) His research focuses on SOFC/SOEC, including: Mechanism of Cr poisoning air electrodes; measurement of temperature distribution inside stack; interface contact on cell performance inside stack; microstructure characterization of SOFCs; quantitative contribution of electrode to cell performance inside stack; and new materials for SOFCs

Mr. Josh Wilson is a Ph.D. candidate working in the PI's group. He received B.S. degree from the Chemical Engineering Department at UL Lafayette. Mr. Wilson's research will focus on the innovative SOFC development. He is a Graduate Fellow of the Board of Regents of the State of Louisiana.

Undergraduate: The PI will leverage the Undergraduate Research Fellowships and NSF Research Experience for Undergraduates at UL Lafayette to build a diverse group that includes women and members of underrepresented minority groups. The undergraduates from the PI's group will be encouraged to enroll in the Honors College and to continue further graduate research by applying for graduate fellowships.

H. References

1. Tang, M.; Carter, W. C.; Chiang, Y. M., Electrochemically Driven Phase Transitions in Insertion Electrodes or Lithium-Ion Batteries: Examples in Lithium Metal Phosphate Olivines. In *Annual Review of Materials Research, Vol 40*, Clarke, D. R.; Ruhle, M.; Zok, F., Eds. Annual Reviews: Palo Alto, 2010; Vol. 40, pp 501-529.
2. Chiang, Y. M.; Wang, H. F.; Jang, Y. I., Electrochemically induced cation disorder and phase transformations in lithium intercalation oxides. *Chem. Mat.* **2001,** *13* (1), 53-63.
3. Meethong, N.; Huang, H. Y. S.; Speakman, S. A.; Carter, W. C.; Chiang, Y. M., Strain accommodation during phase transformations in olivine-based cathodes as a materials selection criterion for high-power rechargeable batteries. *Adv. Funct. Mater.* **2007,** *17* (7), 1115-1123.
4. Chick, L. A.; Pederson, L. R.; Maupin, G. D.; Bates, J. L.; Thomas, L. E.; Exarhos, G. J., GLYCINE NITRATE COMBUSTION SYNTHESIS OF OXIDE CERAMIC POWDERS. *Materials Letters* **1990,** *10* (1-2), 6-12.
5. Dogdibegovic, E.; Wright, C. J.; Zhou, X.-D., Stability and Activity of (Pr1-xNdx)2NiO4 as Cathodes for Solid Oxide Fuel Cells: I. Quantification of Phase Evolution in Pr2NiO4. *Journal of the American Ceramic Society* **2016,** *99* (8), 2737-2741.
6. Dogdibegovic, E.; Guan, W.; Yan, J.; Cheng, M.; Zhou, X.-D., Activity and Stability of (Pr1-xNdx)2NiO4 as Cathodes for Solid Oxide Fuel Cells: II. Electrochemical Performance and Performance Durability. *Journal of The Electrochemical Society* **2016,** *163* (13), F1344-F1349.
7. E. Dogdibegovic, Q. C., N. S. Alabri, W. Guan, and X.-D. Zhou, Activity and Stability of (Pr1-xNdx)2NiO4 as Cathodes for Solid Oxide Fuel Cells: III Crystal Structure, Electrical Properties, and Microstructural Analysis. *Submitted to Journal of The Electrochemical Society* **2016**.
8. Yan, J. B.; Chen, H.; Dogdibegovic, E.; Stevenson, J. W.; Cheng, M. J.; Zhou, X. D., High-efficiency intermediate temperature solid oxide electrolyzer cells for the conversion of carbon dioxide to fuels. *Journal of Power Sources* **2014,** *252*, 79-84.
9. Schichlein, H.; Muller, A. C.; Voigts, M.; Krugel, A.; Ivers-Tiffee, E., Deconvolution of electrochemical impedance spectra for the identification of electrode reaction mechanisms in solid oxide fuel cells. *J. Appl. Electrochem.* **2002,** *32* (8), 875-882.
10. Leonide, A.; Sonn, V.; Weber, A.; Ivers-Tiffee, E., Evaluation and modeling of the cell resistance in anode-supported solid oxide fuel cells. *Journal of the Electrochemical Society* **2008,** *155* (1), B36-B41.
11. Liu, B.; Muroyama, H.; Matsui, T.; Tomida, K.; Kabata, T.; Eguchi, K., Analysis of Impedance Spectra for Segmented-in-Series Tubular Solid Oxide Fuel Cells. *Journal of the Electrochemical Society* **2010,** *157* (12), B1858-B1864.
12. Boehm, E.; Bassat, J. M.; Dordor, P.; Mauvy, F.; Grenier, J. C.; Stevens, P., Oxygen diffusion and transport properties in non-stoichiometric Ln(2-x)NiO(4+delta) oxides. *Solid State Ion.* **2005,** *176* (37-38), 2717-2725.
13. Petit, L.; Svane, A.; Szotek, Z.; Temmerman, W. M., First-principles study of rare-earth oxides. *Phys. Rev. B* **2005,** *72* (20).
14. Chen, T.; Pang, S. L.; Shen, X. Q.; Jiang, X. N.; Wang, W. Z., Evaluation of Ba-deficient PrBa1-xFe2O5+delta oxides as cathode materials for intermediate-temperature solid oxide fuel cells. *RSC Adv.* **2016,** *6* (17), 13829-13836.
15. Qin, W.; Nam, C.; Li, H. L.; Szpunar, J. A., Effects of local stress on the stability of tetragonal phase in ZrO2 film. *J. Alloy. Compd.* **2007,** *437* (1-2), 280-284.

16. Dogdibegovic, E.; Yan, J.; Cai, Q.; Jung, H. Y.; Xing, Z.; Liu, Z.; Goettler, R. W.; Zhou, X.-D., Activity and Stability of (Pr1-xNdx)2NiO4+δas Cathodes for Oxide Fuel Cells: Part VI. The Role of Cu Dopant on the Structure and Electrochemical Properties. *Journal of The Electrochemical Society* **2017,** *164* (10), F3131-F3139.
17. Vibhu, V.; Rougier, A.; Nicollet, C.; Flura, A.; Fourcade, S.; Penin, N.; Grenier, J. C.; Bassat, J. M., Pr4Ni3O10+delta: A new promising oxygen electrode material for solid oxide fuel cells. *Journal of Power Sources* **2016,** *317*, 184-193.
18. Dogdibegovic, E.; Cai, Q.; Alabri, N. S.; Guan, W.; Zhou, X.-D., Activity and Stability of (Pr1-xNdx)2NiO4as Cathodes for Solid Oxide Fuel Cells. *Journal of The Electrochemical Society* **2016,** *164* (2), F99-F106.
19. Dogdibegovic, E.; Alabri, N. S.; Wright, C. J.; Hardy, J. S.; Coyle, C. A.; Horlick, S. A.; Guan, W.; Stevenson, J. W.; Zhou, X.-D., Activity and Stability of (Pr1-xNdx)2NiO4as Cathodes for Solid Oxide Fuel Cells: Part V. In Situ Studies of Phase Evolution. *Journal of The Electrochemical Society* **2017,** *164* (12), F1115-F1121.
20. Dogdibegovic, E.; Alabri, N. S.; Tenny, K.; Wright, C. J.; Hardy, J. S.; Coyle, C. A.; Horlick, S.; Guan, W.; Stevenson, J. W.; Zhou, X.-D., The Role of Interlayer on the Catalytic Activity and Performance Stability of (Pr1-xNdx)2NiO4as Cathodes for Solid Oxide Fuel Cells. *ECS Transactions* **2017,** *78* (1), 983-992.
21. Kresse, G.; Furthmüller, J., Efficient iterative schemes for ab initio total-energy calculations using a plane-wave basis set. *Phys. Rev. B* **1996,** *54* (16), 11169.
22. Blöchl, P. E., Projector augmented-wave method. *Phys. Rev. B* **1994,** *50* (24), 17953.
23. Kresse, G.; Joubert, D., From ultrasoft pseudopotentials to the projector augmented-wave method. *Phys. Rev. B* **1999,** *59* (3), 1758.
24. Perdew, J. P.; Burke, K.; Ernzerhof, M., Generalized gradient approximation made simple. *Physical Review Letters* **1996,** *77* (18), 3865-3868.
25. Yu, J.; Rosso, K. M.; Bruemmer, S. M., Charge and ion transport in NiO and aspects of Ni oxidation from first principles. *The Journal of Physical Chemistry C* **2012,** *116* (2), 1948-1954.
26. Monkhorst, H. J.; Pack, J. D., Special points for Brillouin-zone integrations. *Phys. Rev. B* **1976,** *13* (12), 5188-5192.
27. Henkelman, G.; Uberuaga, B. P.; Jónsson, H., A climbing image nudged elastic band method for finding saddle points and minimum energy paths. *The Journal of Chemical Physics* **2000,** *113* (22), 9901-9904.
28. Henkelman, G.; Arnaldsson, A.; Jónsson, H., A fast and robust algorithm for Bader decomposition of charge density. *Computational Materials Science* **2006,** *36* (3), 354-360.
29. Andersson, D. A.; Simak, S. I.; Skorodumova, N. V.; Abrikosov, I. A.; Johansson, B., Optimization of ionic conductivity in doped ceria. *Proceedings of the National Academy of Sciences of the United States of America* **2006,** *103* (10), 3518.
30. Fu, Z.; Sun, Q.; Ma, D.; Zhang, N.; An, Y.; Yang, Z., Effects of Sm doping content on the ionic conduction of CeO2 in SOFCs from first principles. *Applied Physics Letters* **2017,** *111* (2), 023903.
31. Sun, Q.; Fu, Z.; Yang, Z., Effects of rare-earth doping on the ionic conduction of CeO2 in solid oxide fuel cells. *Ceramics International* **2018,** *44* (4), 3707-3711.
32. Sakakibara, H.; Usui, H.; Suzuki, K.; Kotani, T.; Aoki, H.; Kuroki, K., Model Construction and a Possibility of Cupratelike Pairing in a New ${d}^{9}$ Nickelate Superconductor $(\mathrm{Nd},\mathrm{Sr}){\mathrm{NiO}}_{2}$. *Physical Review Letters* **2020,** *125* (7), 077003.

33. Aspera, S. M.; Sakaue, M.; Wungu, T. D. K.; Alaydrus, M.; Linh, T. P. T.; Kasai, H.; Nakanishi, M.; Ishihara, T., Analysis of structural and electronic properties of Pr2NiO4through first-principles calculations. *Journal of Physics: Condensed Matter* **2012,** *24* (40), 405504.
34. Allançon, C.; Gonthier-Vassal, A.; Bascat, J. M.; Loup, J. P.; Odier, P., Influence of oxygen on structural transitions in Pr2NiO4+δ. *Solid State Ion.* **1994,** *74* (3), 239-248.
35. Obradors, X.; Martinez, B.; Batlle, X.; Rodriguez‐Carvajal, J.; Fernandez‐Diaz, M.; Martínez, J.; Odier, P., Magnetic transitions in Pr2NiO4 single crystal. *Journal of applied physics* **1991,** *70* (10), 6329-6331.
36. de Andrés, A.; Martinez, J.; Odier, P., Dynamical study of the structural and magnetic phases in Pr 2 NiO 4 single crystals by Raman spectroscopy. *Phys. Rev. B* **1992,** *45* (22), 12821.
37. Kovalevsky, A.; Kharton, V.; Yaremchenko, A.; Pivak, Y.; Tsipis, E.; Yakovlev, S.; Markov, A.; Naumovich, E.; Frade, J., Oxygen permeability, stability and electrochemical behavior of $$\Pr _ {2}{\text {NiO}} _ {{4+\delta}} $$-based materials. *Journal of electroceramics* **2007,** *18* (3-4), 205-218.
38. Aspera, S.; Sakaue, M.; Wungu, T.; Alaydrus, M.; Linh, T.; Kasai, H.; Nakanishi, M.; Ishihara, T., Analysis of structural and electronic properties of Pr2NiO4 through first-principles calculations. *Journal of Physics: Condensed Matter* **2012,** *24* (40), 405504.
39. Aspera, S. M.; Sakaue, M.; Alaydrus, M.; Wungu, T. D. K.; Linh, T.; Kasai, H.; Ishihara, T., Investigations on the Structural and Electronic Properties of Pure and Doped Bulk Pr2NiO4 through First Principles Calculations. *ECS Transactions* **2013,** *57* (1), 2753.
40. Allançon, C.; Gonthier-Vassal, A.; Bascat, J.; Loup, J.; Odier, P., Influence of oxygen on structural transitions in Pr2NiO4+ δ. *Solid State Ion.* **1994,** *74* (3-4), 239-248.
41. Niwa, E.; Wakai, K.; Hori, T.; Yashiro, K.; Mizusaki, J.; Hashimoto, T., Thermodynamic analyses of structural phase transition of Pr2NiO4+ δ involving variation of oxygen content. *Thermochimica Acta* **2014,** *575*, 129-134.
42. Sakai, M.; Wang, C.; Okiba, T.; Soga, H.; Niwa, E.; Hashimoto, T., Thermal analysis of structural phase transition behavior of Ln 2 Ni 1− x Cu x O 4+ δ (Ln= Nd, Pr) under various oxygen partial pressures. *Journal of Thermal Analysis and Calorimetry* **2019,** *135* (5), 2765-2774.
43. Zhou, X.-D.; Templeton, J. W.; Nie, Z.; Chen, H.; Stevenson, J. W.; Pederson, L. R., Electrochemical performance and stability of the cathode for solid oxide fuel cells: V. high performance and stable Pr2NiO4 as the cathode for solid oxide fuel cells. *Electrochimica Acta* **2012,** *71*, 44-49.
44. Parfitt, D.; Chroneos, A.; Kilner, J. A.; Grimes, R. W., Molecular dynamics study of oxygen diffusion in Pr 2 NiO 4+ δ. *Physical Chemistry Chemical Physics* **2010,** *12* (25), 6834-6836.
45. Sadykov, V.; Pikalova, E.; Eremeev, N.; Shubin, A.; Zilberberg, I.; Prosvirin, I.; Sadovskaya, E.; Bukhtiyarov, A., Oxygen transport in Pr nickelates: Elucidation of atomic-scale features. *Solid State Ion.* **2020,** *344*, 115155.
46. Nakamura, T.; Yashiro, K.; Sato, K.; Mizusaki, J., Oxygen nonstoichiometry and defect equilibrium in La2−xSrxNiO4+δ. *Solid State Ion.* **2009,** *180* (4), 368-376.
47. Nakamura, T.; Yashiro, K.; Sato, K.; Mizusaki, J., Defect chemical and statistical thermodynamic studies on oxygen nonstoichiometric Nd2−xSrxNiO4+δ. *Solid State Ion.* **2009,** *180* (26), 1406-1413.